

Evaluation of FDS V.4: Upward Flame Spread

by
Jae-Wook Kwon

A Thesis
Submitted to the Faculty
of the

WORCESTER POLYTECHNIC INSTITUTE

in partial fulfillment of the requirements for the

Degree of Master of Science

in

Fire Protection Engineering

August 2006

APPROVED:

Professor Nicholas A. Dembsey, Major Advisor

Christopher W. Lautenberger, University of California Berkeley, Co-Advisor

Professor Kathy A. Notarianni, Head of Department

ABSTRACT

NIST's Fire Dynamics Simulator (FDS) is a powerful tool for simulating the gas phase fire environment of scenarios involving realistic geometries. If the fire engineer is interested in simulating fire spread processes, FDS provides possible tools involving simulation of the decomposition of the condensed phase: gas burners and simplified pyrolysis models. Continuing to develop understanding of the capability and proper use of FDS related to fire spread will provide the practicing fire engineer with valuable information. In this work three simulations are conducted to evaluate FDS V.4's capabilities for predicting upward flame spread. The FDS predictions are compared with empirical correlations and experimental data for upward flame spread on a 5 m PMMA panel. A simplified flame spread model is also applied to assess the FDS simulation results. Capabilities and limitations of FDS V.4 for upward flame spread predictions are addressed, and recommendations for improvements of FDS and practical use of FDS for fire spread are presented.

ACKNOWLEDGEMENTS

I would like to thank my thesis advisor, Professor Nicholas A. Dembsey for his guidance and advice. He enthusiastically offered his advice even if he was on a busy schedule. I appreciate his thoughtful considerations in every aspect to encourage me to become a better engineer throughout my graduate experience at WPI. I would also like to thank Christopher W. Lautenberger for his advice. He generously answered my questions and offered different perspectives in approaching and solving a problem. I have been fortunate to have them as my advisors.

I'm grateful to Arup and FM Global which both provided generous partial financial support toward this research. I also thank the department of fire protection engineering at WPI for giving me the opportunity to study fire protection engineering through their academic and financial support.

I give my thanks to Seung-han Lee for his help and encouragement. I also thank Randy Harris for helping me complete a series of residential-scale experiments. It was a pleasure to work with them.

Finally, my huge thanks go to my parents and my girlfriend who always encouraged me and stood by me. I do not name here, but I thank my friends who helped me go through this path. I thank God for allowing me all these wonderful people and environments.

TABLE OF CONTENTS

ABSTRACT II	
ACKNOWLEDGEMENTS	III
TABLE OF CONTENTS	IV
LIST OF FIGURES	VIII
NOMENCLATURE	X
OVERVIEW OF THESIS	1
INTRODUCTION	1
Background	1
Scope of Work	5
OVERVIEW OF FDS V.4	6
Hydrodynamic model	6
Turbulence Model	6
Combustion Model	6
Automatic_Z : Adjustment of Stoichiometric value of Mixture Fraction	7
Thermal Radiation Model	7
Radiation Inside Flame Zone	8
Thermally-Thick Thermoplastic Fuel	9
EXPERIMENTAL WORK	10
Experimental Configuration	10
Experimental Data	11
FDS INPUT DATA	13
PMMA Panel Simulation	13
Geometry	13
Grid Resolution	14

Ignition Source.....	15
Material Properties.....	16
RESULTS AND DISCUSSION.....	19
PMMA Panel Simulation.....	19
Heat Release Rate and Pyrolysis Height.....	19
Flame Heights and Heat Fluxes.....	20
Forward Heating Zone Length.....	24
Mass Loss Rate.....	26
MMA Burner Simulation.....	26
“AUTOMATIC_Z” disabled PMMA Panel Simulation.....	30
Heat Release Rate and Pyrolysis Height.....	30
Flame Heights and Heat Fluxes.....	32
SIMPLIFIED FLAME SPREAD MODEL.....	32
CONCLUSION.....	35
REFERENCES.....	37
FUTURE WORK.....	41
APPENDIX A THEORETICAL DESCRIPTIONS FOR FDS.....	42
A1 Hydrodynamic Model.....	42
A2 Combustion Model.....	43
A2.1 Mixture Fraction Combustion Model.....	43
A2.2 State Relations.....	46
A2.3 Heat Release Rate Calculation in FDS.....	47
A3 Thermal Radiation Model.....	48
A3.1 Radiative Transport Equation (RTE).....	48
A3.2 Thermal Radiation Model in FDS.....	48
A3.3 Radiation Inside Flame Zone.....	49
A4 Appendix A References.....	50

APPENDIX B GRID RESOLUTION ANALYSIS.....	51
B1 Grid Resolution Criteria and Test Matrix	51
B2 Description of Steckler’s Experiment	53
B3 Comparison FDS Predictions with Experimental Data	53
B4 Summary.....	56
B5 Appendix B References	56
APPENDIX C GASEOUS PHASE SENSITIVITY ANALYSIS.....	58
C1 Parameters in the MISC Namelist Group (CSMAG, PR, and SC)	60
C1.1 Smagorinsky Coefficient (CSMAG) Sensitivity Analysis.....	60
C1.2 Turbulent Prandtl Number (PR) Sensitivity Analysis	67
C1.3 Turbulent Schmidt Number (SC) Sensitivity Analysis.....	72
C2 Parameters in the RADI Namelist Group (Angle Increment, Number Radiation Angles, and Time Increment)	74
C2.1 Angle Increment Sensitivity Analysis.....	74
C2.2 Number Radiation Angles Sensitivity Analysis	77
C2.3 Time Step Increment Sensitivity Analysis.....	80
C3 Parameters in the REAC (Radiative Fraction)	83
C3.1 Radiative Fraction Sensitivity Analysis	83
C4 Appendix C References	86
APPENDIX D PROPANE CHARACTERIZATION EXPERIMENT.....	88
D1 Experimental Configurations and Conditions	88
D1.1 Test Compartments.....	88
D1.2 Room Contents and Gas burner	90
D2 Instrumentation	92
D2.1 Thermocouple Rakes	92
D2.2 Thin-Skin Calorimeters.....	94
D3 Data Reduction	97
D3.1 Heat Release Rate (HRR).....	97
D3.2 Gas Temperature and Radiation Corrected Temperature	101
D3.3 Incident Heat Flux	103

D3.4. Smoke Properties.....	105
D4 Results and Discussion	105
D5 Summary	109
D6 Appendix D References	110
APPENDIX E PMMA PANEL SIMULATION WITH HIGH ACTIVATION ENERGY AND HIGH PRE-EXPONENTIAL FACTOR.....	112
E1 New Material Properties for PMMA.....	112
E2 Results and Discussions	112
E3 Appendix E References	114
APPENDIX F FDS INPUT FILE FOR PMMA PANEL SIMULATION.....	115

LIST OF FIGURES

Figure 1 FDS V.2 Flame Spread Predictions of 5 m PMMA Wall Panel Experiment compared to FMRC Experimental Data [12].	5
Figure 2 Configuration of 5 m PMMA Wall Panel Experiment under Fire Products Collector [12].	11
Figure 3 Heat Release Rate History from FMRC Experiment [12].	12
Figure 4 Pyrolysis Height History from FMRC Experiment [12].	12
Figure 5. Heat Flux Distribution over PMMA Panel from FMRC Experiment [12].	13
Figure 6 Global View of FDS Domain.	14
Figure 7 Detail View of FDS Domain. Green block is “hot block” for Ignition.	16
Figure 8 Mass Flux History Comparison between Lee’s Model and Experiment for 0.025 m Black PMMA (Applied Heat Flux of 50 kW/m ²) [32].	17
Figure 9 Time to Ignition vs. Applied Heat Flux for Black PMMA, Thickness 0.025 m.....	18
Figure 10 Mass Loss Rate vs. Applied Heat Flux for Black PMMA, Thickness 0.025 m.....	18
Figure 11 Heat Release Rate Comparison between the FMRC Experiment [12] and Simulation.....	20
Figure 12 Pyrolysis Height Comparison between FMRC Experiment [12] and Simulation.....	20
Figure 13 Heat Flux Comparison between FMRC Experiment [12] and FDS Simulation at Pyrolysis Heights of 0.9m.....	22
Figure 14 Heat Flux Comparison between FMRC Experiment [12] and FDS Simulation at Pyrolysis Heights of 1.73m.....	22
Figure 15 Heat Flux Comparison between FMRC Experiment [12] and FDS Simulation at Pyrolysis Heights of 3.55m.....	23
Figure 16 Heat Flux Comparison between FMRC Experiment [12] and FDS Simulation at Pyrolysis Heights of 4.69m.....	23

Figure 17 Schematic Diagram of Upward Flame Spread.....	25
Figure 18 Forwarding Heating Zone vs. Pyrolysis Height for FMRC Experiment [12], FDS Simulation, and Orloff Correlation [9].....	25
Figure 19 FDS Simulated Mass Loss Rate vs. Height at Pyrolysis Height of 0.9 m.....	26
Figure 20 View of MMA Burner Simulation Domain.....	27
Figure 21 HRRPUV PLOT3D Snapshots ($H_p=1m$, $HRR=146kW$) from: (a) MMA Burner Simulation (b) PMMA Panel Simulation.	28
Figure 22 Flame Height vs. Pyrolysis Height for FDS Simulations and empirical correlations [9, 40].	29
Figure 23 Heat Flux Distribution Comparison with FMRC Experiment [12], PMMA Panel Simulation, and MMA Burner Simulation.	30
Figure 24 Heat Release Rate History Comparison between FMRC Experiment [12] and FDS Simulations.	31
Figure 25 Pyrolysis Height History Comparison between FMRC Experiment [12] and FDS Simulations.	31
Figure 26 Heat Flux Comparison between FMRC Experiment [12] and FDS Simulations with Flame Heights at Pyrolysis Height of 0.9m.	32
Figure 27 Comparisons of Time to Ignition Data (FMRC Experiment [12] and AUTOMATIC_Z enabled and disabled PMMA Panel Simulations).	34
Figure 28 Forward Heating Zone Heat Fluxes from Time to Ignition Data and Direct Measurements (FMRC Experiment [12], and "AUTOMATIC_Z" enabled and disabled PMMA Panel Simulations)	35

NOMENCLUTURE

a	Mean absorption coefficient [m^{-1}]
A	Pre-exponential factor [m/s],
c	Constant pressure specific heat of solid [$\text{kJ/kg}\cdot\text{K}$]
C	Constant for defining an effective stoichiometric value of mixture fraction[-]
D^*	Plume characteristic length [m]
E_A	Activation energy [J/mol]
H_f	Flame height [cm]
H_p	Pyrolysis height [cm]
i	Radiation intensity [W/m^2]
k	Fuel thermal conductivity [$\text{W/m}\cdot\text{K}$]
L	Thickness of solid
\dot{m}''	Mass loss rate per unit area [$\text{kg/m}^2\cdot\text{s}$]
$\dot{m}''_{critical}$	Critical mass loss rate [$\text{kg/m}^2\cdot\text{s}$]
P_0	Background pressure [Pa]
\dot{Q}	Total heat release rate [kW]
\dot{q}'''	Heat release rate per unit volume [kW/m^3]
\dot{q}''_c	Convective heat flux [kW/m^2]
\dot{q}''_r	Radiative heat flux [kW/m^2]
\dot{q}''_{net}	Net heat flux [kW/m^2]
R	Universal gas constant [$\text{J/mol}\cdot\text{K}$]
S	Coordinate along path of radiation [-]
T	Temperature [K]
T_o	Initial temperature [K]
T_s	Surface temperature [K]
T_{ig}	Ignition temperature [K]

V_p	Pyrolysis spread rate [cm/s]
x	Distance from heated surface [m]
Z_{st}	Ideal stoichiometric value of mixture fraction [-]
$Z_{st,eff}$	Effective stoichiometric value of mixture fraction [-]

Greek Symbols

β	Constant for pyrolysis spread rate [-]
ΔH_v	Heat of vaporization [kJ/kg]
$d\delta$	Grid spacing [m]
μ	Dynamic viscosity [kg/m·s]
ρ	Density of solid [kg/ m ³]
σ	Stefan-Boltzmann constant [5.67 x 10 ⁻¹¹ kW/m ² K ⁴]
χ_{rad}	Radiative fraction [-]

Abbreviation

CFD	Computational Fluid Dynamics
DNS	Direct Numerical Simulation
FDS	Fire Dynamics Simulator
HRR	Heat release rate
HRRPUV	Heat release rate per unit volume
LES	Large Eddy Simulation
MLR	Mass loss rate
MMA	Methyl methacrylate
NIST	National Institute of Standards and Technology
PMMA	Polymethyl methacrylate
TC	Thermocouple

Overview of Thesis

FDS V.4 capabilities to predict upward flame spread on surfaces are investigated and are presented in the body of this thesis. Appendix A presents the theoretical description of FDS with regards to its hydrodynamic model, combustion model, and thermal radiation model. Appendix B and Appendix C present grid resolution sensitivity analyses and gaseous phase sensitivity analyses, respectively. Both are conducted as preliminary work to provide a firm basis for the flame spread investigation. Appendix D describes the propane characterization experiment which was used for gaseous phase sensitivity analyses. Appendix E describes one of the FDS simulations (high activation energy and high pre-exponential factor) which was used to investigate potential connections to previous flame spread work involving FDS V.4. Appendix F provides the FDS input data file for one of the upward flame spread simulations: PMMA panel.

Introduction

Background

Flame spread is an important mechanism in development of large fires which present significant hazards to life safety and property. Studies starting with de Ris [1] and followed by Altenkirch et al. [2], Zhou et al. [3], Wichman et al. [4,5], and Bhattacharjee et al. [6,7] have focused on opposed flow flame spread (air flow opposed to the spread direction). Other studies have focused on vertical flame spread (wind-aided or concurrent flow spread). Concurrent flow flame spread rates are faster than opposed flow flame spread rates and are inherently unsteady, accelerating as pyrolysis heights increase. Markstein and de Ris [8] investigated upward fire spread over textiles. They found an accelerating flame-spread rate and characterized it by a power-law relationship between pyrolysis spread rate V_p and pyrolysis height H_p :

$$V_p = \beta H_p^n \quad (1)$$

Orloff et al. [9] examined the upward fire spread rate for vertical polymethyl methacrylate (PMMA). With 4.5 cm thick, 41 cm wide, and 157 cm high vertical PMMA slabs, they observed flame spread remained relatively constant for pyrolysis heights from 10 to 15 cm and subsequently became proportional to H_p :

$$V_p = 0.00441H_p^{0.964} \quad (2)$$

This empirical correlation suggests that spread rate and pyrolysis height increase exponentially with time. The total flame heat flux back to the burning surface increases approximately linearly from 21 kW/m² at 0.38 m high to 27 kW/m² at 1.5 m high. Fire behavior of PMMA was studied comprehensively by Tewarson and Ogden [10]. They also found flame spread rates accelerate for upward spread. The total heat fluxes to the solid flame region ranged from 20 to 30 kW/m² for 0.61 m PMMA samples, which agreed with the analysis by Quintiere et al. [11]. Wu et al. [12] conducted a 5 m high PMMA vertical wall panel experiment. The heat release rate and pyrolysis heights increased exponentially as a function of time. Total heat fluxes to the fuel surface varied from 30 to 40 kW/m².

As the performance of computers has been improving rapidly, considerable attention has been given to fire field models, or Computational Fluid Dynamics (CFD) models. Since the National Institute of Standards and Technology (NIST) released Fire Dynamics Simulator (FDS) [13] in 2000, it has been a powerful tool for simulating the consequences of fire scenarios involving realistic geometries. The usual application of FDS involves specifying the HRR history directly using a “gas burner”. If the fire engineer is interested in estimating the actual fire spread processes rather than specifying the fire a priori, FDS provides simplified pyrolysis models to simulate the decomposition of the condensed phase.

Several works related to flame spread simulation using FDS have been conducted. NIST reported investigations of several fire incidents using FDS

[14,15,16]. The Cook County administration building fire in Chicago was examined using FDS V.3 [14]. The material properties used were obtained from the literature or fire experiments. Subsequently, they were adjusted to match the fire growth in the simulation to observations during the fire and the investigation of the post-fire scene.

FDS V.4 was used for the examination of the Station nightclub fire in Rhode Island [15]. Most properties for the primary fuel, polyurethane foam, were estimated from the bench-scale experiments. Only maximum burning rate was determined through a series of simulations. The value of maximum burning rate in FDS was varied and determined by comparing the heat release rate in the numerical simulation with the full-scale mock-up experimental results. Images from video of the incident were compared to the Smokeview images in FDS. The simulation was consistent with the video record during the early stages of fire development.

NIST investigated the collapse of the World Trade Center (WTC) Towers in New York [16]. Four fire scenarios were modeled. Photographs and videos were employed to assess each of the four scenarios in terms of the fire duration and spread rate. The report stated that in general, reasonable agreement between the simulated and observed flame spread rates, were shown, although the fires burned too quickly and too near the perimeter.

In contrast with the above studies, it was reported that FDS as well as other CFD models showed inconsistencies in the predictions of flame spread processes involving an FDS pyrolysis model [17,18,19]. Hostikka and McGrattan [17] studied the coupling of a charring material pyrolysis model to FDS by comparing its predictions to experimental data. The capability of FDS for predicting heat release rate and environmental conditions was evaluated by comparing model predictions to a real-scale spruce panel room/corner flame spread test. Several variations of pyrolysis rate coefficients and grid sizes were tried. Strong grid dependence was observed in the HRR predictions. The maximum HRR deviation between the prediction and the experiment were within

20 %, but none of simulations yielded the same kind of smooth increase as observed in the experimental data.

Carlsson [18] evaluated the performance of different CFD models in wall flow modeling and various pyrolysis models using 3 m particleboard vertical flame spread experiments and a cone calorimeter. The pyrolysis model for charring fuels in the form of a first order Arrhenius equation used in FDS V.2.2 showed the potential of quite correctly and consistently predicting the heat release rate as compared with the cone calorimeter experimental data. However, the FDS predictions of vertical flame spread rate showed significant grid dependencies.

Moghaddam et al. also applied FDS to predict the results of room/corner test [19]. Significantly inconsistent results with grid size variation and the choice of gas phase fuel reaction (ethanol and wood) were shown in the FDS surface flame spread modeling.

To date limited work focusing specifically on vertical flame spread has been conducted to determine the capability of FDS. Liang [20] evaluated FDS V.2 for the flame spread and burning rate predictions using a 5 m PMMA vertical wall panel experiment conducted by Factory Mutual Research Corporation (FMRC) [12]. Figure 1 shows the FDS V.2 flame spread predictions of a 5 m wall experiment compared to the experimental data. The simulation results show the simulated upward flame spread follows the trend of the experimental data. The thermoplastic pyrolysis model used in FDS V.2 was as follows:

$$\dot{m}'' = 0 \quad (T_s < T_{ig}) \quad (3a)$$

$$\dot{m}'' = \frac{\dot{q}_{net}''}{\Delta H_v} \quad (T_s \geq T_{ig}) \quad (3b)$$

where \dot{m}'' , \dot{q}_{net}'' , ΔH_v , T_s , and T_{ig} are the mass loss rate (MLR), the net heat flux, the heat of vaporization, the surface temperature, and the ignition temperature, respectively. This pyrolysis model possesses a “switch”: ignition temperature, or pyrolysis temperature.

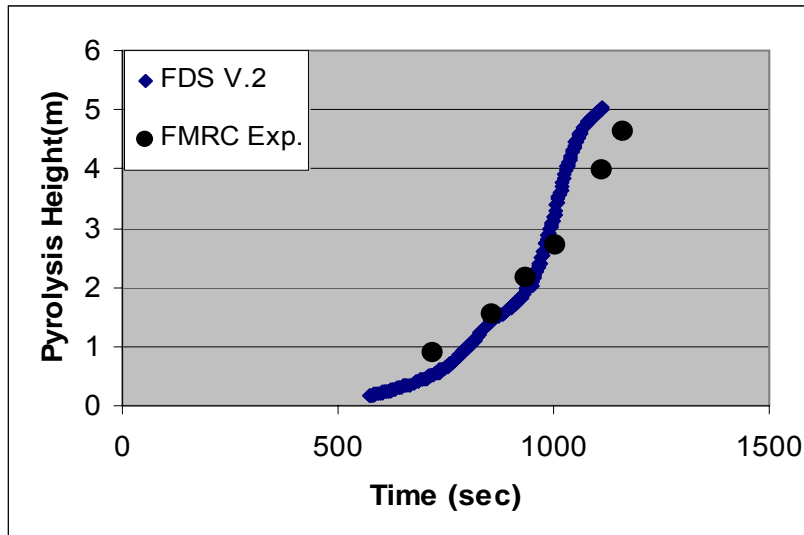


Figure 1 FDS V.2 Flame Spread Predictions of 5 m PMMA Wall Panel Experiment compared to FMRC Experimental Data [12].

Scope of Work

In this work three simulations were conducted to evaluate the capabilities of NIST's FDS V.4 to predict upward flame spread. In the first simulation, the vertical flame spread experiment over a 5 m PMMA panel performed by FMRC [12] is modeled with the default values for FDS input parameters. In the second simulation, the gaseous and condensed phases are decoupled to better assess the gas phase calculation in FDS by directly specifying the burning rate rather than calculating it with the FDS pyrolysis model. In the third simulation, an effort to mitigate the over-predicted flame heights in the first simulation is made by turning off the "AUTOMATIC_Z" feature which locally modifies the stoichiometric value of mixture fraction. The key experimental data and empirical correlations are used to compare against the corresponding FDS outputs. A simplified flame spread model is also applied to assess the simulation results.

Overview of FDS V.4

Hydrodynamic model

Conservation of mass, conservation of momentum, the divergence of velocity (conservation of energy), the perfect gas law, and conservation of mixture fraction are used in FDS V.4 [13]. The low Mach number assumption used in FDS makes possible to use the constant value of background pressure P_0 that filters out acoustic waves.

Turbulence Model

In FDS [13], there are two options to solve for the viscosity μ : Large Eddy Simulation (LES) and Direct Numerical Simulation (DNS). A DNS computation is currently impractical for most large fire applications due to computational costs. In LES, large eddies are computed directly using Navier-Stokes equations while the unresolved small eddies are modeled. In FDS, the Smagorinsky sub-grid scale (SGS) model [21] is employed to represent the small eddy motion.

Combustion Model

If the chemical reaction is assumed to be infinitely fast, all parameters related to finite-rate chemical kinetics from the analysis can be eliminated. From this assumption, the “conserved scalar” parameter, “mixture fraction” is introduced [22]:

$$Z = \frac{sY_F - Y_{O_2} + Y_{O_2,2}}{sY_{F,1} + Y_{O_2,2}} \quad (4)$$

where s is the stoichiometric oxygen to fuel mass ratio, Y_F is the mass fraction of fuel, and Y_{O_2} is the mass fraction of oxidizer. Subscript 1 and 2 indicate fuel stream and oxidant stream, respectively. With a mixture fraction combustion model, the fuel and oxidizer cannot co-exist. The mass fractions of fuel and

oxidizer are simultaneously zero where the flame sheet is formed. Thus, the flame surface, or the “iso-surface” of the stoichiometric mixture, is determined from:

$$Z_{st} = \frac{Y_{O_2,2}}{sY_{F,1} + Y_{O_2,2}} \quad (5)$$

Automatic Z : Adjustment of Stoichiometric value of Mixture Fraction

Flame heights can be underestimated when coarse grids are used [23]. One way to remedy this drawback is to define an effective stoichiometric value of mixture fraction. Therefore, a routine is implemented into FDS [13] with the following relation to enhance the mixture fraction combustion model:

$$\frac{Z_{st,eff}}{Z_{st}} = \min\left(1, C \frac{D^*}{d\delta}\right) \quad (6)$$

Z_{st} and $Z_{st,eff}$ are the ideal stoichiometric value of mixture fraction (Eqn. 5) and the effective stoichiometric value of mixture fraction, respectively. C is an empirical constant of 0.6 and $d\delta$ is grid spacing. D^* is the plume characteristic length (Eqn. 13). As either the grid resolution is finer or the fire size increases, the $Z_{st,eff}$ would approach the ideal stoichiometric value of mixture fraction. The adjustment parameter of the stoichiometric value of mixture fraction, AUTOMATIC_Z, is enabled by default in FDS.

Thermal Radiation Model

Soot that is inevitably generated from most fire cases dominates the thermal radiation from fire and hot gas layers. For all but lightly sooting fuels, it is possible to treat the gas as a gray medium (independent of wavelength) since soot has a continuous radiation spectrum and can be considered a non-scattering material. Thus, the mean absorption coefficient can be reasonably

used. The Radiation Transport Equation for non-scattering gray gas is expressed as:

$$\frac{di'}{dS} = a (i'_b(S) - i'(S)) \quad (7)$$

where i , S , a , and subscript b denote the radiation intensity, coordinate along the path of radiation, the absorption coefficient, and blackbody, respectively.

The source term is given by blackbody radiation intensity [13,24]:

$$i'_b = \frac{\sigma}{\pi} T^4 \quad (8)$$

where σ is the Stefan-Boltzman constant. The use of mean absorption coefficient a results in reducing the amount of computation considerably since the values of a can be tabulated as a function of variables such as gas temperature and mixture fraction by assuming that all species, including soot, are unique functions of mixture fraction. a is pre-calculated in FDS by employing RADCAL [25].

Radiation Inside Flame Zone

As described in Eqn 8, the radiative source term i'_b depends on the temperature raised to the fourth power. Therefore, inaccurate computation of temperature results in large error in the radiation calculation. Especially, temperatures inside the flame zone are under-estimated if the spatial resolution used is not fine enough to resolve the flame since the flame sheet occupies only a small fraction of the cell volume. To compensate for this limitation, FDS provides two options for the calculation of the source term inside the flame zone:

$$a i' = \text{Max} \left(\frac{\chi_{\text{rad}} \dot{q}'''}{4\pi}, \frac{a\sigma T^4}{\pi} \right) \quad (\text{Inside flame zone}) \quad (9)$$

where χ_{rad} is the user specified radiative fraction value. The method employing \dot{q}''' and radiative fraction value is usually dominant as fire grows [26], see Appendix C. Unlike inside flame zone, it is believed that the estimation of temperature outside the flame zone is reliable. Therefore, the radiative source term is determined only from:

$$a i' = \frac{a\sigma T^4}{\pi} \quad (\text{Outside flame zone}) \quad (10)$$

Thermally-Thick Thermoplastic Fuel

In FDS V.4, a one-dimensional heat conduction model for thermally-thick thermoplastic fuel is as follows:

$$\frac{\partial}{\partial t}(\rho c T) = \frac{\partial}{\partial x} \left(k \frac{\partial T}{\partial x} \right) \quad (0 < x < L) \quad (11a)$$

$$-k \frac{\partial T}{\partial x} \Big|_{x=0} = \dot{q}_c'' + \dot{q}_r'' - \dot{m}'' \Delta H_v \quad (11b)$$

$$-k \frac{\partial T}{\partial x} \Big|_{x=L} = 0 \quad (11c)$$

$$T \Big|_{t=0} = T_o \quad (11d)$$

where $\rho, c, k, T, \dot{q}_c'', \dot{q}_r'', \dot{m}'', \Delta H_v$ and T_o are respectively the density of fuel, the specific heat of fuel, the thermal conductivity of fuel, the temperature of fuel, the convective heat flux, the radiative heat flux, the mass loss rate of fuel, the heat of vaporization, and the initial temperature. The mass loss rate of fuel, pyrolysis rate, \dot{m}'' , in FDS V.4 is based on a first order Arrhenius equation with the pyrolysis rate related directly to the surface temperature:

$$\dot{m}'' = A\rho \exp\left(-\frac{E_A}{RT_S}\right) \quad (12)$$

where A , E_A , R , and T_S are the pre-exponential factor (m/s), the activation energy (J/mol), the universal gas constant (J/mol·K), and the surface temperature, respectively. Note that the units of A are m/s instead of s^{-1} because pyrolysis is assumed to occur at the surface. It is noted that in comparison to Eqn. 3a and 3b, there is no temperature below which no fuel is generated for an Arrhenius equation. Note that this pyrolysis model is not the same as that in FDS V.2 used in Liang's work [20]

Experimental Work

Experimental Configuration

Wu et al. [12] conducted a full scale upward flame spread experiment under the FMRC Fire Products Collector. Figure 2 shows the configuration of the 5 m PMMA vertical wall experiment. 0.025 m thick, 0.58 m wide, and 5 m high PMMA slab was used in the experiment. Calcium silicate panels were placed on both sides of the PMMA panel. To minimize the effects of room drafts, a perpendicular 0.6 m flow barrier (24 gauge steel) was placed at the outer edge of calcium silicate panels. A 3 m extension (24 gauge steel) was mounted flush with the PMMA panel to provide a way to measure flame heights above the PMMA panel.

Seven water-cooled heat flux gauges and seven thermocouples (TCs) were placed at various heights on the PMMA wall. The pyrolysis heights were measured by visual observation and TC traces. Additionally, chemical heat release rate was measured.

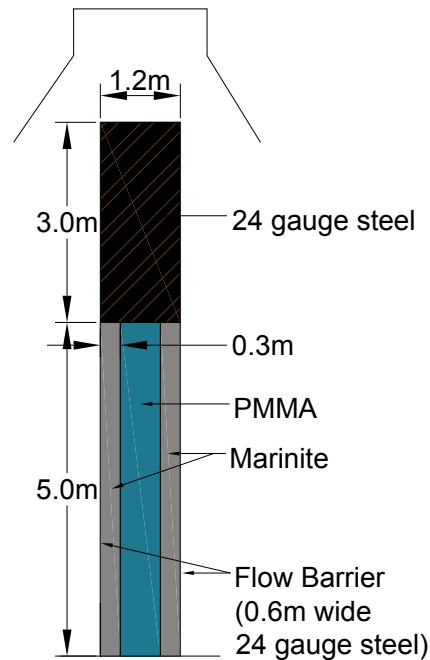


Figure 2 Configuration of 5 m PMMA Wall Panel Experiment under Fire Products Collector [12].

Experimental Data

Figure 3, Figure 4, and Figure 5 present respectively the heat release rate (HRR), the pyrolysis height and heat flux histories over the PMMA panel obtained from the experiment. The heat release rate increases exponentially with time. The pyrolysis height history shows the same trend as the HRR. At about 1200 second, the pyrolysis front reached the top of the PMMA panel. It is evident that there are three phases in the heat flux distribution data (Figure 5). A triangle-like profile is observed at the early stage (around 800 seconds). A top-hat profile with peak values approximately $30\text{-}40\text{ kW/m}^2$ is formed as the flame propagated up the wall between 900 and 1100 seconds. Subsequently, the profile approaches steady state after 1200 seconds.

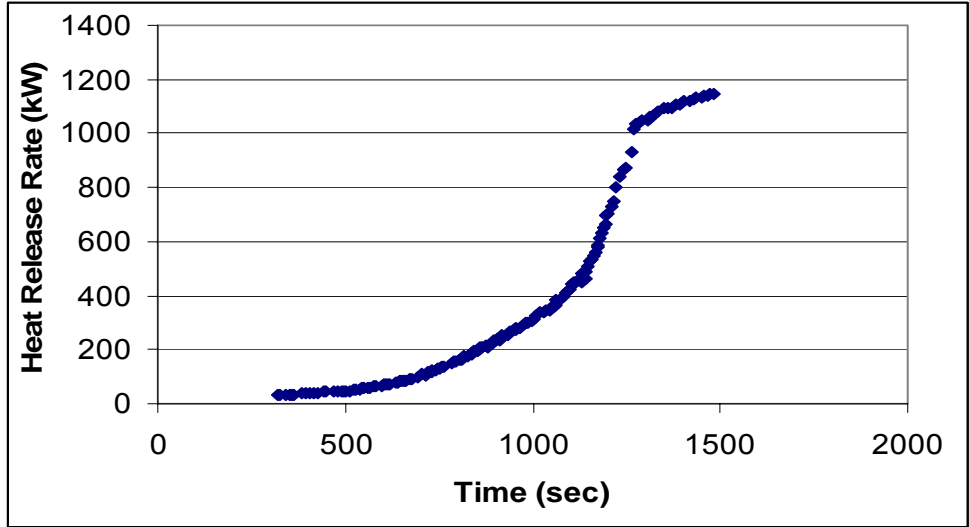


Figure 3 Heat Release Rate History from FMRC Experiment [12].

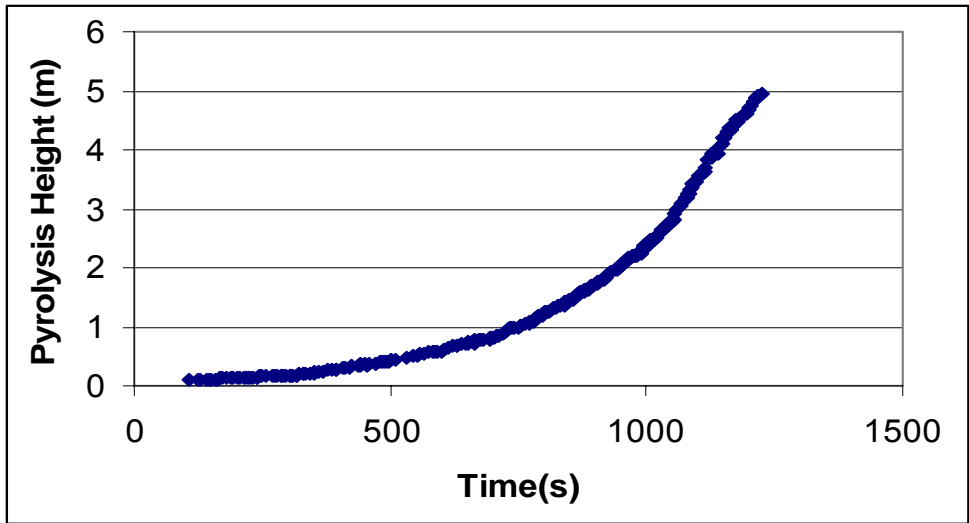


Figure 4 Pyrolysis Height History from FMRC Experiment [12].

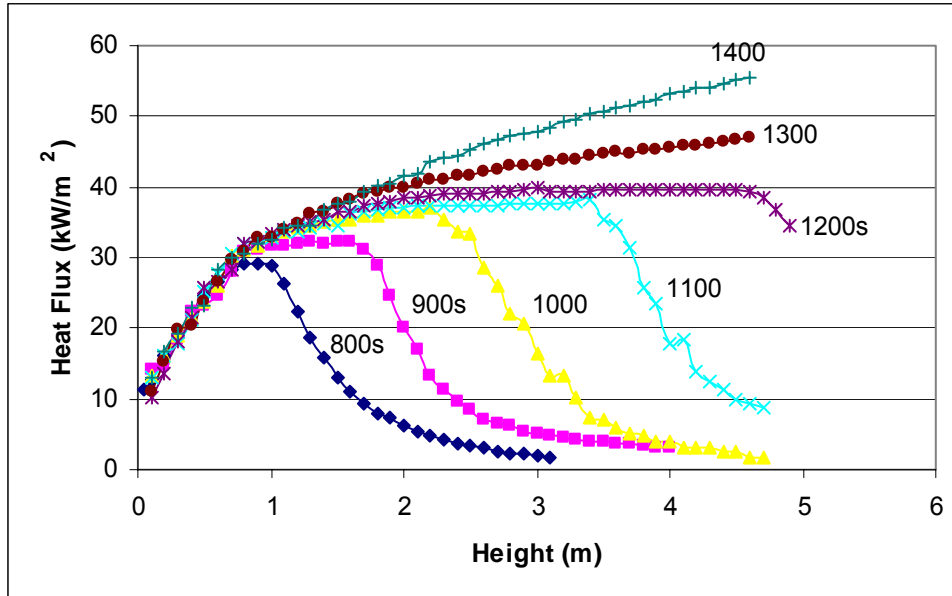


Figure 5. Heat Flux Distribution over PMMA Panel from FMRC Experiment [12].

FDS Input Data

PMMA Panel Simulation

This section presents FDS input data for a PMMA panel simulation. All input parameters not mentioned in this section are the default FDS values.

Geometry

The domain in FDS is constructed as close to the PMMA wall panel experiment as practical (Figure 6). The size of domain is 0.6 m deep, 1.2 m wide, and 8 m high. The 0.025 m thick, 0.6 m wide, and 5 m high PMMA slab is located in the middle of backside wall. The 0.3 m width of calcium silicate panels are placed on both sides of the PMMA panel. The side walls (0.6 m depth) are made of 24 gauge steel to mimic the flow barrier for minimizing the effects of room drafts. A 3 m extension (24 gauge steel) is placed on the top of the PMMA panel. The front and top of domain are open to the exterior ambient.

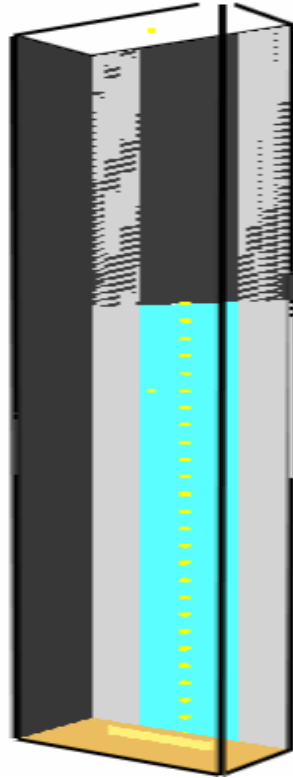


Figure 6 Global View of FDS Domain.

Grid Resolution

Grid size plays an important role in FDS to capture the features of flow and combustion. FDS shows sensitivity to grid size in many applications [15,17,23,27,28,29]. A smaller grid size is preferred for better simulation of both large and small scale dynamics; however, a larger grid size is favored in terms of a computational cost.

According to Ma [23], the optimum resolution is determined as 5 % of plume characteristic length, D^* :

$$D^* = \left[\frac{\dot{Q}}{\rho_\infty c_\infty T_\infty \sqrt{g}} \right]^{2/5} \quad (13)$$

where \dot{Q} , ρ_∞ , c_∞ , T_∞ , and g are respectively the total heat release rate (kW), the density at ambient temperature (kg/m^3), the specific heat of gas ($\text{kJ/kg}\cdot\text{K}$), the ambient temperature (K), and the gravity acceleration (m/s^2).

McGrattan [30] suggested 10 % of plume characteristic length as adequate resolution after careful comparisons with plume correlations. Based on these suggestions, a grid sensitivity analysis was conducted to determine the appropriate grid spacing [26], see Appendix B. The “10 % criterion” satisfies in terms of good predictions balanced with reasonable computational time.

Here, the fire size varies from 0 to approximately 1200 kW, which corresponds to a grid spacing of 0 to 10 cm based on the “10 % criteria”. As it takes account of both fine grids and the computing time, a 2.5 cm grid size is chosen. This grid size results in 368,640 cells in total for the FDS domain. The configuration of personal computer used is 3.6 GHz CPU with 4 GB RAM and the operating system is Windows XP. It takes approximately 12 days to simulate 1300 s real time for a serial (non-parallel) run.

Ignition Source

A 0.6 m wide x 0.05 m deep x 0.1 m high “hot block” is created as an ignition source in the bottom of domain (Figure 7). The distance between the face of the block parallel to the PMMA and the PMMA is 0.2 m. The face of the block parallel to the PMMA is set to 760 °C. These conditions result in a radiative heat flux to the PMMA of approximately 13-15 kW/m^2 to the projected area on the PMMA. This heat flux range is somewhat higher than the critical heat flux for ignition of PMMA in the fire propagation apparatus (FPA) [31]. This radiative heat flux ignites the PMMA panel.

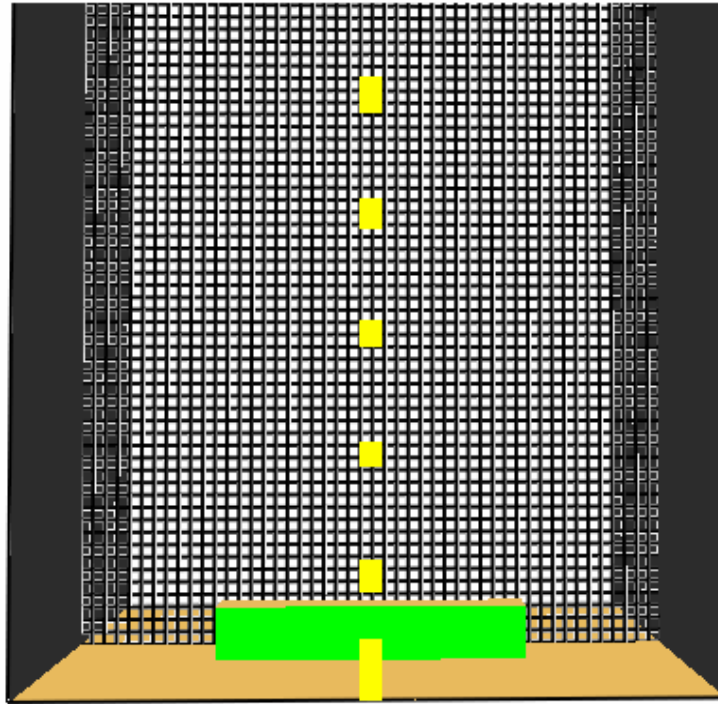


Figure 7 Detail View of FDS Domain. Green block is “hot block” for Ignition.

Material Properties

Sensitivity to material properties in FDS predictions can be seen in the FDS related works [13,14,15]; thus, it is crucial to use the reliable values for material properties. Lee [32] developed a material property estimation method using a one-dimensional heat conduction model and thermoplastic pyrolysis model as implemented in FDS. His model produces a set of FDS input data such as thermal conductivity, specific heat, pre-exponential factor, activation energy, and heat of vaporization. Predictions of the material properties from his model are confirmed by the cone calorimeter experimental data with regards to surface temperature and MLR histories. The cone experimental data in Figure 8 is obtained with an applied heat flux of 50 kW/m^2 and an assumed flame heat flux of 30 kW/m^2 [32].

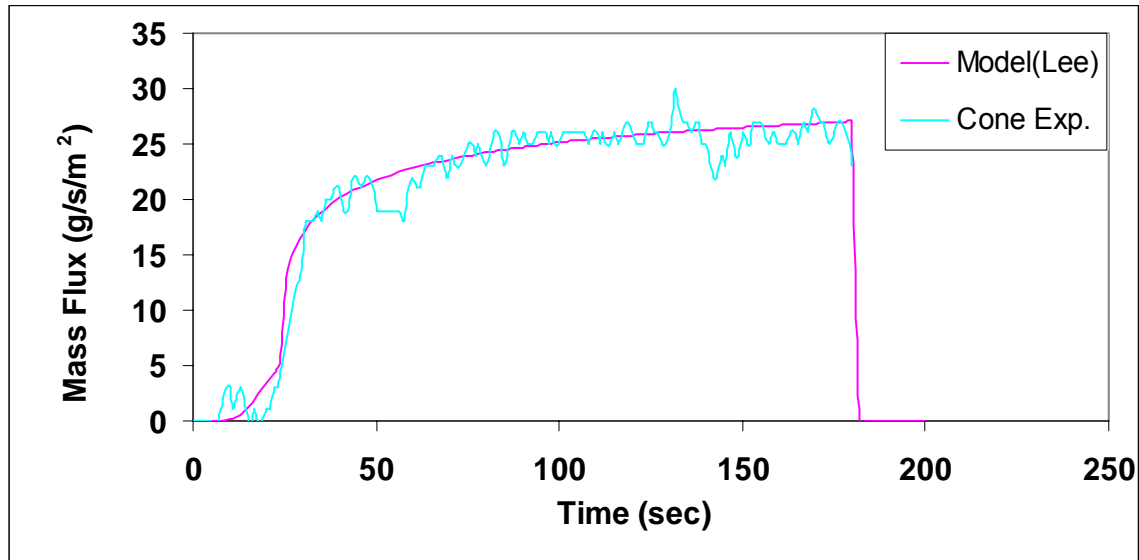


Figure 8 Mass Flux History Comparison between Lee's Model and Experiment for 0.025 m Black PMMA (Applied Heat Flux of 50 kW/m²) [32].

Figure 9 represents the inverse square root of the time to ignition vs. applied heat flux for thermally thick behaving PMMA. A mass flux of 4 g/m²·s is used to determine the time to ignition for Lee's model. The ignition data from Lee's experiment and model is plotted with the values from Beaulieu [33], Tewarson and Ogden [10], and Hopkins and Quintiere [34]. Figure 10 represents the inverse of the mass loss rate vs. applied heat flux for PMMA. The mass loss flux data from Lee's experiment and model is plotted with the values from Beaulieu [33], Tewarson [10], and Hopkins and Quintiere [34]. As can be seen in Figure 9 and Figure 10, Lee's material properties combined with the FDS pyrolysis model reproduce the bench-scale experimental data for PMMA that exists in the literature. Therefore, Lee's material properties can be used with confidence to simulate pyrolysis in the upward flame spread experiment described earlier in the Experimental Work section.

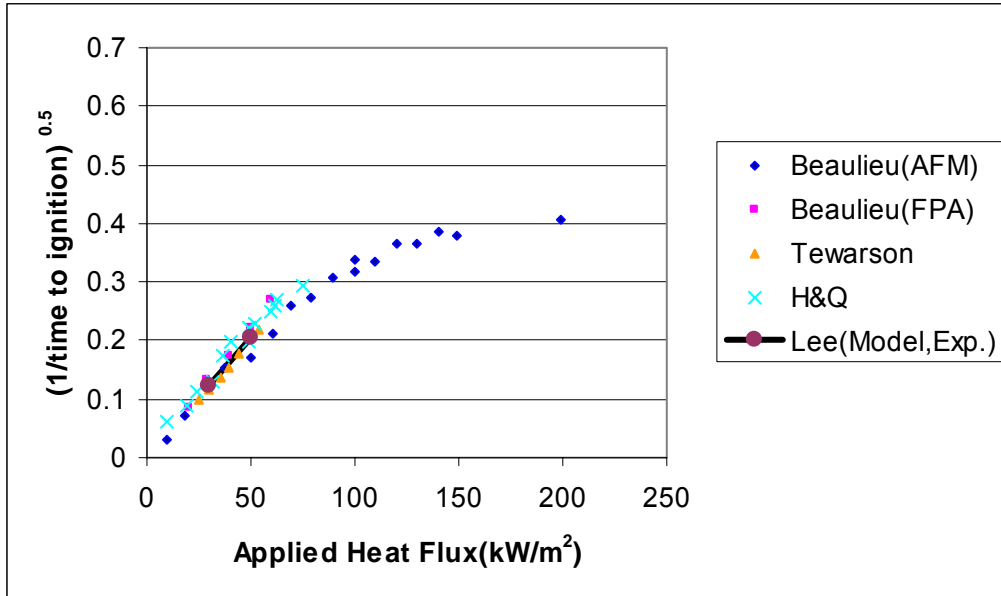


Figure 9 Time to Ignition vs. Applied Heat Flux for Black PMMA, Thickness 0.025 m.

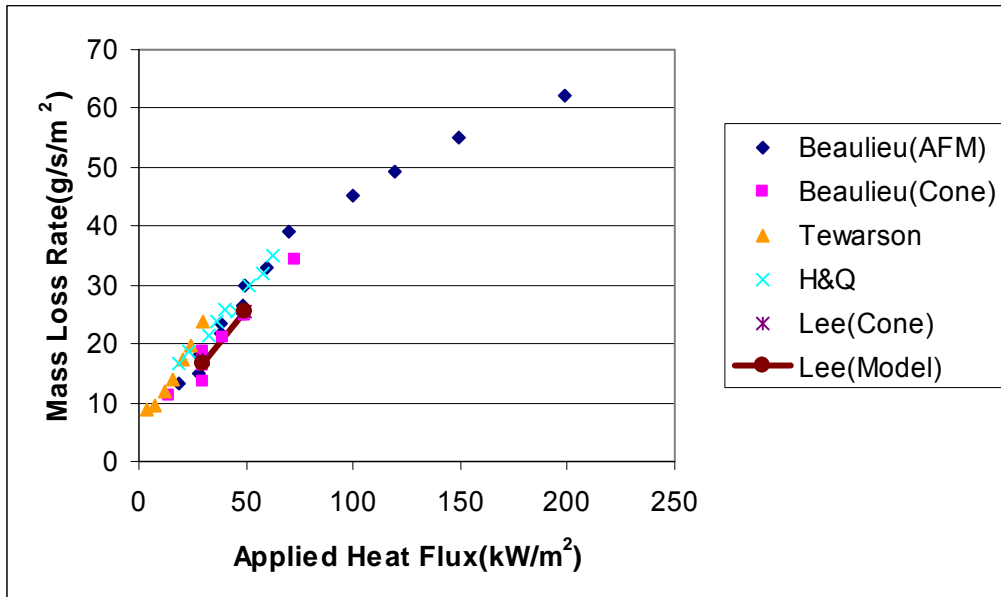


Figure 10 Mass Loss Rate vs. Applied Heat Flux for Black PMMA, Thickness 0.025 m.

The thermal properties for calcium silicate and steel (metal sheet) are used as presented in FDS V.4 database. The thickness of each material is changed,

accordingly to match that used by Wu [12]. The FDS input data for the PMMA panel simulation is presented in Appendix F.

Results and Discussion

PMMA Panel Simulation

Heat Release Rate and Pyrolysis Height

The heat release rate and pyrolysis height comparisons between the 5 m PMMA wall panel experiment and FDS simulation are presented in Figure 11 and Figure 12, respectively. The time axis in the experimental data is shifted to correspond to the simulation at a HRR of approximately 30 kW. For the criterion determining pyrolysis height, a critical mass flux is used because of the continuous pyrolysis model in FDS. Bamford [35] introduced the concept that a critical mass flux is an ignition criterion. Tewarson [36] reported $1.9 \text{ g/m}^2\text{s} \leq \dot{m}''_{critical} \leq 3.9 \text{ g/m}^2\text{s}$ for thermoplastics under natural convection and $2.9 \text{ g/m}^2\text{s} \leq \dot{m}''_{critical} \leq 4.5 \text{ g/m}^2\text{s}$ for thermoplastics under forced convection. Deepak and Drysdale [37] obtained $\dot{m}''_{critical} \approx 4 \sim 5 \text{ g/m}^2\text{s}$ for PMMA. Thompson and Drysdale [38] reported $0.8 \text{ g/m}^2\text{s} \leq \dot{m}''_{critical} \leq 2.9 \text{ g/m}^2\text{s}$ for thermoplastics. Here, a pyrolysis height criterion of $4 \text{ g/m}^2\text{s}$ is chosen as obtained for PMMA in Ref. [37]. Note that $\dot{m}''_{critical}$ is strongly dependent on apparatus used. However, for tracking the pyrolysis zone location in this study, the choice of $\dot{m}''_{critical}$ is not critical as long as it is used consistently.

As can be seen from Figure 11 and Figure 12, the velocity of flame spread in the experiment increases with time, while FDS predicts a nominally linear increase and a subsequent “jump”. FDS shows promise for predicting upward flame spread. Upward flame spread across a PMMA panel is simulated, and the magnitude of the maximum HRR in the PMMA panel is comparable to that in an FMRC experiment. However, the FDS predictions for flame spread do not show the trends of the experimental data.

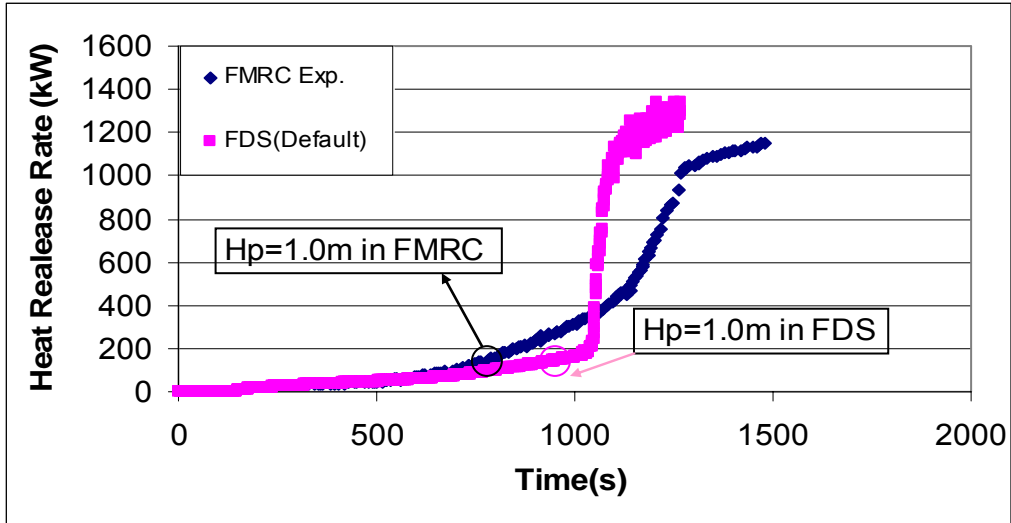


Figure 11 Heat Release Rate Comparison between the FMRC Experiment [12] and Simulation.

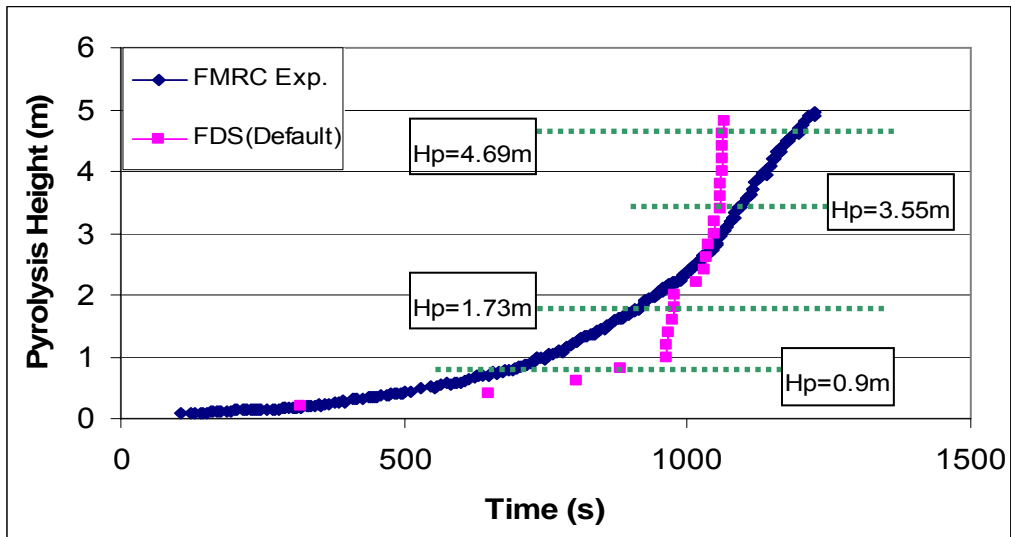


Figure 12 Pyrolysis Height Comparison between FMRC Experiment [12] and Simulation.

Flame Heights and Heat Fluxes

The heat flux distribution comparisons at the same pyrolysis height between the experiment and simulation are presented. GAUGE_HEAT_FLUX in FDS is used to compare with experimental data. It is the most appropriate to use for

comparison with data using water-cooled heat flux gauges. Note that there is an issue between the calibration of heat flux gauge and its use in a wall fire as the calibration environment is different. Figure

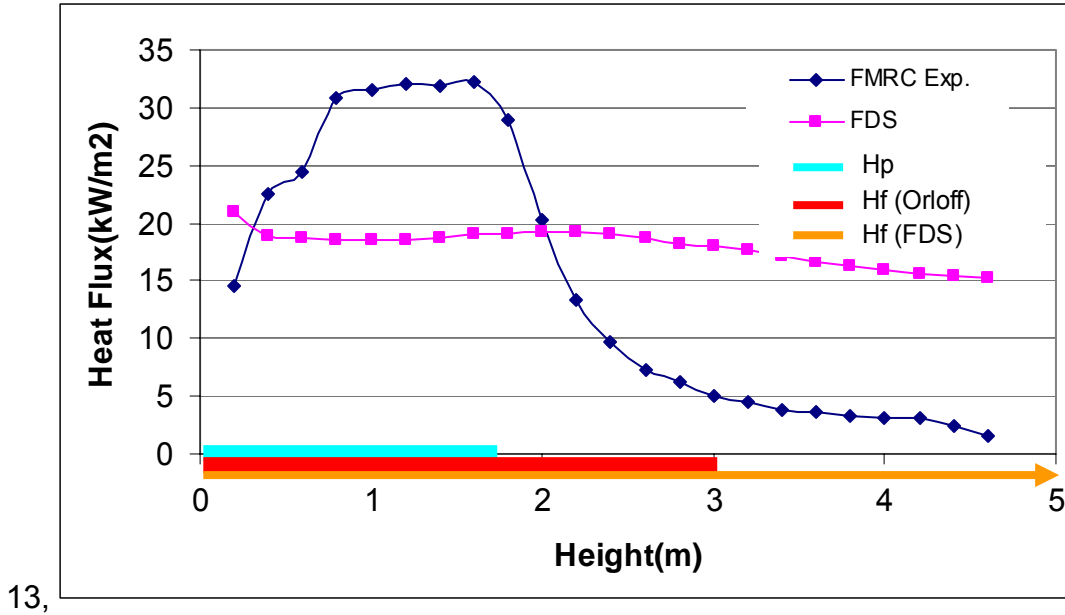


Figure 14, Figure 15, and Figure 16 show heat flux vs. height at the pyrolysis height of 0.9 m (prior to “jump”), 1.73 m (early stage in “jump”), 3.55 m (late stage in “jump”), and 4.69 m (“jump” aftermath) as indicated in Figure 12. In addition, the length scales of flame heights and pyrolysis height are added in the height axis as colored bars. The criterion for flame height for FDS data is the 99.99 % heat release rate locus [20]. Using the recorded slice file for \dot{Q}''' for the entire domain, the value of \dot{Q}''' is accumulated with elevation. The point at which the accumulative \dot{Q}''' reaches 99.99 % of total heat release rate is determined as flame tip. Orloff’s flame height empirical correlation for PMMA [9] is used to estimate flame height for the experimental data:

$$H_f = 5.346H_p^{0.781} \quad (14)$$

where H_f and H_p are flame height and pyrolysis height in cm, respectively.

Prior to “jump” and in the early stage of “jump”, FDS predicts lower heat flux values in the burning zone as represented in Figure 13 and

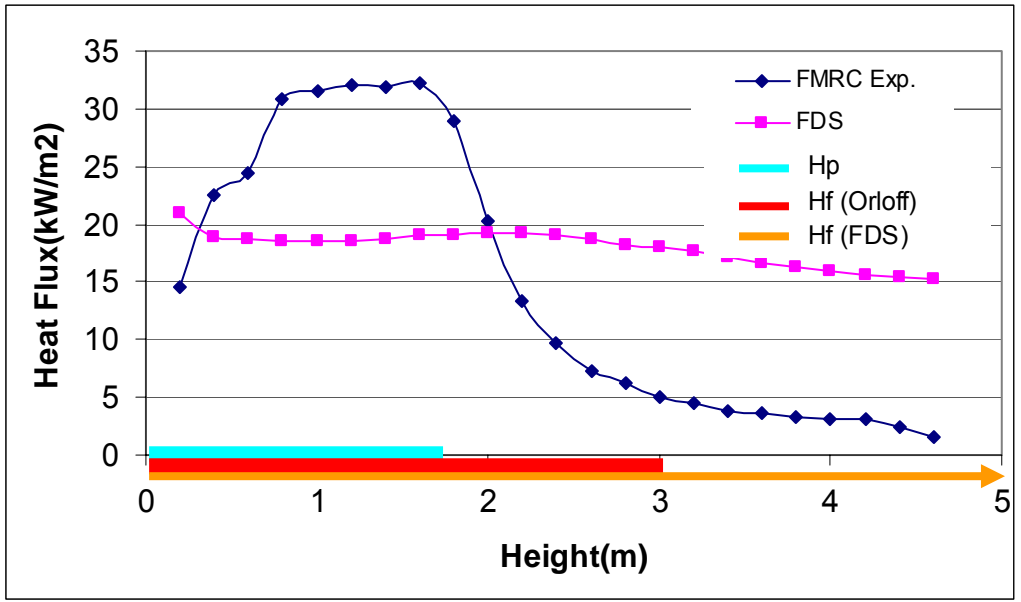


Figure 14; on the other hand, the heat fluxes above the pyrolysis height in FDS don't drop as the experimental data shows. Figure 13 and

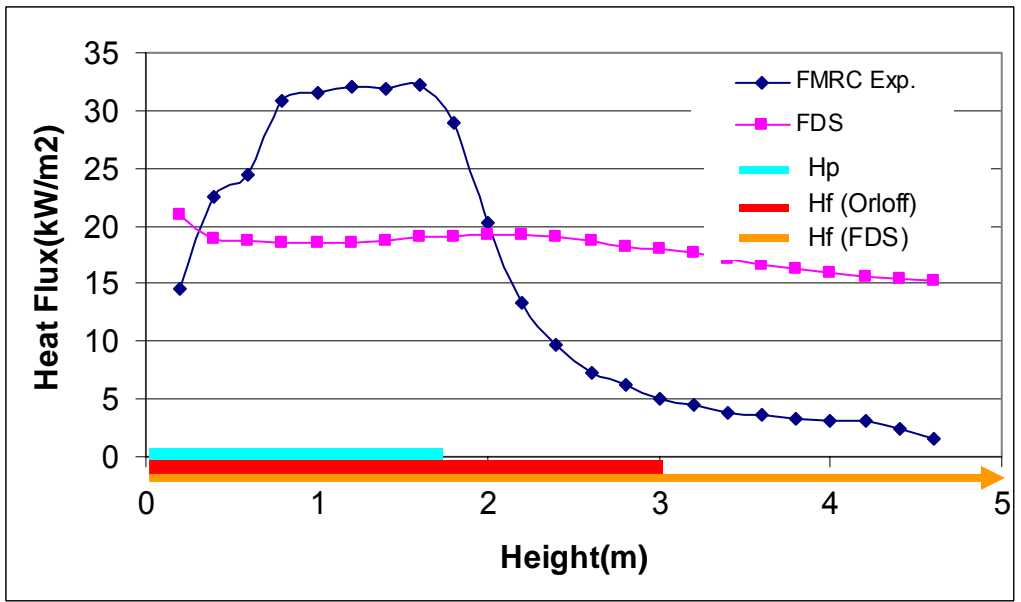


Figure 14 show that the overestimated flame heights lead to the relatively high heat fluxes above the pyrolysis zone. As can be seen in Figure 13, the flame height in FDS is beyond 5 m while the height from the correlation is about 1.8 m.

As the fire develops, the FDS predictions compare more favorably to the experimental data (See Figure 15 and Figure 16).

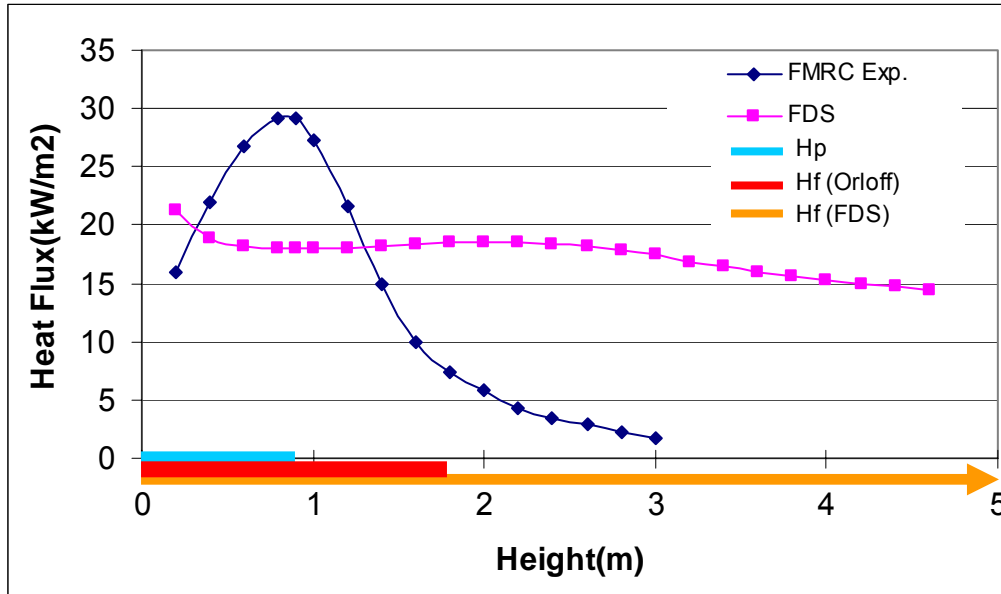


Figure 13 Heat Flux Comparison between FMRC Experiment [12] and FDS Simulation at Pyrolysis Heights of 0.9m.

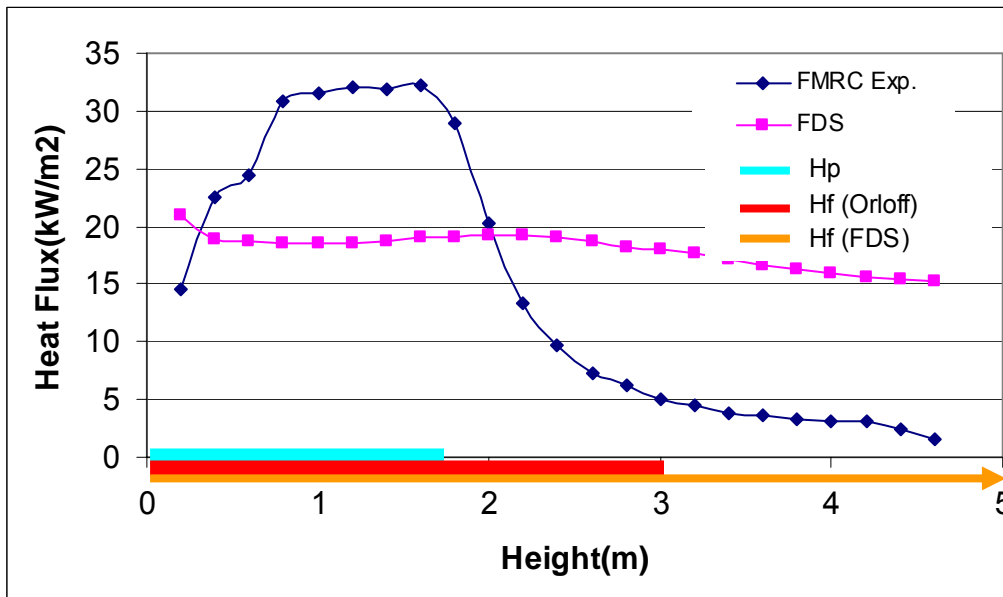


Figure 14 Heat Flux Comparison between FMRC Experiment [12] and FDS Simulation at Pyrolysis Heights of 1.73m.

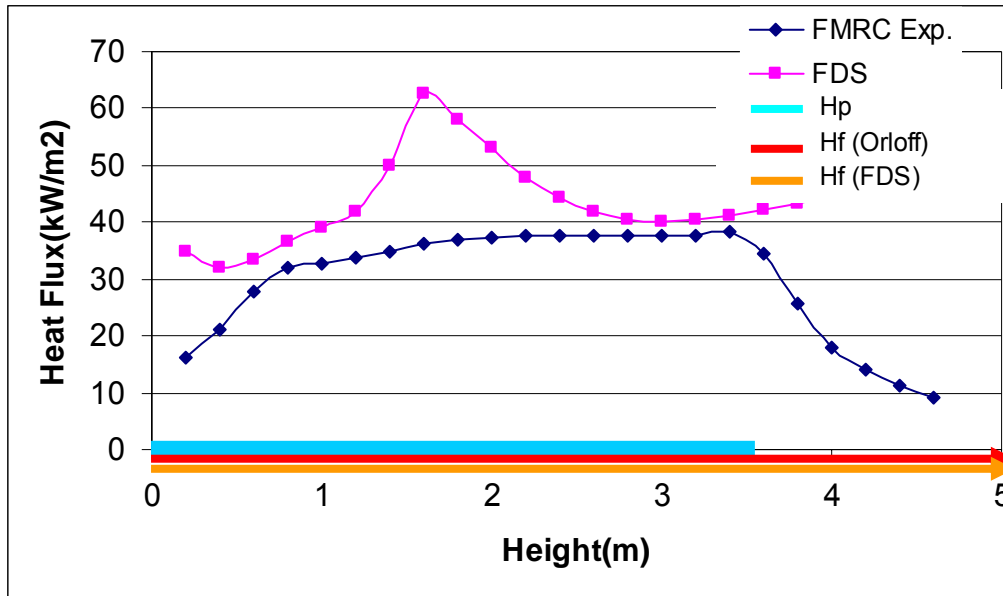


Figure 15 Heat Flux Comparison between FMRC Experiment [12] and FDS Simulation at Pyrolysis Heights of 3.55m.

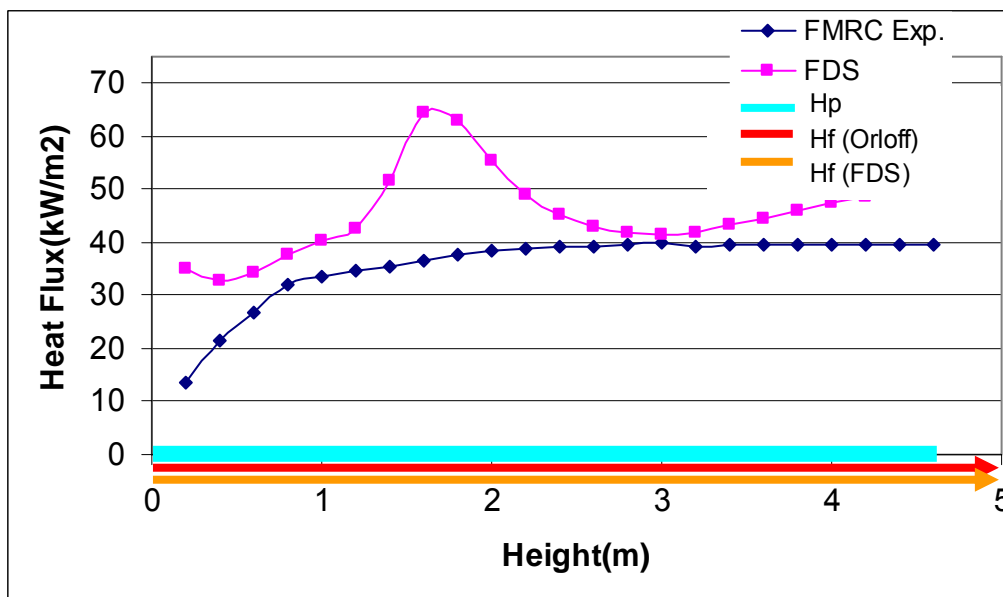


Figure 16 Heat Flux Comparison between FMRC Experiment [12] and FDS Simulation at Pyrolysis Heights of 4.69m.

Forward Heating Zone Length

In the previous section, the overestimated flame heights cause inaccurate heat fluxes to the solid surface. Similarly, the forward heating zone length L_C in the FDS simulation is investigated and compared to that obtained from the experiment and the Orloff's empirical correlation (Eqn. 14).

With the assumption of constant flame heat flux over the forward heating zone (See Figure 17), the L_C can be expressed as [39]:

$$L_C = H_f - H_p = V \cdot \tau \quad (15)$$

where V is the flame spread velocity and τ denotes the ignition time related to the flame heat flux.

For the FDS data, the flame spread velocity is calculated from the slope of pyrolysis front from Figure 12. It is assumed that a heat flux of 20 kW/m² is applied in the early and intermediate stage of flame spread, followed by 40 kW/m² (See Figure 13 to Figure 16). With these heat fluxes, ignition times of 78 and 30 seconds are extracted from the FDS pyrolysis model in Lee's work [32]. For the experimental data, the flame spread velocity is also calculated as the slope of pyrolysis front from Figure 12. As can be seen in Figure 5, the heat fluxes range from 30 to 40 kW/m². Therefore, a median value of 35 kW/m² is chosen to determine the ignition time. The ignition time is calculated using the following relationship [31]:

$$\sqrt{\frac{1}{\tau}} = \frac{(\dot{q}_e'' - CHF)}{TRP} \quad (16)$$

where \dot{q}_e'' , CHF, and TRP indicate respectively the applied heat flux, the critical heat flux, and the thermal response parameter. The values of CHF and TRP used are 11 kW/m² and 274 kW·s^{1/2}/m², respectively [31].

The forward heating zone lengths L_c obtained are plotted as a function of pyrolysis height in Figure 18. Consistent with the flame height comparisons in Figure 13 to Figure 16, the forward heating zone in FDS is significantly overestimated during the early stage in “jump”. This overestimated L_c results from the rapid spread of the “jump”. From the intermediate stage of the “jump”, the L_c is comparable to the experimental data and the empirical data.

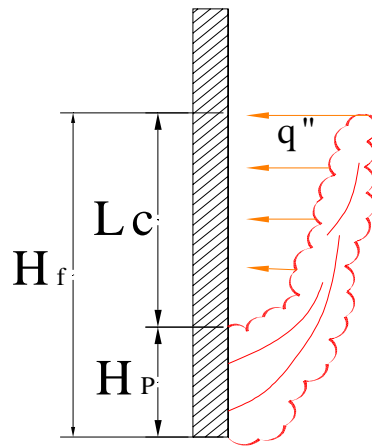


Figure 17 Schematic Diagram of Upward Flame Spread.

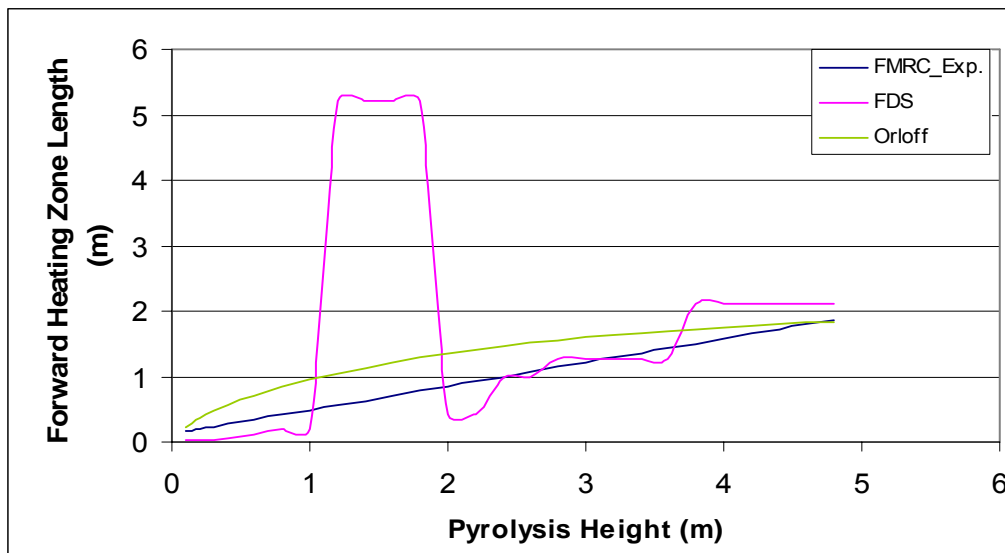


Figure 18 Forwarding Heating Zone vs. Pyrolysis Height for FMRC Experiment [12], FDS Simulation, and Orloff Correlation [9].

Mass Loss Rate

The FDS MLRs are integrated horizontally at each level and are plotted as a function of the height in Figure 19. Figure 19 shows mass loss rate vs. height at the pyrolysis height of 0.9 m (based on the $4 \text{ g/m}^2\text{s}$ criterion).

It is clear that a substantial amount of mass is released above the pyrolysis zone. As described earlier, the Arrhenius equation produces mass as a continuous function of surface temperature. This plays a great role in distinguishing the current works using FDS V.4 from Liang's [20] using FDS V.2 in which no pyrolysis occurs until the surface temperature reaches ignition temperature.

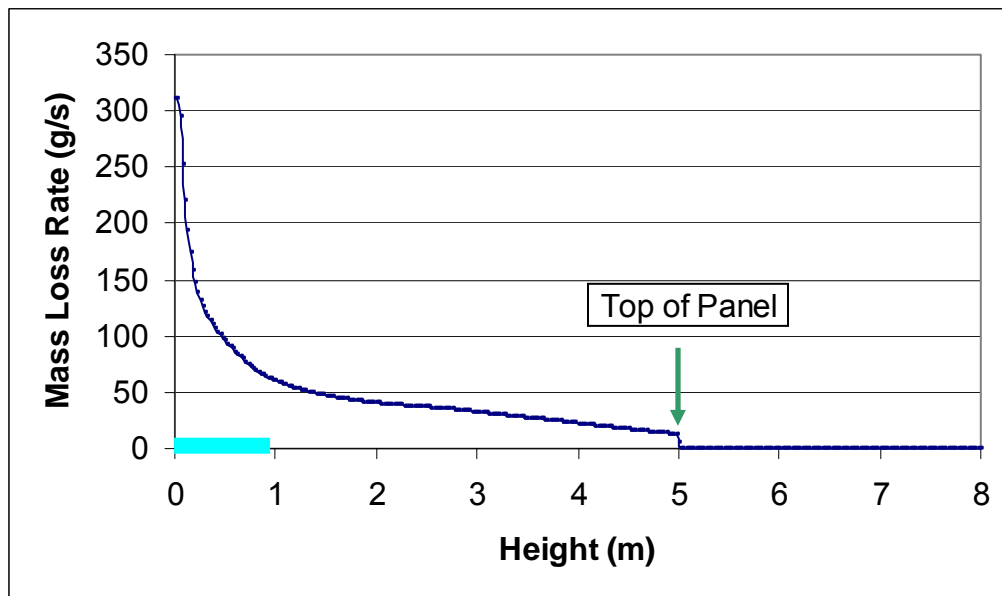


Figure 19 FDS Simulated Mass Loss Rate vs. Height at Pyrolysis Height of 0.9 m.

MMA Burner Simulation

As can be seen in the previous section, there is a significant deviation between the FDS predictions for the PMMA panel simulation and the FMRC experimental data. In this section, the gas and the condensed phases are decoupled to better assess the FDS gas phase calculation. A steady state MMA gas burner is used for further investigation.

As indicated in Figure 11, when the pyrolysis height is 1 m, the HRR is approximately 146 kW in both experiment and PMMA panel simulation. For comparison purposes, the PMMA panel is replaced by the MMA burner (0.6 m x 1 m high), and the 146 kW fire is prescribed directly (Figure 20). The size of burner is analogous to the pyrolysis zone in the PMMA panel simulation. The other set-up remains the same as the PMMA panel simulation.

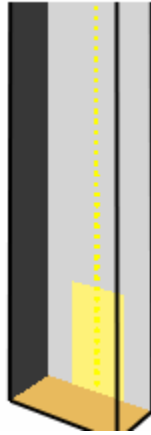


Figure 20 View of MMA Burner Simulation Domain.

The comparison of heat release rate per unit volume (HRRPUV) distributions between the MMA burner and PMMA panel simulation with the same pyrolysis height and total HRR are shown in Figure 21. In Figure 21, a 2D HRRPUV Plot3D contour parallel to the PMMA panel and located 0.025 m in front of the panel is shown. It is obvious that there is a wide flame height difference between two simulations. In Figure 22, flame height vs. pyrolysis height is plotted for the two FDS simulations as well as the empirical correlations from Saito [40] and Orloff [9]. The criterion for flame height, again, is the 99.99 % heat release rate locus. Figure 22 clearly shows the prediction from the gas burner simulation matches well with the empirical correlations while the flame height in the PMMA panel is overestimated. The burning behavior in the PMMA panel simulation is due to the combined effects of the combustion model (mixing controlled) and pyrolysis model (transitioning from surface temperature (kinetically) limited MLR to heat flux limited MLR) in FDS. The PMMA panel is

continuously undergoing pyrolysis. Once the PMMA pyrolyzates meet with oxygen in the right proportion, flames form. This results in the distortion of the HRRPUV distribution as shown in Figure 21. As described in Eqn. 9, the radiation heat distribution is distorted by the unreasonably extended HRRPUV distribution.

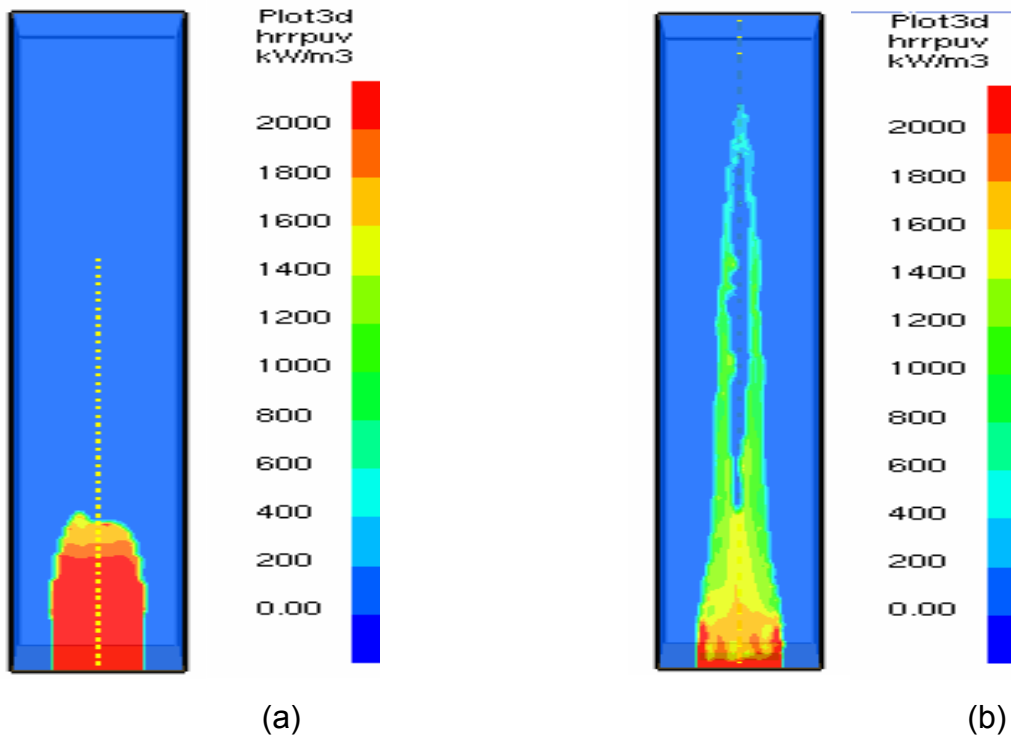


Figure 21 HRRPUV PLOT3D Snapshots ($H_p=1\text{m}$, $HRR=146\text{kW}$) from:
(a) MMA Burner Simulation (b) PMMA Panel Simulation.

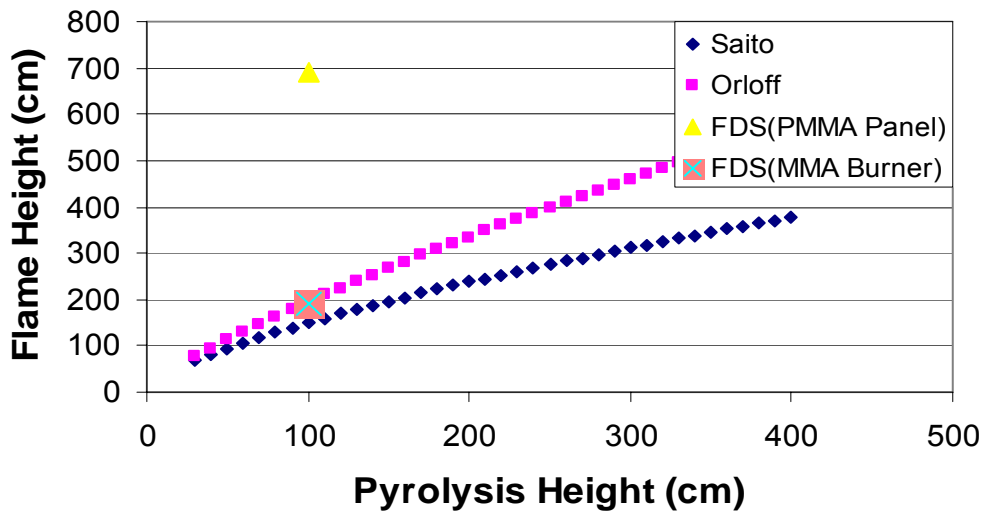


Figure 22 Flame Height vs. Pyrolysis Height for FDS Simulations and empirical correlations [9, 40].

A comparison of heat flux distributions between the FMRC experiment, PMMA panel simulation, and MMA burner simulation are made in Figure 23. As shown earlier, the relatively lower heat fluxes in the pyrolysis zone and the relatively higher heat fluxes above the pyrolysis zone are observed in the PMMA panel simulation. However, heat fluxes from the burner simulation are more comparable to the experimental data. The somewhat high heat fluxes at 0.2 m height in the FDS simulations are partly due to the radiation from the “hot block”.

It is presumed that the favorable agreement in Liang’s work is due to the existence of a “switch” in the pyrolysis model in FDS V.2. As described in the Background section, no mass is produced unless a surface temperature has reached an ignition temperature. This eliminates the possibility of the formation of flames to an unreasonable extent when the Arrhenius based pyrolysis model is coupled with a mixture fraction combustion model.

An effort to replicate the “switch” was made by setting a high activation energy E_A and a high pre-exponential factor A as inputs for the pyrolysis model in FDS V.4. One set of material properties with a high E_A and a high A is tried,

but was not successful in reproducing the experimental data. The details regarding this simulation are presented in Appendix E.

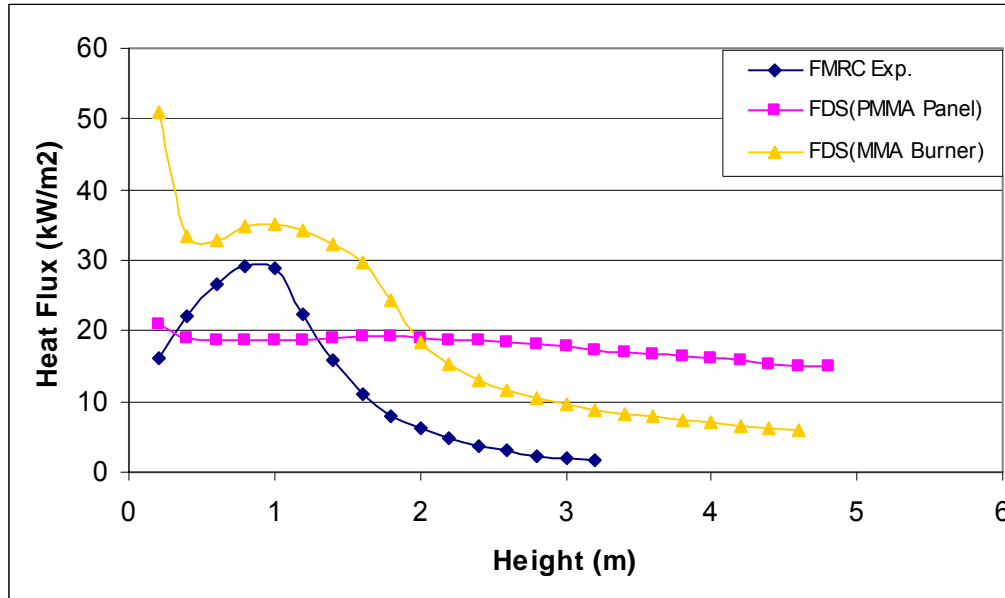


Figure 23 Heat Flux Distribution Comparison with FMRC Experiment 12], PMMA Panel Simulation, and MMA Burner Simulation.

“AUTOMATIC_Z” disabled PMMA Panel Simulation

As described earlier, the stoichiometric value of mixture fraction is redefined to lengthen flame height based on grid size and fire HRR. As can be seen in the previous work, the over-estimated flame height plays a significant role in the FDS predictions; therefore, a further investigation is made by disabling the “AUTOMATIC_Z” feature. This feature is enabled by default in FDS. The other FDS input data remains the same as for the PMMA panel simulation.

Heat Release Rate and Pyrolysis Height

Figure 24 and Figure 25 represent comparisons of heat release rate and pyrolysis height history. By turning “AUTOMATIC_Z” off, the event of “jump” does not occur; however, the flame propagates to the tip of the panel after only a short

period of time. FDS shows significant sensitivity to the “AUTOMATIC_Z” feature in the prediction of vertical flame spread on solids.

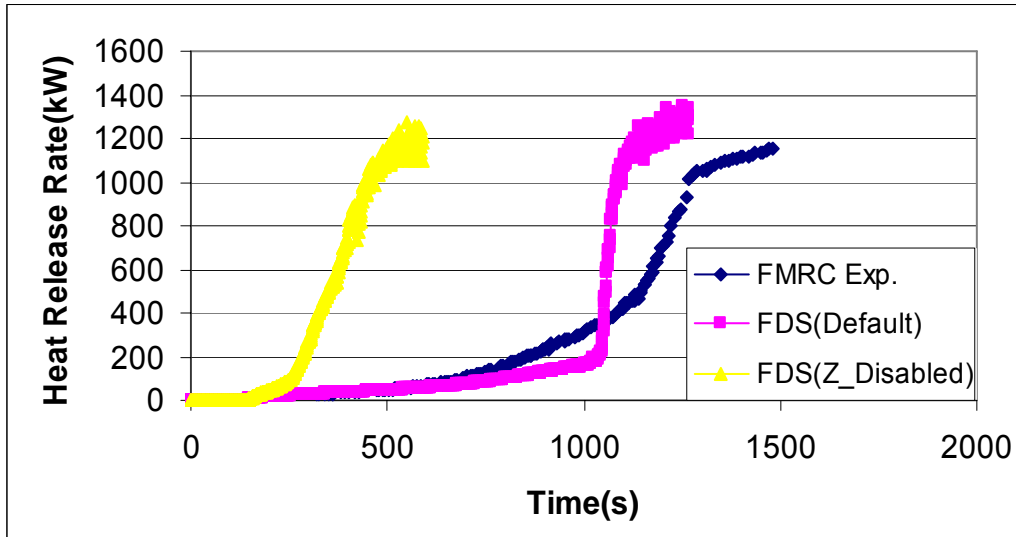


Figure 24 Heat Release Rate History Comparison between FMRC Experiment [12] and FDS Simulations.

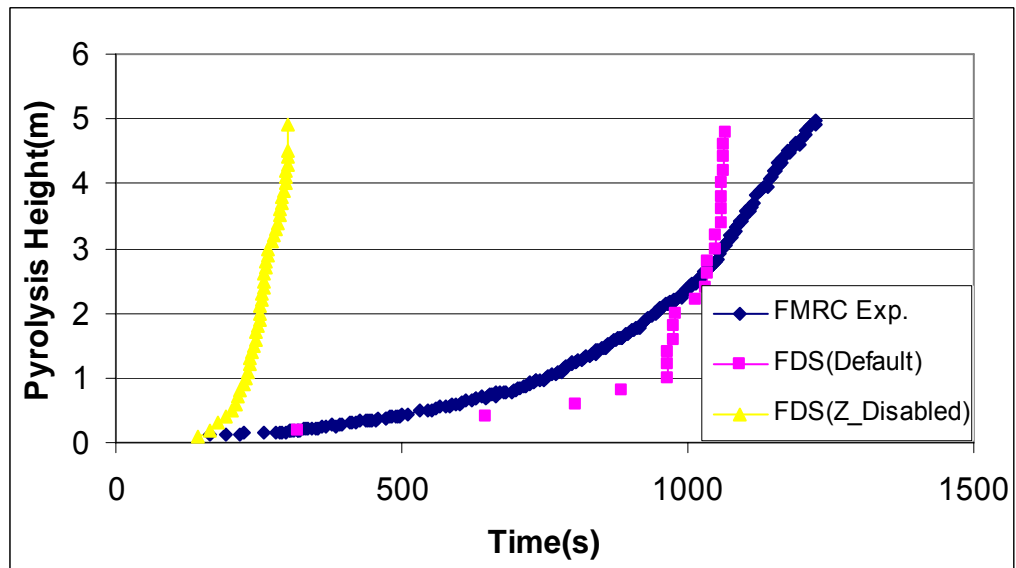


Figure 25 Pyrolysis Height History Comparison between FMRC Experiment [12] and FDS Simulations.

Flame Heights and Heat Fluxes

The FDS results with “AUTOMATIC_Z” enabled were first presented in Figure 13 and are reproduced in Figure 26. The heat fluxes in the “AUTOMATIC_Z” disabled simulation show a good agreement with the experimental data. Also, the flame height of 2.3 m is measured using the 99.99 % HRR criterion. It is reduced substantially compared to “AUTOMATIC_Z” enabled simulation, but is still higher than the value from the empirical correlation. The “AUTOMATIC_Z” feature is problematic for this type of fire scenario. While the “AUTOMATIC_Z” feature is built in for a better estimation of flame height, there is a possibility that flames appear below a lower flammable limit (LFL) by changing the ideal stoichiometric mixture fraction value.

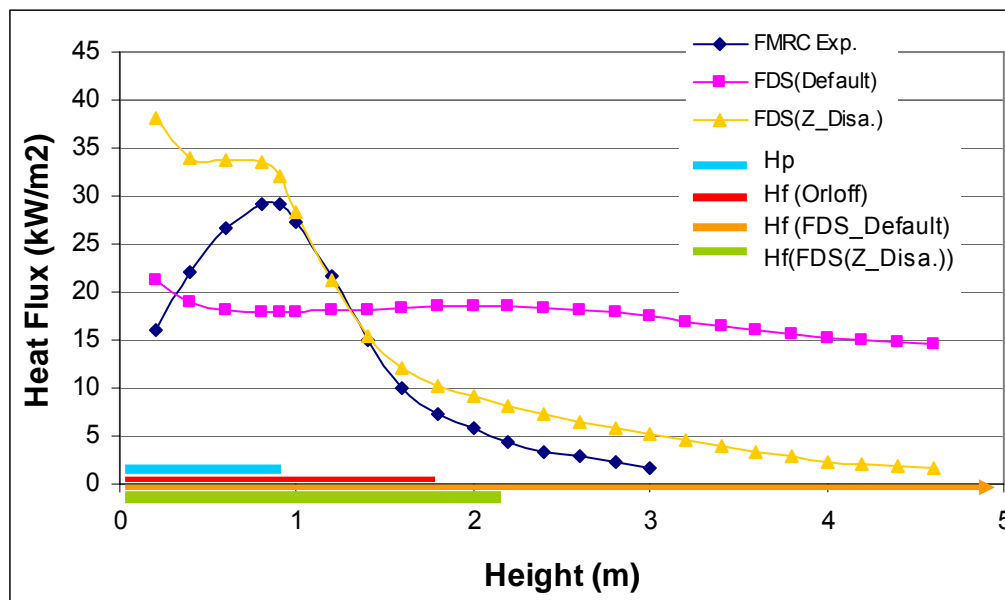


Figure 26 Heat Flux Comparison between FMRC Experiment [12] and FDS Simulations with Flame Heights at Pyrolysis Height of 0.9m.

Simplified Flame Spread Model

The previously discussed FDS simulations show inconsistency for the flame spread predictions. In this section, a simplified flame spread model is used

to identify the reasons for inconsistency. The flame spread velocity can be expressed as [39]:

$$V = \frac{L_c}{\tau_{ig}} = \frac{H_f - H_p}{\tau_{ig}} \quad (17)$$

L_c is the characteristic length (See Figure 17) and τ_{ig} is the characteristic time to ignition. The characteristic time to ignition is a function of forward heating zone heat flux that is assumed to be a constant over the forward heating zone. Eqn. 17 can be used to solve for τ_{ig} based on determining $H_f - H_p$ and V . If Eqn. 17 is rearranged for the characteristic time to ignition:

$$\tau_{ig} = \frac{H_f - H_p}{V} \quad (18)$$

In order to obtain τ_{ig} , the measured pyrolysis heights from the experiment and the simulations are used. The flame spread velocity is from the slope of pyrolysis front in Figure 25. The flame heights for the experimental data and FDS data are obtained using Eqn. 14. The same criterion for flame height needs to be employed to eliminate the effects of an overestimated flame height in FDS. The comparisons of time to ignition data for the experiment and the two FDS simulations (enabled and disabled "AUTOMATIC_Z") are presented in Figure 27. The inverse square root of the time to ignition vs. time is plotted for thermally thick behaving PMMA.

A linear relationship between the inverse square root of the time to ignition and the applied heat flux is found from Figure 9. Using this relationship, the time to ignition data presented in Figure 27 is translated into averaged forward heating zone heat fluxes, and the results are shown in Figure 28. In Figure 28, the measured average heat fluxes over the forward heating zone are added to confirm the values from the simplified flame spread model. For each simulation,

the heat flux values from the simplified flame spread are reasonably consistent with those directly measured.

In Figure 28, compared to the experimental data, the PMMA FDS wall simulation (AUTOMATIC_Z enabled) initially results in lower heat fluxes to the forward heating zone and results in higher heat fluxes as the HRR grows. These results provide insight to an occurrence of the initial low flame spread velocity and a subsequent “jump” in the PMMA panel simulation. In the case of “AUTOMATIC_Z” disabled FDS simulation, higher heat fluxes are applied to the forward heating zone initially, which causes very rapid flame spread.

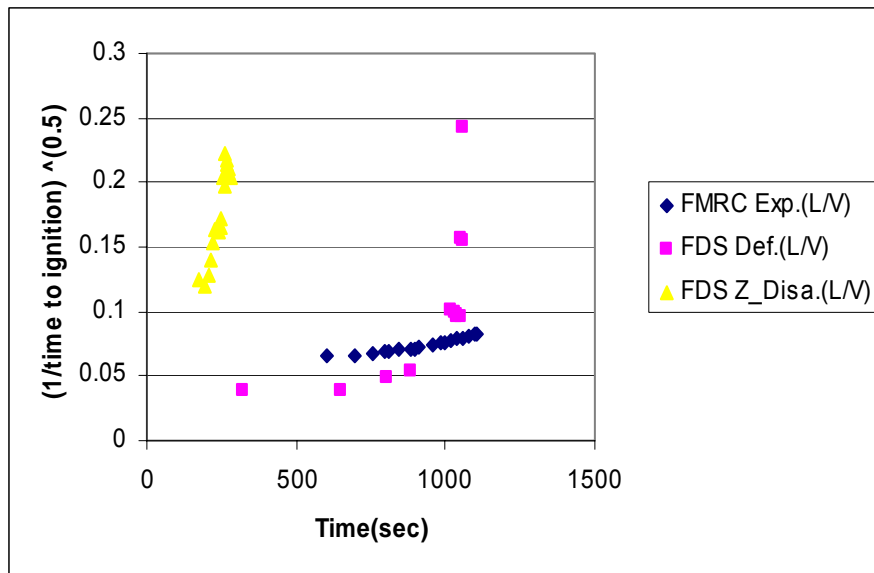


Figure 27 Comparisons of Time to Ignition Data (FMRC Experiment [12] and AUTOMATIC_Z enabled and disabled PMMA Panel Simulations).

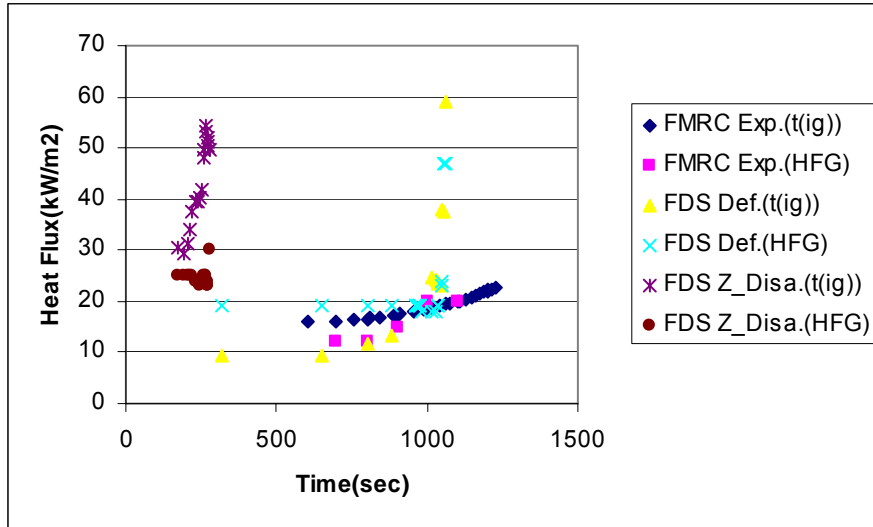


Figure 28 Forward Heating Zone Heat Fluxes from Time to Ignition Data and Direct Measurements (FMRC Experiment [12], and “AUTOMATIC_Z” enabled and disabled PMMA Panel Simulations)

Conclusion

To evaluate FDS V.4 capabilities relative to upward flame spread prediction, three FDS simulation results are compared to FMRC experimental data [12] and empirical correlations.

In this study, FDS shows promise for predicting upward flame spread, however, FDS should be used with caution and the results considered carefully when used for real world fire spread scenarios. Upward flame spread across a PMMA panel is simulated, and the magnitude of the maximum HRR in the PMMA panel simulation is comparable to that in an FMRC experiment [12]. However, the FDS predictions for flame spread do not show the trends of heat release rate and pyrolysis history in the FMRC experiment. The combined effects fuel being generated as a continuous function of surface temperature and the mixture fraction combustion model cause overestimation of the flame height, and distort the distribution of heat release rate per unit volume and the subsequent heat flux distribution.

Unlike the PMMA panel simulation involving a pyrolysis model, the FDS predictions from the gas burner simulation that has a fixed burning rate show good agreement with the experimental data and empirical correlations. The different heat release rate per unit volume distributions between the PMMA panel simulation and gas burner simulation show the problem in the coupling of pyrolysis model and gas phase combustion model in FDS.

It maybe possible to improve the flame spread predictions of FDS by modifying the coupling between the pyrolysis model which generates fuel as a continuous function of surface temperature and the “mixed is burned” combustion model. As can be seen in Liang’s work [20], the pyrolysis model with ignition temperature “switch” appears to be better matched to the gas phase mixture fraction combustion model.

In addition, the PMMA panel simulations with the enabled and disabled “AUTOMATIC_Z” feature show significant inconsistency for the flame spread predictions. The “AUTOMATIC_Z” feature is problematic for this type of fire scenario. While the “AUTOMATIC_Z” feature is built in for a better estimation of flame height, there is a possibility that flames appear below a lower flammable limit (LFL) by changing the ideal stoichiometric mixture fraction value.

From a practical point view, FDS V.4 inconsistencies for the prediction of upward flame spread on surfaces noted in this work suggest that the use of FDS in fire growth scenarios should be considered carefully. Upward flame spread is simulated and fire maximum HRR appears to be reasonable; however, the predicted rate of fire growth does not appear to be reliable due to the combined effects from the FDS V.4 pyrolysis model and combustion model. The most reliable way to assess the effects of fire growth would be to use a “gas burner” to approximate fire growth.

References

- [1] J. N. de Ris, "Spread of a Laminar Diffusion Flame," in 12th Symposium (International) on Combustion, Combustion Institute, Pittsburgh, PA, USA, 1969, pp.241-252.
- [2] R.A Altenkirch, R. Eichhorn, and P.C. Shang, "Buoyancy Effects on Flames Spreading down Thermally Thin Fuels," *Combustion and Flame*, Vol. 37, No. 1, pp. 71-83, 1980.
- [3] L. Zhou, A.C. Fernandez-Pello, and R. Cheng, "Flame Spread in an Opposed Turbulent Flow," *Combustion and Flame*, Vol. 81, No. 1, pp.40-49, 1990.
- [4] I.S. Wichman, F.A. Williams, and I. Glassman, "Theoretical Aspects of Flame Spread in an Opposed Flow over Flat Surfaces of Solid Fuels," in 19th Symposium(International) on Combustion, Combustion Institute, Pittsburgh, PA, USA, 1982, pp.835-845.
- [5] I.S. Wichman, "Theory of Opposed-flow Flame Spread," *Progress in Energy and Combustion Science*, Vol. 18, No. 6, 1992, pp. 553-593.
- [6] S. Bhattacharjee, J. West, and R.A. Altenkirch, "Determination of the Spread Rate in Opposed-flow Flame Spread over Thick Solid Fuels in the Thermal Regime," in 26th Symposium(International) on Combustion, Combustion Institute, Pittsburgh, PA, USA, Vol. 1, 1996, pp. 1477-1485.
- [7] S. Bhattacharjee, M. King, S. Takahashi, T. Nagumo, and K. Wakai, "Downward Flame Spread over Poly(methyl) methacrylate," in 28th Symposium (International) on Combustion, Combustion Institute, Pittsburgh, PA, USA, Vol. 28, No. 2, 2000, pp. 2891-2897.
- [8] G.H. Markstein and J.N. de Ris, "Upward Fire Spread over Textiles," in 14th Symposium (International) on Combustion, Combustion Institute, Pittsburgh, PA, USA, 1972, pp. 1085-1097.
- [9] L. Orloff, J. de Ris, and G.H. Markstein, "Upward Turbulent Fire Spread and Burning of Fuel Surface," in 15th Symposium (International) on Combustion, Combustion Institute, Pittsburgh, PA, USA, 1974, pp.183-192.
- [10] A. Tewarson and S.D. Ogden, "Fire Behavior of Polymethylmethacrylate," *Combustion and Flame*, Vol. 89, No. 3 and 4, pp. 237-259, 1992.

- [11] J. Quintiere, M. Harkleroad, and Y. Hasemi, "Wall Flames and Implications for Upward Flame Spread," *Combustion Science and Technology*, Vol. 48, No. 3 and 4, pp. 191-222, 1985.
- [12] P.K. Wu, L. Orloff, and A. Tewarson, "Assessment of Material Flammability with the FSG Propagation Model and Laboratory Test Methods," in 13th Joint Panel Meeting of the UJNR Panel on Fire Research and Safety, NIST, Gaithersburg, MD, USA, 1996.
- [13] K. McGrattan and G. Forney, "FDS V.4 Technical Reference Guide," NIST Special Publication 1018, National Institute Standards and Technology, Gaithersburg, MD, 2005.
- [14] D. Madrzykowski and W.D. Walton, "Cook County Administration Building Fire, 69 West Washington, Chicago, Illinois, October 17, 2003: Heat Release Rate Experiments and FDS Simulations," NIST Special Publication SP-1021, National Institute Standards and Technology, Gaithersburg, MD, USA, 2004.
- [15] W. Grosshandler et al, "Report of the Technical Investigation of the Station Night Club Fire," NIST NCSTAR 2: Vol. 1, National Institute Standards and Technology, Gaithersburg, MD, USA, 2005.
- [16] S.S. Sunder et al., "Final Report of the National Construction Safety Team on the Collapses of the World Trade Center Towers (Draft)," NIST NCSTAR 1, National Institute Standards and Technology, Gaithersburg, MD, USA, 2005.
- [17] S. Hostikka and K.B. McGrattan, "Large Eddy Simulation of Wood Combustion," *International Interflam Conference 9th Proceedings*, Vol.1, Edinburgh, Scotland, Interscience, London, U.K., 2001, pp. 755-762.
- [18] J. Carlsson, "Computational Strategies in Flame-Spread Modeling Involving Wooden Surfaces-An Evaluation Study," Report 1028, Lund University, Sweden, 2003.
- [19] A.Z. Moghaddam, I.R. Moiduddin, I.R. Thomas, I.D. Bennetts, and M. Culton, "Fire Behavior Studies of Combustible Wall Linings Applying Fire Dynamics Simulator," in 15th Australian Fluid Mechanics Conference, the University of Sydney, Sydney, Australia, 2004.

- [20] M. Liang and J.G. Quintiere, "Evaluation Studies of the Flame Spread and Burning Rate Predictions by the Fire Dynamics Simulator," MS Thesis, University of Maryland, 2002.
- [21] J. Smagorinsky, "General Circulation Experiments with the Primitive Equations. I. The Basic Experiment," *Monthly Weather Review*, Vol. 91, No.3, pp. 99-164, 1963.
- [22] N. Peters, *Turbulent Combustion*, Cambridge University Press, Cambridge, U.K., 2002.
- [23] T. Ma, and J.G. Quintiere, "Numerical Simulation of Axi-symmetric Fire Plumes: Accuracy and Limitations," MS Thesis, University of Maryland, 2001.
- [24] Kevin McGrattan, Jason Floyd, Glenn Forney, and Howard Baum, "Development of Combustion and Radiation Models for Large Scale Fire Simulation," in *Proceedings of the Third Technical Symposium on Computer Applications in Fire Protection Engineering*, Bethesda, MD, 2001, pp. 14-22.
- [25] W. Grosshandler, "RADCAL: Narrow Band Model for Radiation Calculations Model in a Combustion Environment," NIST Technical Note 1402, Gaithersburg, MD, USA, 1993.
- [26] J. Kwon, "Evaluation of FDS V.4: Upward Flame Spread," M.S. Thesis, Worcester Polytechnic Institute, 2006.
- [27] P. Friday and F.W. Mowrer, "Comparison of FDS Model Predictions with FM/SNL Fire Test Data," NIST GCR 01-810, National Institute of Standards and Technology, Gaithersburg, MD, USA, 2001.
- [28] K.B. McGrattan, J.E. Floyd, G.P. Forney, H.R. Baum, and S. Hostikka, "Improved Radiation and Combustion Routines for a Large Eddy Simulation Fire Model," in *Fire Safety Science, Proceedings of the Seventh International Symposium*, International Association for Fire Safety Science, WPI, MA, USA, 2002, pp 827-838.
- [29] A. Bounagui, A. Kashef, and N. Benichou, "Simulation of the Fire for a Section of the L.H.- La Fortaine Tunnel," IRC-RR- 140, National Research Council Canada, Ontario, Canada, 2003.

- [30] K.B. McGrattan, H.R. Baum, R.G. Rehm, "Large Eddy Simulations of Smoke Movement", *Fire Safety Journal*, V.30, No.2, 1998, pp.161-178.
- [31] Tewarson, A., "Chapter 3-4, Generation of Heat and Chemical Compounds in Fires," in *The SFPE Handbook of Fire Protection Engineering*, 3rd edition, NFPA, Quincy, MA, 2002.
- [32] S. Lee "Material Property Method using a Thermoplastic Pyrolysis Model," MS Thesis, Worcester Polytechnic Institute, 2005.
- [33] P. Beaulieu, "Flammability Characteristics at Applied Heat Flux Levels up to 200 kW/m² and the Effect of Oxygen on Flame Heat Flux," Ph.D Dissertation, Worcester Polytechnic Institute, 2005.
- [34] D. Hopkins and J. Quintiere, "Material Fire Properties and Predictions for Thermoplastics," *Fire Safety Journal*, Vol. 26, No. 3, pp. 241-268, 1996.
- [35] C.H. Bamford, J. Crank, and D.H. Malan, "On the Combustion of Wood. Part I." *Proceedings of the Cambridge Phil. Soc.*, Vol.42, 1946, pp.166-182.
- [36] A. Tewarson, "Experimental Evaluation of Flammability Parameters of Polymeric Materials" in *Flame Retardant Polymeric Materials*, Vol. 3, pp. 97-153, Plenum Press, New York, 1982.
- [37] D. Deepak and D.D. Drysdale, "Flammability of Solids: An Apparatus to Measure the Critical Mass Flux at the Firepoint," *Fire Safety Journal*, Vol. 5, No.2, pp.167-169, 1983.
- [38] D.D. Drysdale and H.E. Thomson, "Flammability of Plastics II: Critical Mass Flux at the Firepoint," *Fire Safety Journal*, Vol. 14, No. 3, 1989, pp. 179-188.
- [39] J.G. Quintiere, "Chapter 2-12, Surface Flame Spread," in *The SFPE Handbook of Fire Protection Engineering*, 3rd edition, NFPA, Quincy, MA, 2002.
- [40] K. Saito, J.G. Quintiere, and F.A. Williams, "Upward Turbulent Flame Spread," in *Proceedings of the 1st International Symposium on Fire Safety Science*, NIST, MD, USA, 1985, pp. 75-86.

Future Work

FDS shows promise for simulating flame spread. The upward flame spread across a PMMA panel is observed, and the HRRs in the PMMA panel simulation and an FMRC experiment are of the same order of magnitude. However, the FDS predictions for flame spread do not show the trends of the experimental data. Several considerations are suggested to improve the capability of FDS for flame spread.

- FDS needs improvement of the combustion model and pyrolysis model coupling.
- A pyrolysis model in FDS V.4 as a continuous function of surface temperature forms flames to an unreasonable extent. Inclusion of a “switch” such as ignition temperature in the pyrolysis model can be considered to reproduce the experimental data as can be seen in Liang’s work.
- A different set of material properties can be considered. A high activation energy and a high pre-exponential factor in the pyrolysis model in FDS V.4 would act as a “switch” and make it possible to reproduce the experimental data.

Appendix A Theoretical Descriptions for FDS

Hydrodynamic model, combustion model, and thermal radiation model used in FDS are presented in this section.

A1 Hydrodynamic Model

Conservation of mass, conservation of momentum, and the divergence of velocity (obtained from conservation of energy) are presented below [1,2].

$$\frac{D\rho}{Dt} + \rho(\nabla \cdot \mathbf{u}) = 0 \quad (\text{A. 1})$$

$$\rho \frac{D\mathbf{u}}{Dt} = \rho \mathbf{g} + \nabla \cdot \Pi_{ij} \quad (\text{A. 2})$$

$$\nabla \cdot \mathbf{u} = \frac{1}{\rho C_p T} (\nabla \cdot k \nabla T - \nabla \cdot \dot{q}_r'' + \dot{q}''') + \left(\frac{1}{\rho C_p T} - \frac{1}{p_0} \right) \frac{dp_0}{dt} \quad (\text{A. 3})$$

The operator ∇ denotes the gradient, and $\nabla \cdot (\bullet)$ stands for the divergence. The following equation is the substantial derivative, or material derivative, which represents the time rate of change of quantity (\bullet) when moving with the fluid.

$$\frac{D(\bullet)}{Dt} = \frac{\partial(\bullet)}{\partial t} + \mathbf{u} \cdot \nabla(\bullet) \quad (\text{A. 4})$$

In momentum equation [A.2], the left hand side is the acceleration of a fluid. The first term on the right hand side represents the body force per unit volume. The second term on the right hand side is the surface forces per unit volume. These forces including normal forces and tangential (shear) forces are derived from the external stresses on the fluid. The stresses consisting of normal stresses and shearing stresses are represented by the component of the stress tensor Π_{ij} . If the fluid is assumed to be a Newtonian fluid, the stress tensor may be written as:

$$\Pi_{ij} = -p\delta_{ij} + \tau_{ij} \quad (\text{A. 5})$$

where δ_{ij} is the Kronecker delta function ($\delta_{ij} = 1$ if $i = j$ and $\delta_{ij} = 0$ if $i \neq j$) and τ_{ij} is the viscous stress tensor as follows:

$$\tau_{ij} = \mu \left[\left(\frac{\partial u_i}{\partial x_j} + \frac{\partial u_j}{\partial x_i} \right) - \frac{2}{3} \delta_{ij} \frac{\partial u_k}{\partial x_k} \right] \quad i, j, k = 1, 2, 3 \quad (\text{A. 6})$$

It is noted that the energy equation is not explicitly solved in FDS; however, it is employed to draw the expression of the divergence of velocity as presented in (A.3). Gas temperatures are obtained using the perfect gas law:

$$p_0 = \frac{\rho RT}{M_{mix}} \quad (\text{A. 7})$$

where R is the universal gas constant and M_{mix} is the molecular weight of the mixture of gases. The molecular weight of the mixture of gases is obtained by:

$$M_{mix} = \left(\sum_{i=1}^n \frac{Y_i}{M_i} \right)^{-1} \quad [\text{A. 8}]$$

where Y_i is the mass fraction of species i .

It is noted that the spatially averaged “background pressure” P_0 filtering out acoustic waves replaces the total pressure P in Eqn. A.3 and A.7. The total pressure can be expressed as follows:

$$P = P_0 + \Delta p \quad (\text{A. 9})$$

Δp is the pressure variation including hydrostatic and flow-induced perturbation:

$$\Delta p = \Delta p_{hydro} + \tilde{p} \quad (\text{A. 10})$$

As long as the height of domain is not order of km and the low Mach number assumption is used, Δp is negligible in comparison with P_0 . Therefore, a following relationship can be obtained:

$$P \approx P_0 \quad (\text{A. 11})$$

A2 Combustion Model

A2.1 Mixture Fraction Combustion Model

In non-premixed combustion, diffusion is the rate-limiting process. Generally, the diffusive and convective time needed is much greater than the time for combustion reactions to occur. It makes possible to assume that the chemical reaction is infinitely fast. This assumption is able to eliminate all

parameters related to finite-rate chemical kinetics from the analysis. From this assumption, the “conserved scalar” parameter, “mixture fraction”, is introduced [3]. The mixture fraction Z satisfies the balance equation:

$$\rho \frac{DZ}{Dt} = \nabla \cdot (\rho D \nabla Z) \quad (\text{A. 12})$$

$$\left. \begin{array}{l} Z = 0 \text{ in the oxidizer stream} \\ Z = 1 \text{ in the fuel stream} \end{array} \right\}$$

A two feed system is introduced to express the mixture fraction for homogeneous system or inhomogeneous system assuming equal diffusivities of species and inert substances. Subscript 1 and subscript 2 represent the fuel stream and the oxidizer stream, respectively. \dot{m} denotes a mass flux. Then, the mixture fraction Z is defined as follows:

$$Z = \frac{\dot{m}_1}{\dot{m}_1 + \dot{m}_2} \quad (\text{A. 13})$$

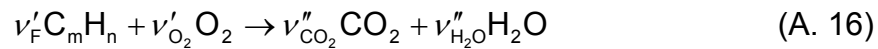
And then, the local mass fraction of fuel $Y_{F,u}$ and the local mass fraction of the oxidizer $Y_{O_2,u}$ in the unburnt mixture are associated with the mixture fraction Z :

$$Y_{F,u} = Y_{F,1} Z \quad (\text{A. 14})$$

$$Y_{O_2,u} = Y_{O_2,2} (1 - Z) \quad (\text{A. 15})$$

where $Y_{F,1}$ and $Y_{O_2,2}$ indicate the mass fraction of fuel in fuel stream and the mass fraction of the oxidizer in the oxidizer stream.

From now on, take the chemical reaction into account. A reaction equation for complete combustion of an arbitrary hydrocarbon fuel as:



Before combustion takes place, the mass fraction of fuel and oxygen are obtained as:

$$Y_F = \frac{\nu'_F M_F}{\nu'_F M_F + \nu'_{O_2} M_{O_2}} \quad (\text{A. 17})$$

$$Y_{O_2} = \frac{\nu'_{O_2} M_{O_2}}{\nu'_F M_F + \nu'_{O_2} M_{O_2}} \quad (\text{A. 18})$$

Combining Eqn. A.17 with A.18, the following equation is obtained:

$$Y_{O_2} = Y_F \frac{v'_{O_2} M_{O_2}}{v'_F M_F} \quad (\text{A. 19})$$

$\frac{v'_{O_2} M_{O_2}}{v'_F M_F}$ is the stoichiometric oxygen to fuel mass ratio s . Then, Eqn. A.19 can

be rewritten as:

$$Y_{O_2} = sY_F \quad (\text{A. 20})$$

For the case that the combustion is taking place, Eqn. A.20 can be expressed as follows:

$$dY_{O_2} = s dY_F \quad (\text{A. 21})$$

Integrating Eqn. A.21 between the unburnt and any other state of combustion for homogeneous system or inhomogeneous system having the equal diffusivities of fuel and oxidizer,

$$sY_F^P - Y_{O_2}^P = sY_{F,u} - Y_{O_2,u} \quad (\text{A. 22})$$

The mass fractions Y_i and $Y_{i,u}$ correspond to any other state of combustion and unburnt state. Associating Eqn. A.14 and A.15 with A.22, the expression of the mixture fraction Z in terms of the mass fractions of fuel and oxidizer is as:

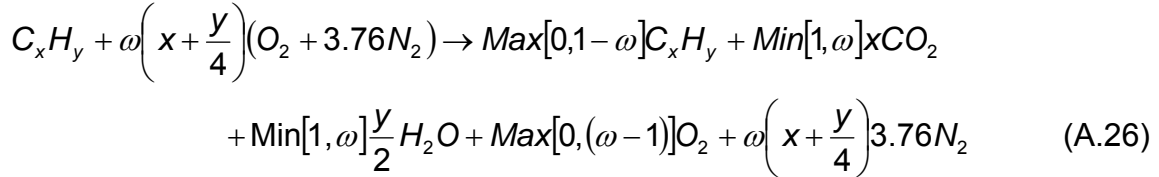
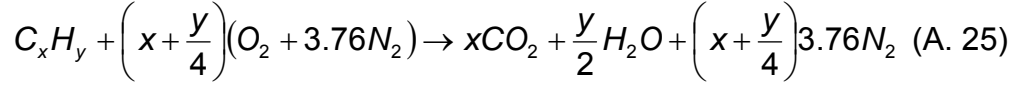
$$Z = \frac{sY_F^P - Y_{O_2}^P + Y_{O_2,2}}{sY_{F,1} + Y_{O_2,2}} \quad (\text{A. 23})$$

Note that the mixture fraction in the computational domain shows a post-combustion value (products). With a mixture fraction combustion model, the fuel and oxidizer cannot co-exist. The Y_F and Y_{O_2} are simultaneously zero where the flame sheet is formed. Thus, the flame surface, or the “iso-surface” of the stoichiometric mixture fraction is determined from:

$$Z_{st} = \frac{Y_{O_2,2}}{sY_{F,1} + Y_{O_2,2}} \quad (\text{A. 24})$$

A2.2 State Relations

Consider arbitrary hydrocarbon fuel combustions for the stoichiometric reaction and the non-stoichiometric reaction [1,4]:



The values of parameter ω of zero and infinity correspond to the mixture fraction of 1 and zero, respectively.

The mass fraction for each species can be expressed with regards to the mixture fraction, Z (See Figure A 1). These correlations are called as “state relations”. The relationships for fuel and oxidizer are as follows:

$$Y_F = \frac{Z - Z_{st}}{1 - Z_{st}}, \quad Y_{O_2} = 0, \quad \text{for } Z \geq Z_{st} \quad (\text{A. 27a})$$

$$Y_{O_2} = Y_{O_2,2} \left(1 - \frac{Z}{Z_{st}}\right), \quad Y_F = 0, \quad \text{for } Z \leq Z_{st} \quad (\text{A. 25b})$$

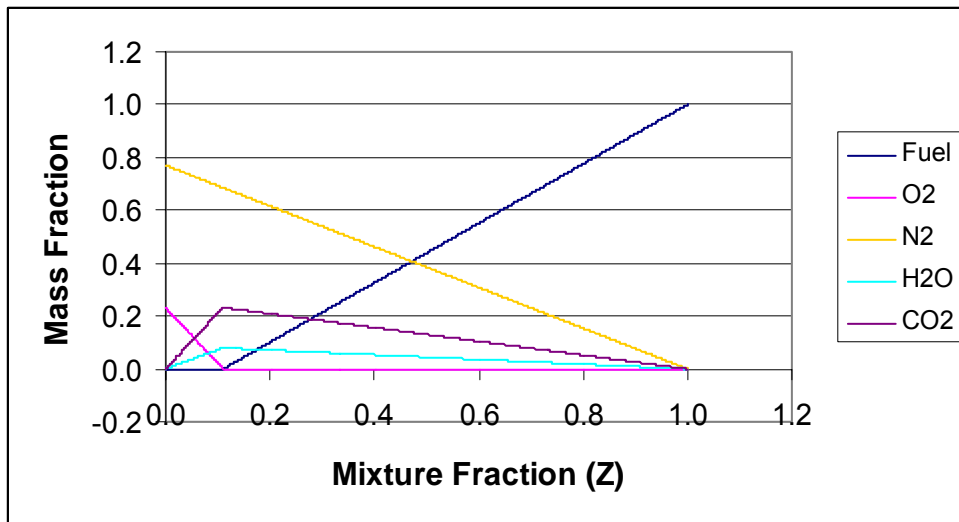


Figure A 1 MMA State Relations

A2.3 Heat Release Rate Calculation in FDS

In FDS, a calculation of heat release rate is based on the amount of depleted oxygen [5]:

$$\dot{q}''' = \Delta H_o \dot{m}'''_{O_2} \quad (\text{A. 28})$$

where ΔH_o is the amount of heat release per unit mass of oxygen consumed. A nearly constant value of heat of 13.1 MJ/kg(O₂) is released for most organic materials. For expression for a local oxygen consumption rate, consider the conservation equation for mixture fraction (Eqn. A.12) and the state relation for oxygen $Y_o(Z)$ [1,4]:

$$\rho \frac{DY_{O_2}}{Dt} = \nabla \cdot (\rho D \nabla Y_{O_2}) + \dot{m}'''_{O_2} \quad (\text{A. 29})$$

where D is the turbulent diffusion coefficient and \dot{m}'''_{O_2} is oxygen consumption during combustion. Multiply Eqn. A.12 by $\frac{dY_{O_2}}{dZ}$:

$$\rho \frac{dY_{O_2}}{dZ} \frac{DZ}{Dt} = \frac{dY_{O_2}}{dZ} \nabla \cdot (\rho D \nabla Z) \quad (\text{A. 30})$$

As the chain rule is applied, the following expression can be obtained from Eqn. A.29:

$$\rho \frac{dY_{O_2}}{dZ} \frac{DZ}{Dt} = \nabla \cdot \left(\rho D \frac{dY_{O_2}}{dZ} \nabla Z \right) + \dot{m}'''_{O_2} \quad (\text{A. 31})$$

Subtract [A.31] from [A.30]:

$$-\dot{m}'''_{O_2} = \nabla \cdot \left(\rho D \frac{dY_{O_2}}{dZ} \nabla Z \right) - \frac{dY_{O_2}}{dZ} \nabla \cdot (\rho D \nabla Z) \quad (\text{A. 32})$$

It is difficult for Eqn. A.32 to be incorporated into the numerical scheme. The volume expression can be converted into the surface expression (flame sheet) by applying the divergence theorem. This leads to:

$$-\dot{m}'''_{O_2} = \frac{dY_{O_2}}{dZ} \rho D \nabla Z \cdot \vec{n} \Big|_{Z=Z_f} \quad (\text{A. 33})$$

There is a numerical advantage in Eqn. A.33 because it just has a single first order, space derivative.

A3 Thermal Radiation Model

A3.1 Radiative Transport Equation (RTE)

The Radiative Transport Equation (RTE) addresses the radiation intensity along a path through a medium. The intensity obtained from the RTE presents the local radiation traveling in a single direction per unit solid angle and wavelength. The intensity at any position along the path is changed by absorption, emission, and scattering as radiation passes through the layer [6]:

$$\frac{di'_\lambda}{dS} = -a_\lambda i'_\lambda(S) + a_\lambda i'_{\lambda b}(S) - \sigma_{s\lambda} i'_\lambda(S) + \frac{\sigma_{s\lambda}}{4\pi} \int_{\omega_i=4\pi} i'_\lambda(S, \omega_i) \Phi(\lambda, \omega, \omega_i) d\omega_i \quad (\text{A. 34})$$

$i, S, \lambda, \omega, a, \sigma_s, \Phi$, subscript b , subscript λ , and subscript i denote the radiation intensity, the coordinate along path of radiation, the wavelength, the solid angle, the absorption coefficient, the scattering coefficient, the phase function for scattering, the blackbody, the spectrally dependent, and the incident, respectively. The left hand side of Eqn. A.34 is the change in intensity with S in the solid angle $d\omega$ about the direction of S . The first term in the right hand side of Eqn. A.40 represents a loss by absorption. The second term is a gain by emission. The third and last term indicate a loss by scattering and a gain by scattering into S direction, respectively. If the non-scattering medium is considered for the RTE, Eqn. A.34 is reduced as:

$$\frac{di'_\lambda}{dS} = -a_\lambda i'_\lambda(S) + a_\lambda i'_{\lambda b}(S) = a_\lambda (i'_{\lambda b}(S) - i'_\lambda(S)) \quad (\text{A. 35})$$

A3.2 Thermal Radiation Model in FDS

The radiation spectrum is divided into a number of bands since the spectral dependence cannot be calculated accurately in the practical simulation. Then, Eqn. A.35 can be expressed as [1,7]:

$$\frac{di'_n}{dS} = a_n (i'_{nb}(S) - i'_n(S)) \quad n = 1, 2, \dots, N \quad (\text{A. 36})$$

Soot that is inevitably generated from most fire cases dominates the thermal radiation from fire and hot gas layer. For all but lightly sooting fuels, it is possible to treat the gas as gray medium (independent of wavelength) since soot has a

continuous radiation spectrum and can be considered a non-scattering material. Thus, the mean absorption coefficient ($n=1$) can be reasonably used. The RTE for non-scattering gray gas evolved from Eqn. A.36 can be expressed as:

$$\frac{di'}{dS} = a (i'_b(S) - i'(S)) \quad (\text{A. 37})$$

The source term is given by blackbody radiation intensity:

$$i'_b = \frac{\sigma}{\pi} T^4 \quad (\text{A. 38})$$

where σ is the Stefan-Boltzman constant. The use of mean absorption coefficient (a) results in reducing the amount of computation considerably since the values of a can be tabulated a function of variables such as gas temperature and mixture fraction (gas compositions). a is pre-calculated in FDS by employing RADCAL [8].

A3.3 Radiation Inside Flame Zone

As described in Eqn A38, the radiative source term i'_b depends on the temperature raised to the fourth power. Therefore, inaccurate computation of temperature results in large error in the radiative source term. Especially, temperatures inside the flame zone are under-estimated if the spatial resolution used is not fine enough to resolve the flame since the flame sheet occupies only a small fraction of the cell volume. To compensate for this limitation, FDS provides two options for the calculation of the source term inside the flame zone:

$$a \cdot i' = \text{Max} \left(\frac{\chi_{rad} \cdot \dot{q}'''}{4\pi}, \frac{a\sigma T^4}{\pi} \right) \quad (\text{Inside flame zone}) \quad (\text{A. 39})$$

where χ_{rad} is the user specified radiative fraction value. The method employing HRRPUV and radiative fraction value is usually dominant as fire grows. Unlike inside flame zone, it is believed that the estimation of temperature outside the flame zone is reliable. Therefore, the radiative source term is determined only from:

$$a \cdot i' = \frac{a\sigma T^4}{\pi} \quad (\text{Outside flame zone}) \quad (\text{A. 40})$$

A4 Appendix A References

- [1] K. McGrattan and G. Forney, "FDS V.4 Technical Reference Guide," NIST Special Publication 1018, National Institute Standards and Technology, Gaithersburg, MD, 2005.
- [2] H.R. Baum, K.B. McGrattan, and R.G. Rehm, "Three Dimensional Simulations of Fire Plume Dynamics," in Fire Safety Science, Proceedings of the Fifth International Symposium, International Association for Fire Safety Science, Melbourne, Australia, 1997, pp 511-522.
- [3] N. Peters, Turbulent Combustion, Cambridge University Press, Cambridge, U.K., 2002.
- [4] J.E. Floyd, H.R. Baum, and K.B. McGrattan, "A MIXTURE FRACTION COMBUSTION MODEL FOR FIRE SIMULATION USING CFD," in Proceedings of the International Conference on Engineered Fire Protection Design, San Francisco, CA. 2001, pp. 279-290.
- [5] C. Huggett, "Estimation of the Rate of Heat Release by Means of Oxygen Consumption" Fire and Materials, Vol. 12, 1980, pp. 61-65.
- [6] R. Siegel and J.R. Howell, Thermal Radiation Heat Transfer, 4th ed., Taylor and Francis, New York, 2002.
- [7] Kevin McGrattan, Jason Floyd, Glenn Forney, and Howard Baum, "Development of Combustion and Radiation Models for Large Scale Fire Simulation," in Proceedings of the Third Technical Symposium on Computer Applications in Fire Protection Engineering, Bethesda, MD, 2001, pp. 14-22.
- [8] Grosshandler, W. RADCAL: Narrow Band Model for Radiation Calculations Model in a Combustion Environment. NIST technical note 1402, 1993.

Appendix B Grid Resolution Analysis

Grid size plays an important role in FDS to capture the features of flow and combustion. FDS shows sensitivity to grid size in many applications [1,2,3,4,5]. A smaller grid size is preferred for better simulation of both large and small scale dynamics; however, a larger grid size is favored in terms of a computational cost. The FDS predictions are compared to the Steckler's experimental data [6] to determine the optimum resolution.

B1 Grid Resolution Criteria and Test Matrix

According to Ma [1], the optimum resolution is determined as 5 % of plume characteristic length, D^* :

$$D^* = \left[\frac{\dot{Q}}{\rho_\infty c_\infty T_\infty \sqrt{g}} \right]^{2/5} \quad [\text{B. 1}]$$

where \dot{Q} , ρ_∞ , c_∞ , T_∞ , and g are respectively total heat release rate (kW), density at ambient temperature (kg/m^3), specific heat of gas ($\text{kJ/kg}\cdot\text{K}$), ambient temperature (K), and gravity acceleration (m/s^2). If the grid size is greater than 5 % of D^* , flame height tends to be underestimated compared to a calculated flame height. Below 5%, flame height tends to be overestimated.

Also, McGrattan [7] suggested 10% of plume characteristic length as adequate resolution after careful comparisons with plume correlations.

Based on these suggestions, the four simulations are conducted to obtain the "best" grid size for the applications to be examined later. A test matrix for a grid resolution analysis is presented in Table B 1. When the coarse grids are used, fire is not adequately resolved. This leads to underestimate a heat release rate and flame height [1]. One way to remedy these drawbacks is to redefine the stoichiometric value of mixture fraction. Therefore, a routine is implemented into FDS with a following relation to enhance the mixture fraction combustion model:

$$\frac{Z_{st,eff}}{Z_{st}} = \min\left(1, C \frac{D^*}{d\delta}\right) \quad [B. 2]$$

Z_{st} and $Z_{st,eff}$ are respectively the ideal stoichiometric value of mixture fraction and the redefined stoichiometric value of mixture fraction. C is an empirical constant of 0.6 and $d\delta$ is grid spacing. D^* is the plume characteristic length. As either the grid resolution is finer or the fire size increases, the $Z_{st,eff}$ would approach the ideal stoichiometric value of mixture fraction. In other words, once the value in the last column in Table B 1 is greater than one, the ideal stoichiometric value of mixture fraction is used by Eqn. B.2.

The investigation begins with 10% of plume characteristic length. Then, the grid spacing is halved and doubled. The grid sensitivity analysis by Bounagui [29] showed the maximum plume temperature was improved by decreasing the grid spacing in the z-direction. Thus, the non-uniform grid size (CASE 4) is, also, examined. 5% of D^* is not investigated due to the high computational expense. Halving the grid size in all three dimensions would theoretically increase the total computation time by about a factor of 16. As the numbers of grid are doubled in each direction, so as are the numbers of time steps for fixed Courant numbers because the maximum allowable timestep is decreased. Interestingly, greater than 16-fold increases in the computation time is observed when decreasing the grid size by half. This is, also, observed by Friday and Mowrer [27]. The results from the four cases are presented later.

Table B 1 Test Matrix for Grid Resolution Analysis

CASE	Grid Size(m)			Total Cells	Computation Time(hour)	Real Time(sec)	D*	C(D*) /max(d δ)
	dx	dy	dz					
1	0.03	0.03	0.03	622080	93	500	0.31	5.8
2	0.06	0.06	0.06	77760	5	500	0.31	3.15
3	0.09	0.09	0.09	23040	0.7	500	0.31	2.1
4	0.05	0.05	0.02	373324	74	500	0.31	3.78

B2 Description of Steckler's Experiment

Steckler, et al [6] conducted fifty five full-scale experiments representing different fire strengths (31.6, 62.9, 105.3, and 158 kW), the sizes of opening, fire locations. The experiment compartment was 2.4 m x 2.4 m x 2.14 m in dimension. Movable bi-directional velocity probes and bare-wire thermocouples within the room opening measured the velocities and temperatures of the opening. A fixed vertical array of aspirated thermocouples in the front corner of the room measured the compartment gas temperature profile. Another array of bare-wire thermocouples were placed in the larger well vented area outside the room to measure the near ambient temperature profile. For the comparison with the FDS predictions, one of the experiments is chosen, which has 62.9 kW fire, 0.74 m x 1.83 m door opening, and fire located in the center of the compartment (Figure B 1).

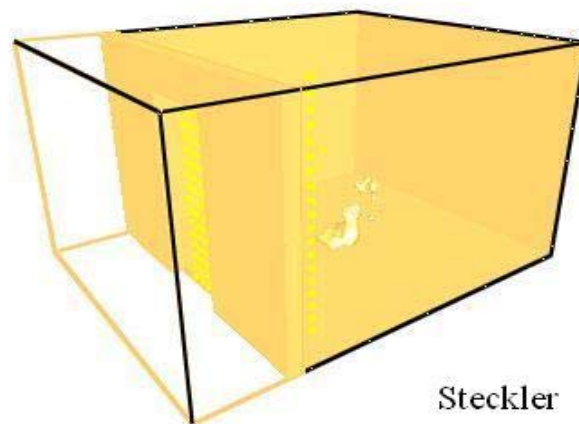


Figure B 1 Snapshot of Steckler's Experiment' FDS Simulation

B3 Comparison FDS Predictions with Experimental Data

Figure B 2, Figure B 3, and Figure B 4 present the comparison of room gas temperatures, doorway temperatures, and doorway velocities, respectively. From these figures, CASE1 used the finest grids, shows the best comparison

with the experimental data. It is noted that finer grids are not guaranteed to provide better prediction from the comparison between CASE 2 and CASE 3. CASE4, or non-uniform grids, did not produce the better results. Therefore, the “10 % criterion” would be used for the rest of works.

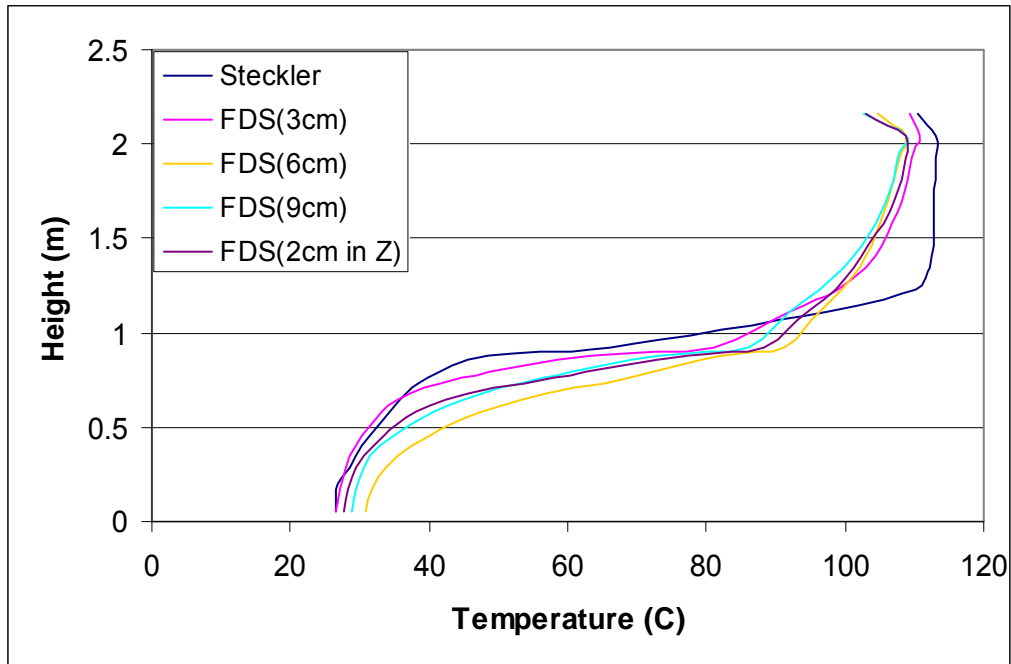


Figure B 2 Room Temperature Profile Comparison in Grid Sensitivity Analysis

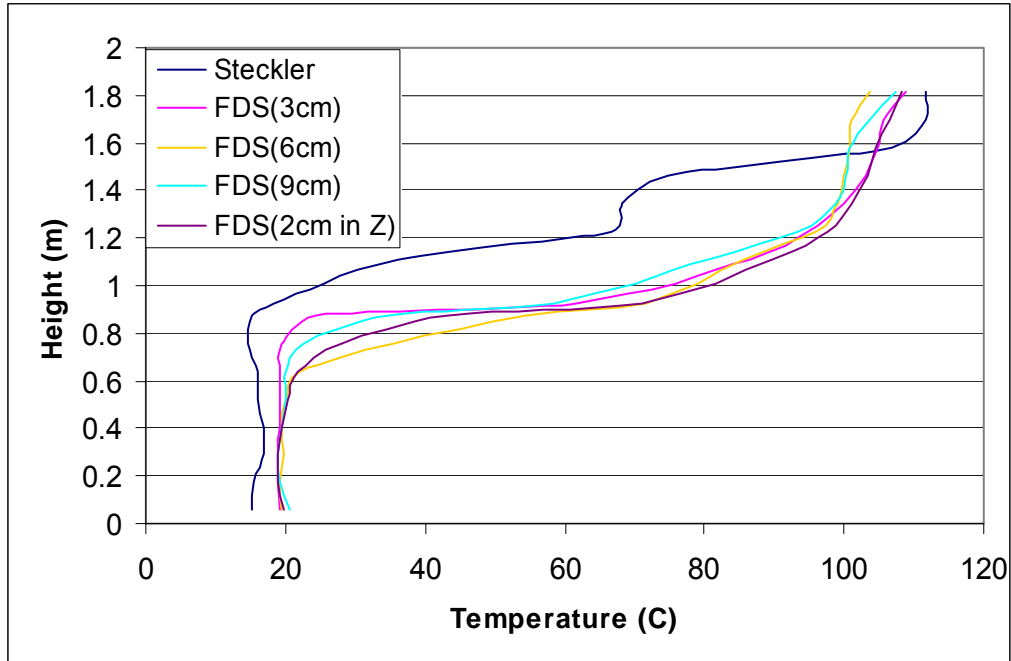


Figure B 3 Doorway Temperature Profile Comparison in Grid Sensitivity Analysis

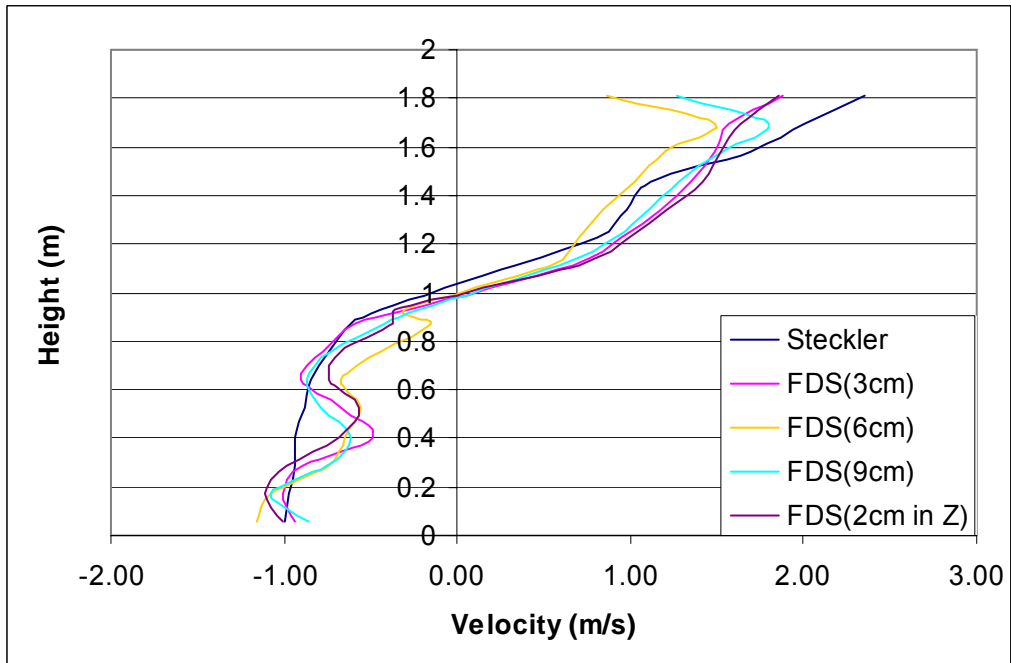


Figure B 4 Doorway Velocity Profile Comparison in Grid Sensitivity Analysis

B4 Summary

Before the gas-phase sensitivity analysis is conducted, the criterion for grid size should be set because 1) the FDS outputs are sensitive to the grid size and 2) the input parameters such as Smagorinsky constant appears to have the interaction with grid refinement (Eqn. C1). The plume characteristic length, D^* , is served as a cue to determine the appropriate grid size. The “best” grid size is determined by comparing the Steckler’s experimental data to the FDS predictions. CASE1 used the finest grids shows the best comparison with the experimental data. Therefore, “10 % criterion” would be used for the rest of works. It is noted that finer grids are not guaranteed to provide better prediction.

B5 Appendix B References

- [1] T. Ma, and J.G. Quintiere, “Numerical Simulation of Axi-symmetric Fire Plumes: Accuracy and Limitations,” MS Thesis, University of Maryland, 2001.
- [2] P. Friday and F.W. Mowrer, “Comparison of FDS Model Predictions with FM/SNL Fire Test Data,” NIST GCR 01-810, National Institute of Standards and Technology, Gaithersburg, MD, USA, 2001.
- [3] K.B. McGrattan, J.E. Floyd, G.P. Forney, H.R. Baum, and S. Hostikka. “Improved Radiation and Combustion Routines for a Large Eddy Simulation Fire Model,” in Fire Safety Science, Proceedings of the Seventh International Symposium, International Association for Fire Safety Science, WPI, MA, USA, 2002, pp 827-838.
- [4] A. Bounagui, A. Kashef, and N. Benichou, “Simulation of the Fire for a Section of the L.H.- La Fortaine Tunnel,” IRC-RR- 140, National Research Council Canada, Ontario, Canada, 2003.
- [5] W. Grosshandler et al, “Report of the Technical Investigation of the Station Night Club Fire,” NIST NCSTAR 2: Vol. 1, National Institute Standards and Technology, Gaithersburg, MD, USA, 2005.

[6] K.D. Steckler, J.G. Quintiere, and W.J. Rinkinen, "Flow Induced by Fire in a Compartment," NISIR 82-2520, National Bureau of Standards National Engineering Laboratory Center for Fire Research, Washington D.C, MD, USA, 1982.

[7] K.B. McGrattan, H.R. Baum, R.G. Rehm, "Large Eddy Simulations of Smoke Movement", Fire Safety Journal, V.30, No.2, 1998, pp.161-178.

Appendix C Gaseous Phase Sensitivity Analysis

To properly evaluate FDS for use in simulation of fire spread scenarios a baseline gas phase uncertainty of FDS is determined. This uncertainty is based on a sensitivity analysis of key input parameters and their subsequent effect on key output variables that are important for fire spread. The gaseous phase input variables considered are: Smagorinsky constant ranging from 0.1 to 0.25, Prandtl number from 0.2 to 0.9, Schmidt number from 0.2 to 1.0, angle increment down to 1, time increment to 1, the number of radiation angles up to 150, and radiative fraction. The variation of these inputs is justified on a common sense physical basis from values determined from the literature. The output variables are: surface heat fluxes, plume/room temperatures, plume/room velocities, and flame heights. These outputs are related to the heat transfer for fire spread on a nearby combustible objects. This baseline uncertainty is determined using actual scenarios that involve gas burner fires. Both “small” and “large” compartment fires have been considered: the Steckler’s room experiment (Appendix B) for “small” fire simulation and the propane characterization experiment (Appendix D) for “large” fire simulation. The baseline uncertainty has been developed from 2 fire scenarios and 42 FDS simulations (Figure C 1). Where it exists, experimental data has been included as a check on the reasonableness of output variations.

Run ID	Referend	Grid Resolution			Qd	Reaction	Xr	CSMAG	Pr	Sc	Radiation Angle	Angle Increment	Time Step Automatic Increment	Step Automatic Z	Baroclinic	VBC	Yes
		i (cm)	j (cm)	k (cm)													
1	Steckler	3	3	3	0.32	Methane	0.15	0.2	0.50	0.50	100	5	3	TRUE	FALSE	0.50	0.010
2	Steckler	3	3	3	0.32	Methane	0.15	0.2	0.50	0.50	100	5	3	TRUE	TRUE	0.50	0.010
3	Propane	4	4	4	0.38-0.95	Propane	0.35	0.2	0.50	0.50	100	5	3	TRUE	TRUE	0.50	0.010
4	Steckler	3	3	3	0.32	Methane	0.15	0.1	0.50	0.50	100	5	3	TRUE	FALSE	0.50	0.010
5	Steckler	3	3	3	0.32	Methane	0.15	0.14	0.50	0.50	100	5	3	TRUE	FALSE	0.50	0.010
6	Steckler	3	3	3	0.32	Methane	0.15	0.18	0.50	0.50	100	5	3	TRUE	FALSE	0.50	0.010
7	Steckler	3	3	3	0.32	Methane	0.15	0.25	0.50	0.50	100	5	3	TRUE	FALSE	0.50	0.010
8	Propane	4	4	4	0.38-0.95	Propane	0.35	0.1	0.50	0.50	100	5	3	TRUE	FALSE	0.50	0.010
9	Propane	4	4	4	0.38-0.95	Propane	0.35	0.25	0.50	0.50	100	5	3	TRUE	FALSE	0.50	0.010
10	Steckler	3	3	3	0.32	Methane	0.15	0.2	0.20	0.50	100	5	3	TRUE	FALSE	0.50	0.010
11	Steckler	3	3	3	0.32	Methane	0.15	0.2	0.90	0.50	100	5	3	TRUE	FALSE	0.50	0.010
12	Propane	4	4	4	0.38-0.95	Propane	0.35	0.2	0.20	0.50	100	5	3	TRUE	FALSE	0.50	0.010
13	Propane	4	4	4	0.38-0.95	Propane	0.35	0.2	0.90	0.50	100	5	3	TRUE	FALSE	0.50	0.010
14	Cox	4	4	4	0.33	Methane	0.15	0.2	0.50	0.50	100	5	3	TRUE	FALSE	0.50	0.010
15	Cox	4	4	4	0.33	Methane	0.15	0.2	0.50	0.20	100	5	3	TRUE	FALSE	0.50	0.010
16	Cox	4	4	4	0.33	Methane	0.15	0.2	0.50	1.00	100	5	3	TRUE	FALSE	0.50	0.010
17	Cox	4	4	4	0.37	Methane	0.15	0.2	0.50	0.50	100	5	3	TRUE	FALSE	0.50	0.010
18	Cox	4	4	4	0.37	Methane	0.15	0.2	0.50	0.20	100	5	3	TRUE	FALSE	0.50	0.010
19	Cox	4	4	4	0.37	Methane	0.15	0.2	0.50	1.00	100	5	3	TRUE	FALSE	0.50	0.010
20	Cox	4	4	4	0.4	Methane	0.15	0.2	0.50	0.50	100	5	3	TRUE	FALSE	0.50	0.010
21	Cox	4	4	4	0.4	Methane	0.15	0.2	0.50	0.20	100	5	3	TRUE	FALSE	0.50	0.010
22	Cox	4	4	4	0.4	Methane	0.15	0.2	0.50	1.00	100	5	3	TRUE	FALSE	0.50	0.010
23	Cox	4	4	4	0.4	Methane	0	0.2	0.50	0.50	100	5	3	TRUE	FALSE	0.50	0.010
24	Cox	4	4	4	0.72	Methane	0.15	0.2	0.50	0.50	100	5	3	TRUE	FALSE	0.50	0.010
25	Cox	4	4	4	0.72	Methane	0.15	0.2	0.50	0.20	100	5	3	TRUE	FALSE	0.50	0.010
26	Cox	4	4	4	0.72	Methane	0.15	0.2	0.50	1.00	100	5	3	TRUE	FALSE	0.50	0.010
27	Cox	4	4	4	0.72	Methane	0.15	0.2	0.50	0.50	100	5	3	TRUE	FALSE	0.50	0.024
28	Propane	4	4	4	0.38-0.95	Propane	0.35	0.2	0.50	0.50	100	5	3	TRUE	FALSE	0.50	0.010
29	Propane	4	4	4	0.38-0.95	Propane	0.35	0.2	0.50	0.50	100	3	3	TRUE	FALSE	0.50	0.010
30	Propane	4	4	4	0.38-0.95	Propane	0.35	0.2	0.50	0.50	100	1	3	TRUE	FALSE	0.50	0.010
31	Propane	4	4	4	0.38-0.95	Propane	0.35	0.2	0.50	0.50	100	5	1	TRUE	FALSE	0.50	0.010
32	Propane	4	4	4	0.38-0.95	Propane	0.35	0.2	0.50	0.50	125	5	3	TRUE	FALSE	0.50	0.010
33	Propane	4	4	4	0.38-0.95	Propane	0.35	0.2	0.50	0.50	150	5	3	TRUE	FALSE	0.50	0.010
34	Propane	4	4	4	0.38-0.95	Propane	0	0.2	0.50	0.50	100	5	3	TRUE	FALSE	0.50	0.010
35	Albert	4	4	4	0.38	Methane	0.15	0.2	0.50	0.50	100	5	3	TRUE	FALSE	0.50	0.010
36	Albert	4	4	4	0.38	Methane	0.15	0.2	0.50	0.50	100	5	3	TRUE	FALSE	-1.00	0.010
37	Albert	4	4	4	0.38	Methane	0.15	0.2	0.50	0.50	100	5	3	TRUE	FALSE	0.00	0.010
38	Albert	4	4	4	0.38	Methane	0.15	0.2	0.50	0.50	100	5	3	TRUE	FALSE	1.00	0.010
39	Albert	4	4	4	0.66	Methane	0.15	0.2	0.50	0.50	100	5	3	TRUE	FALSE	0.50	0.010
40	Albert	4	4	4	0.66	Methane	0.15	0.2	0.50	0.50	100	5	3	TRUE	FALSE	-1.00	0.010
41	Albert	4	4	4	0.66	Methane	0.15	0.2	0.50	0.50	100	5	3	TRUE	FALSE	0.00	0.010
42	Albert	4	4	4	0.66	Methane	0.15	0.2	0.50	0.50	100	5	3	TRUE	FALSE	1.00	0.010

Figure C 1 FDS Simulation Matrix for Gaseous Phase Sensitivity Analysis.

C1 Parameters in the MISC Namelist Group (CSMAG, PR, and SC)

Setting global parameters are conducted in the MISC line in FDS. MISC represents the namelist group of miscellaneous input parameters. As discussed in Appendix A, Large Eddy Simulation (LES) is to be performed for most applications before the sufficient speed and storage capacity of computer that is able to handle Direct Numerical Simulation (DNS) for practical configurations comes out. The sensitivity of LES parameters (Smagorinsky constant, turbulent Schmidt number, and turbulent Prandtl number) are presented in the following section.

C1.1 Smagorinsky Coefficient (CSMAG) Sensitivity Analysis

C1.1.1 Descriptions of Smagorinsky Coefficient

In LES, large-scale eddies are computed directly while small-scale eddies are modeled. In FDS, the Smagorinsky sub-grid scale (SGS) model [1] is used to represent the unresolved eddy motion. The Smagorinsky SGS turbulent viscosity is modeled as [2]:

$$\mu_{LES} = \rho (C_{smag} \Delta)^2 \left(2 \overline{\mathbf{S}}_{ij} \cdot \overline{\mathbf{S}}_{ij} - \frac{2}{3} (\nabla \cdot \overline{\mathbf{u}})^2 \right)^{\frac{1}{2}} \quad (\text{C. 1})$$

where the term $(\overline{\mathbf{S}}_{ij})$ is the strain tensor, C_{smag} is the Smagorinsky constant, and Δ is the length of grid cell. The Smagorinsky model produces satisfactory results for most large-scale applications; however, it has some drawbacks as follows:

- The requirement of the Smagorinsky constant C_{smag} in Eqn. C.1 is flow dependent: C_{smag} of 0.1 is optimized for channel flow [3,4], 0.12 for the flow around bluff body [5], and ranging from 0.17 to 0.19 [6] and 0.23 [7] for isotropic turbulent flow.
- The poor turbulence modeling near a wall [8].
- No ability for sub-grid scale energy to backscatter to a resolved scale [9].

The FDS predictions with the variation of Smagorinsky coefficients are compared. The data from two experiments (Steckler's experiment and propane

characterization experiment) is used as a reference. The Smagorinsky constant is optimized ranging from 0.1 to 0.25 [5]. Here, the coefficients of 0.1, 0.14, 0.18, 0.2 (FDS default value), and 0.25 are tried for the sensitivity analysis.

C1.1.2 Results and Discussion

The comparisons using the Steckler's experiment are shown in Figure C 2 (room temperature profile), Figure C 3 (doorway temperature profile), and Figure C 4 (doorway velocity profile). As a value of the Smagorinsky constant increases, FDS predicts the higher upper layer temperatures that are closer to the experimental data (See Figure C 2 and Figure C 3). The velocities in a doorway are relatively insensitive to the Smagorinsky constants.

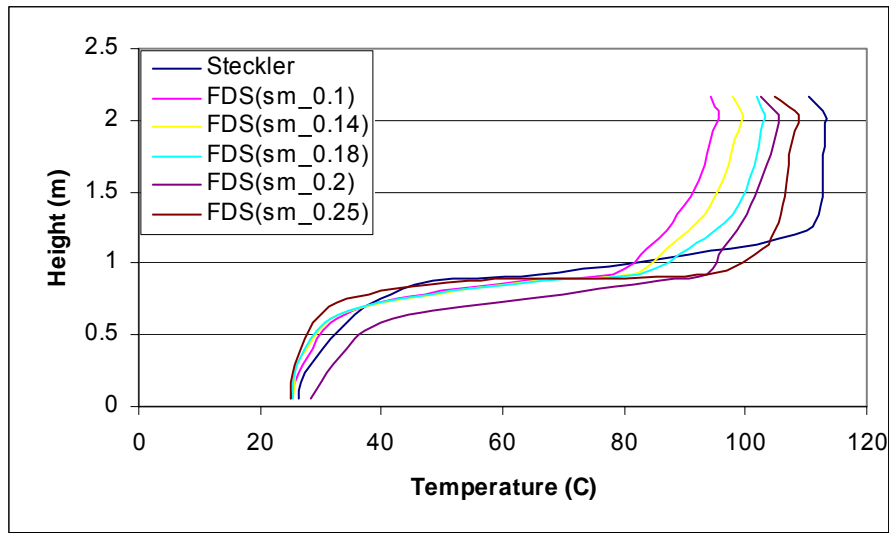


Figure C 2 Room Temperature Profile Comparison in Smagorinsky Constant Sensitivity.

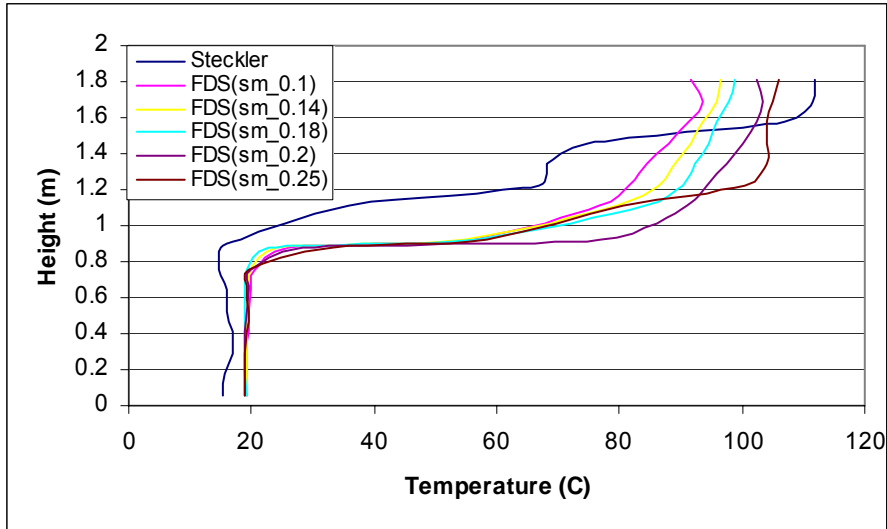


Figure C 3 Doorway Temperature Profile Comparison in Smagorinsky Constant Sensitivity.

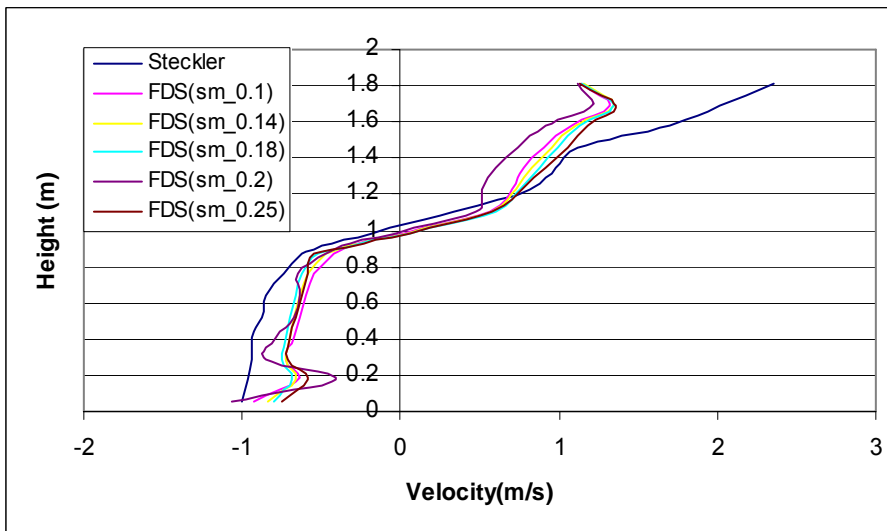


Figure C 4 Doorway Velocity Profile Comparison in Smagorinsky Constant Sensitivity.

Figure C 5, Figure C 6, and Figure C 7 represent the comparisons of incident heat fluxes, room temperature, and HRR involving the propane characterization experiment. Two methods, oxygen depletion and carbon dioxide generation, are used to calculate the HRR in the room. The details of experiment

and data reduction are presented in Appendix D. When a value of 0.1 is used, the followings are observed:

- Overshooting at the early time of simulation in incident heat flux at TSC 2.
- Larger errors in incident heat fluxes (38%), temperature (20%), and HRR than those in the relatively high Smagorinsky constant (within 10 %).

Based on these results, a relatively high value of Smagorinsky constant would be appropriate for most fire cases that have mostly a turbulent flow.

In Figure C 7, when a relatively low value of C_{smag} (=0.1) is used, the HRR is underestimated by about 5 % compared to a default value (0.2). As a value of Smagorinsky constant decreases, a turbulent viscosity decreases as can be seen in Eqn. C.1. Subsequently, this leads the mass diffusivity to lower:

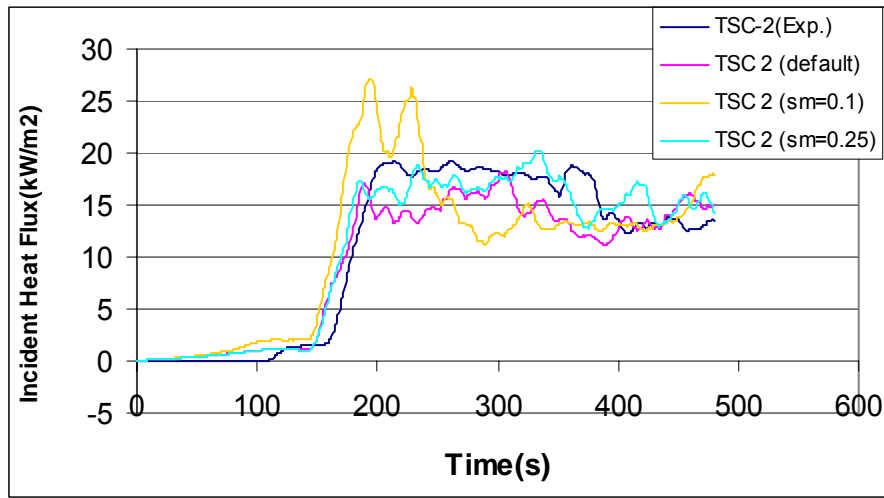
$$(\rho D)_{LES} = \frac{\mu_{LES}}{Sc} \quad (C. 2)$$

where Sc is the turbulence Schmidt number. As described in Eqn. A.33, the mass diffusivity term is involved in the calculation of HRR. Therefore, it can be expected that a heat release rate in FDS would vary by changing the Smagorinsky constant.

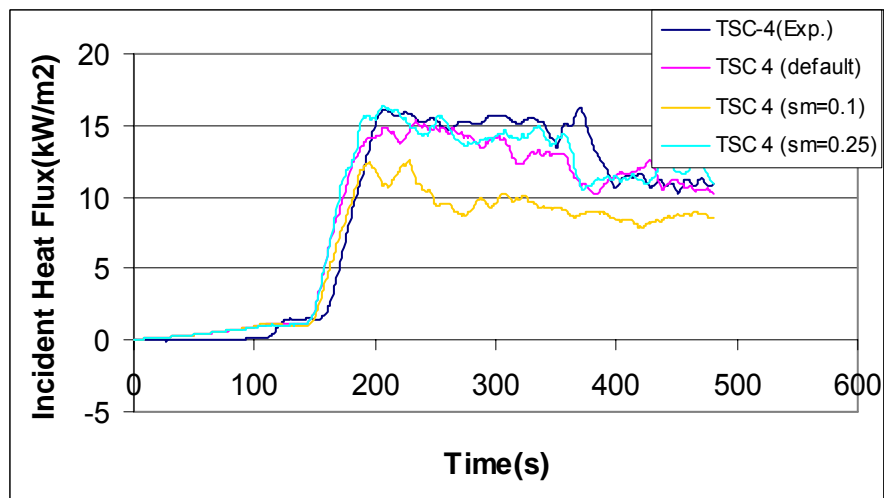
In nature, this might be explained with ‘flame stretch’. The flame front becomes more distorted and pockets of burning gas may break away and travel in the hot burnt gas stream at higher turbulence intensities before finally being consumed. This leads to a thicker reaction zone and slower burning. Eventually flame stretch may extend to the point where holes appear in the front. Cold gas is then able to enter the reaction zone and reduce the temperature and reaction rate until the flame is eventually extinguished [10].

The snapshots comparing the effects of variations of Smagorinsky constant are presented in Figure C 8 through Figure C 10. Figure C 8, Figure C 9, and Figure C 10 show respectively “Iso-surface” of HRRPUA, temperature 2D contour, and speed 2D contour in the middle of the burner at 210 second. As can be seen in Figure C 8 through Figure C 10, the flames are more influenced by entrained air when the low Smagorinsky constant is used. This results in the

rougher flame boundary and contours. The reason is considered that gas holds the low viscosity due to the low Smagorinsky constant.



(a)



(b)

Figure C 5 Incident Heat Flux Comparison at (a) TSC2 and (b) TSC4 in Smagorinsky Constant Sensitivity.

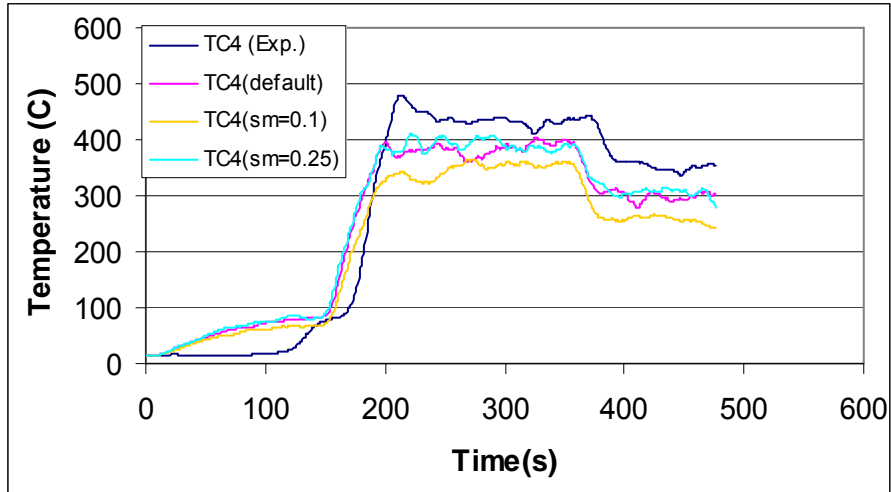


Figure C 6 Temperature Comparison (TC in Upper Layer) in Smagorinsky Constant Sensitivity.

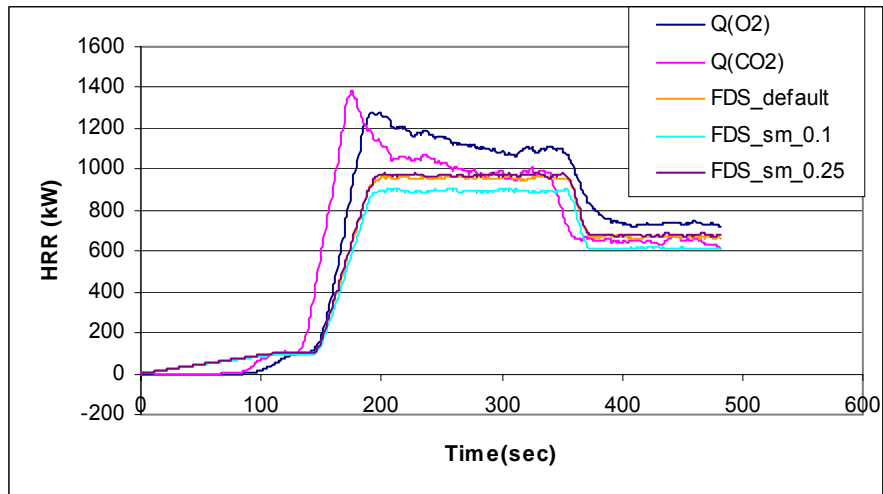


Figure C 7 Heat Release Rate Comparison in Smagorinsky Constant Sensitivity.

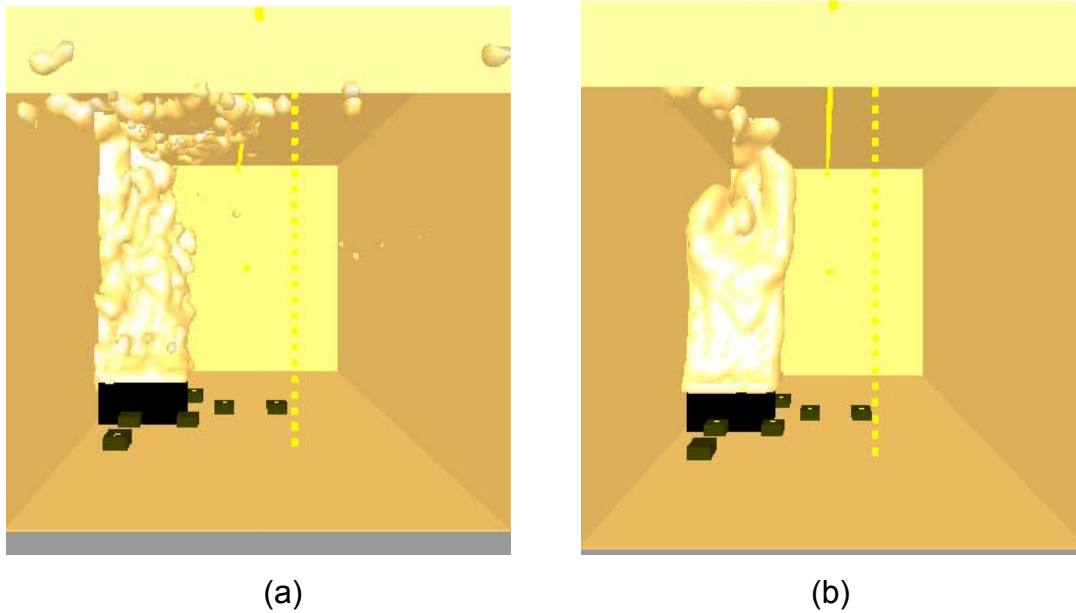


Figure C 8 Iso-surface File Snapshots of HRRPUA
 (a)CSMAG=0.1 (b)CSMAG=0.25 at 210 seconds
 in FDS Simulation of Propane Characterization Experiment.

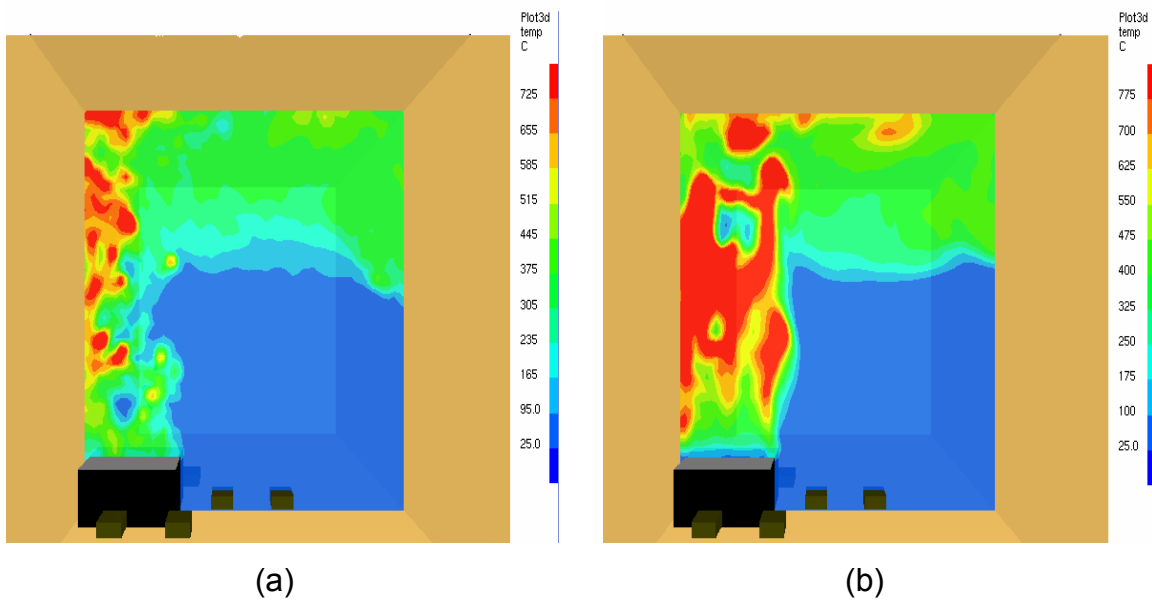
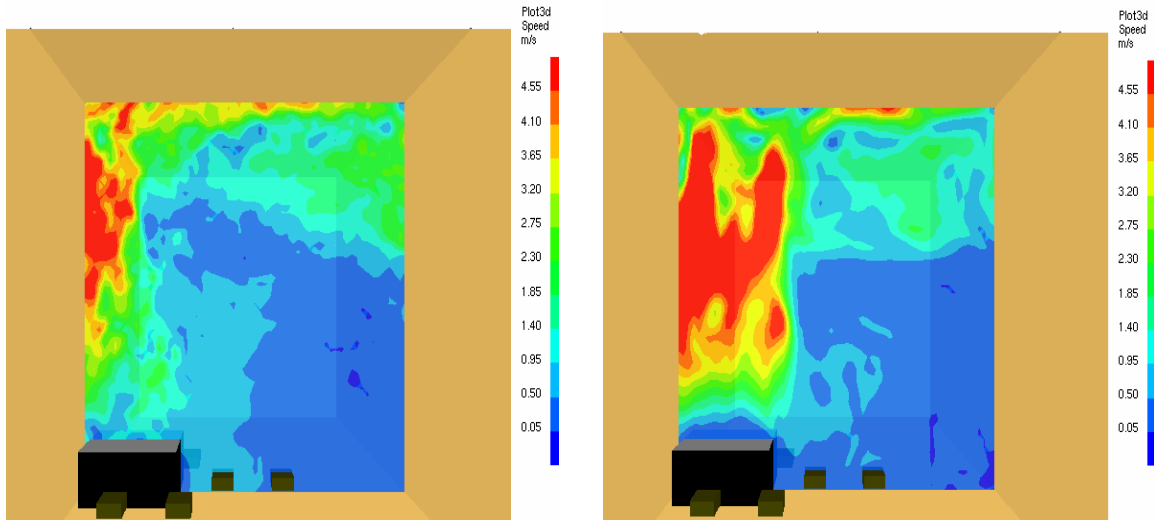


Figure C 9 PLOT 3D File Snapshots of Temperature ($^{\circ}\text{C}$),
 (a) CSMAG=0.1, (b)CSMAG=0.25, at 210 seconds
 in FDS Simulation of Propane Characterization Experiment.



(a) (b)

Figure C 10 PLOT 3D File Snapshots of Speed (m/s),
 (a) CSMAG=0.1, (b) CSMAG=0.25, at 210 seconds
 in FDS Simulation of Propane Characterization Experiment.

C1.1.3 Summary

A relatively high value of coefficient in the ranges of 0.1 to 0.25 is adequate for both “small” and “large fire cases (a turbulent flow). It is noted that the SGS model shows the weaknesses to predict the data in the near ceiling region. Although it is presumed that the default value (Cs=0.2) is applicable for most applications, it is worth to investigate to find more suitable model coefficient for each scenario. Note that Germano et al. [11] developed a dynamic sub-grid scale model where the Smagorinsky constant is adjusted to the local flow conditions.

C1.2 Turbulent Prandtl Number (PR) Sensitivity Analysis

C.1.2.1 Descriptions of Turbulent Prandtl Number Analysis

In LES, the thermal conductivity is calculated as [2]:

$$k_{LES} = \frac{\mu_{LES} C_P}{Pr} \quad (C. 3)$$

where C_p is the specific heat of gas, μ_{LES} is the viscosity of gas obtained from Eqn. C.1, and Pr is the turbulent Prandtl number. The Prandtl number, Pr, is considered as a constant in LES in FDS. The viscosity and thermal conductivity are presumed to have a universal character.

The Prandtl number is generally determined by empirical correlation ranging from 0.2 to 0.9 [9]. The value of 0.33 is optimized for an atmospheric boundary layer [12], and 0.5 for indoor airflow [5]. The Prandtl number of 0.58 was obtained from the turbulence statistical theory [13]. The FDS predictions with several Prandtl numbers are compared. The data from two experiments is used as a reference: (1) Steckler's Experiment and (2) Propane Characterization Experiment. The turbulent Prandtl numbers of 0.2, 0.5 and 0.9 are tried for the sensitivity analysis. The default value in FDS is 0.5.

C.1.2.2 Results and Discussion

The comparisons between the FDS predictions and the Steckler's experimental data are shown in Figure C 11 (room temperature profile), Figure C 12 (doorway temperature profile), and Figure C 13 (doorway velocity profile). The temperatures and velocities appear to be insensitive to the variation of Prandtl number (1-5 % difference). It is noted FDS predicts the higher upper layer temperatures (closer to the experimental data) as a value of the Prandtl number decreases. It is considered the enhanced thermal conductivity plays in a role.

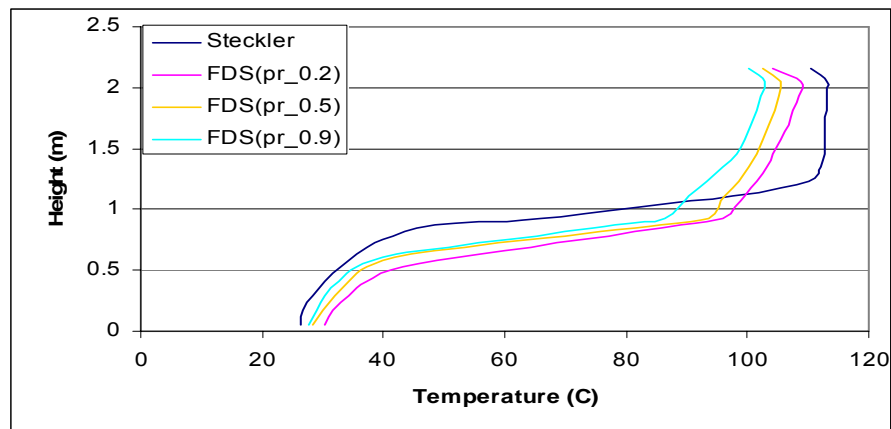


Figure C 11 Room Temperature Profile Comparison in Prandtl Number Sensitivity.

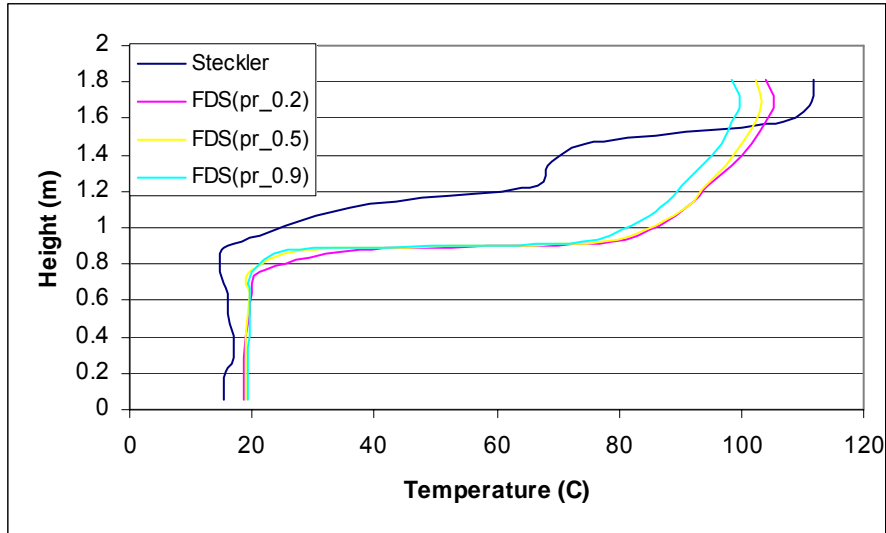


Figure C 12 Doorway Temperature Profile Comparison in Prandtl Number Sensitivity.

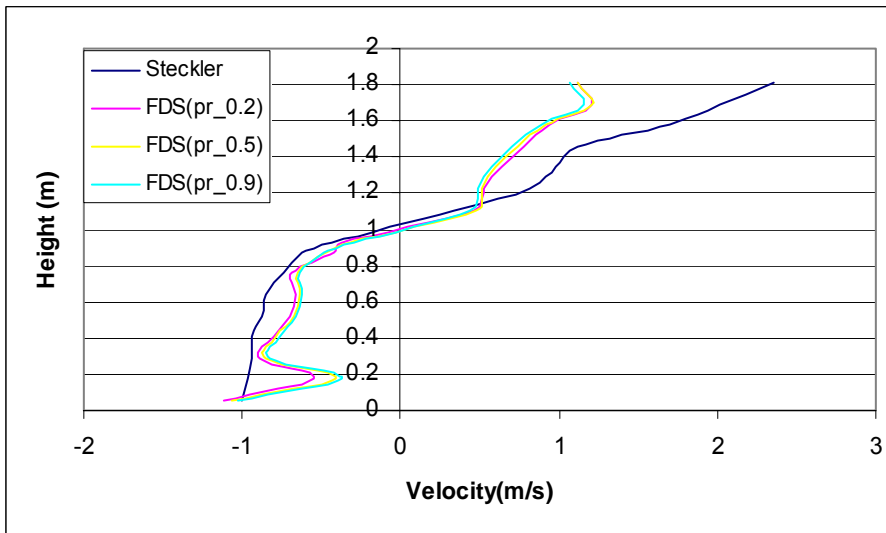
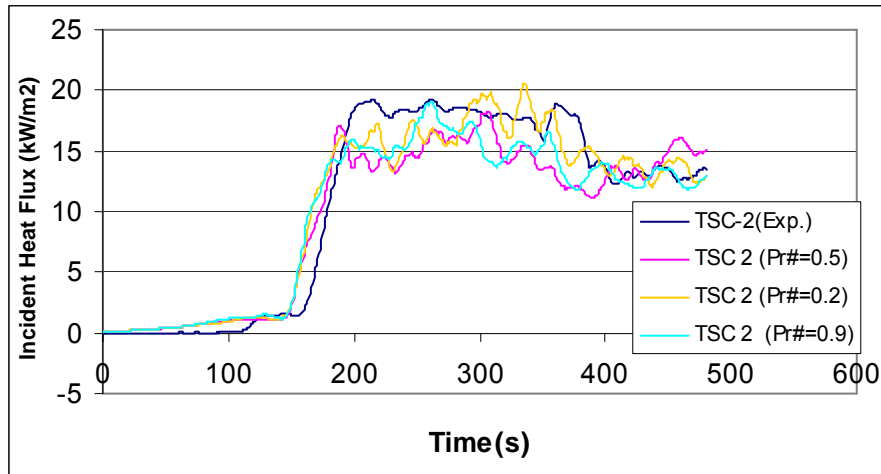


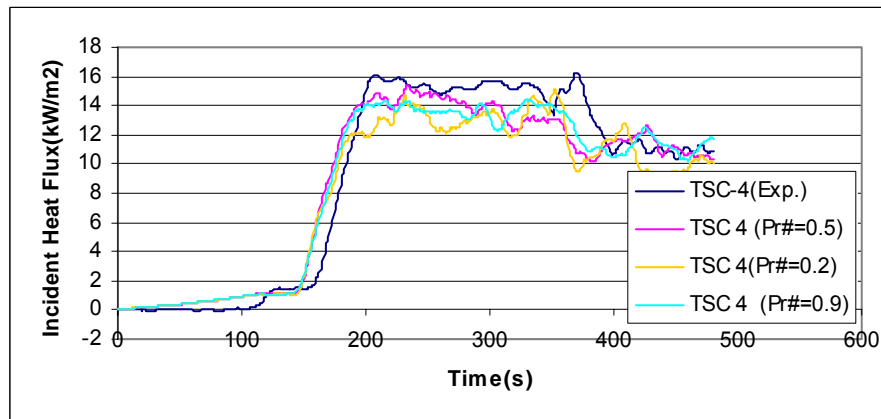
Figure C 13 Doorway Velocity Profile Comparison in Prandtl Number Sensitivity.

Figure C 14, Figure C 15, and Figure C 16 represent the comparisons of incident heat fluxes, room temperature in the upper layer, and room temperature in the lower layer involving the propane characterization experiment. As can be seen in the previous comparisons (Steckler’s experiment), the FDS predictions little change as the Prandtl number varies. The discrepancies between the

simulations for the incident heat fluxes are within 10 %. Generally, the FDS predictions using a default value ($Pr=0.5$) show a good agreement with the experimental data. It is noted the large discrepancy is observed in the lower layer temperature due to the radiation from hot layer to bare bead thermocouple in cold layer in the experiment.



(a)



(b)

Figure C 14 Incident Heat Flux Comparison at (a) TSC2 and (b) TSC4 in Prandtl Number Sensitivity.

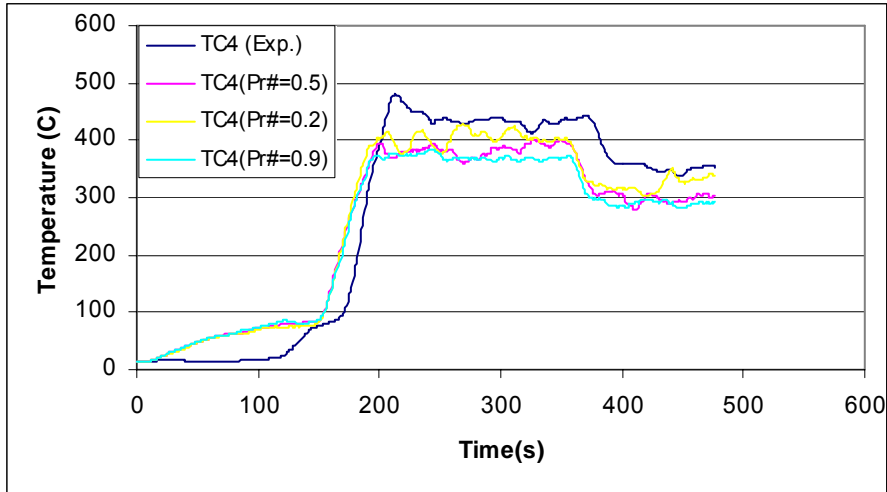


Figure C 15 Room Temperature Comparison (TC in Upper Layer) in Prandtl Number Sensitivity.

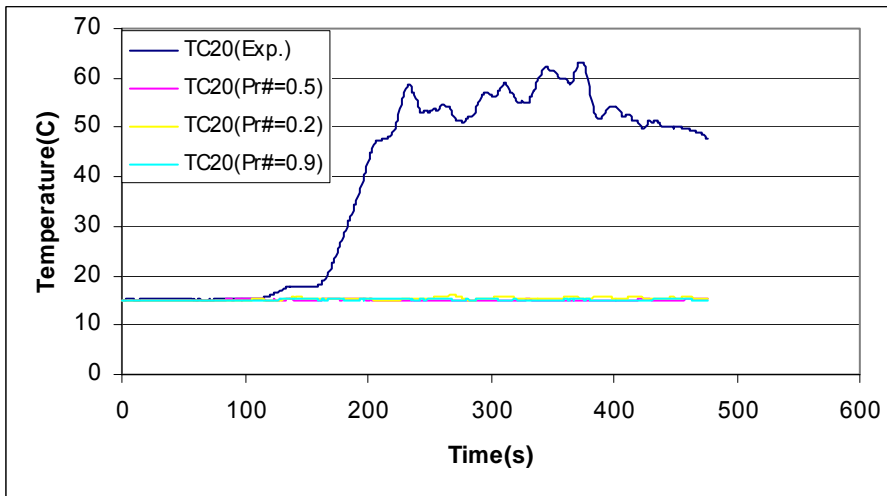


Figure C 16 Room Temperature Comparison (TC in Lower Layer) in Prandtl Number Sensitivity.

C1.2.3 Summary

The variations of the Prandtl number little effect on the output. The FDS predictions using a default value ($Pr=0.5$) show a good agreement with two experimental data. A large discrepancy in the temperature in the lower layer is caused mostly by the radiation effect in the experimental data.

C1.3 Turbulent Schmidt Number (SC) Sensitivity Analysis

C1.3.1 Descriptions of Turbulent Schmidt Number Analysis

In LES, the thermal conductivity is defined by [2]:

$$(\rho D_{LES}) = \frac{\mu_{LES}}{Sc} \quad (C. 4)$$

where D_{LES} is the mass diffusivity of gas, μ_{LES} is the viscosity obtained from Eqn. (C.1), and Sc is turbulent Schmidt number. The Schmidt number, Sc , is considered as a constant in LES in FDS. The viscosity and mass diffusivity are presumed to have a universal character. The Schmidt number of 0.2, 0.5, and 1.0 [14] are tried for the sensitivity analysis. The default value in FDS is 0.5.

An FDS domain was constructed as close as the experimental set up by Cox and Chitty [15]. A square burner was placed in the center of an open space (Figure C 17). The 500 kW fire is prescribed directly. The HRR, gas temperatures, and incident heat fluxes are obtained and are compared between the simulations. For the comparisons, the values of gas temperatures and incident heat fluxes are averaged for 45 seconds after a steady state is reached.

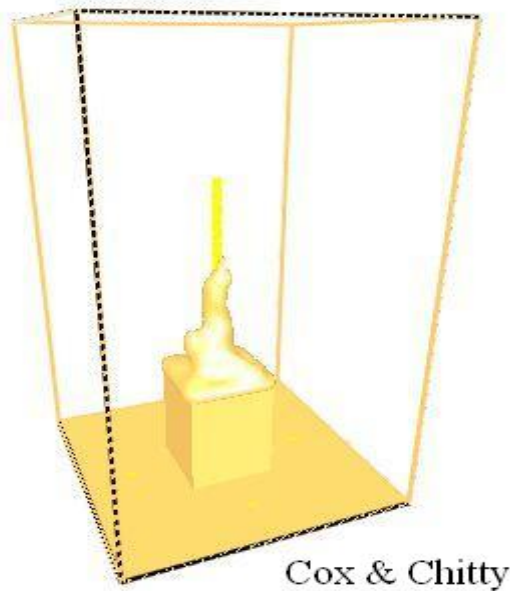


Figure C 17 Snapshot of FDS Simulation of Cox and Chitty's Experiment.

C1.3.2 Results and Discussion

The HRR comparison in the Schmidt number analysis is shown in Figure C 18. It is evident that the HRR in FDS is sensitive to the Schmidt number. As a value of the Schmidt number is decreased, the predicted HRR is closer to the prescribed one. In Eqn. C.4, a change in the Schmidt number results in a change in the mass diffusivity. Subsequently, it effects to the calculation of the HRR as shown in Eqn. A.33. The plots for the gas temperatures and incident heat fluxes between the simulations are not presented here, but the differences are within 10 %.

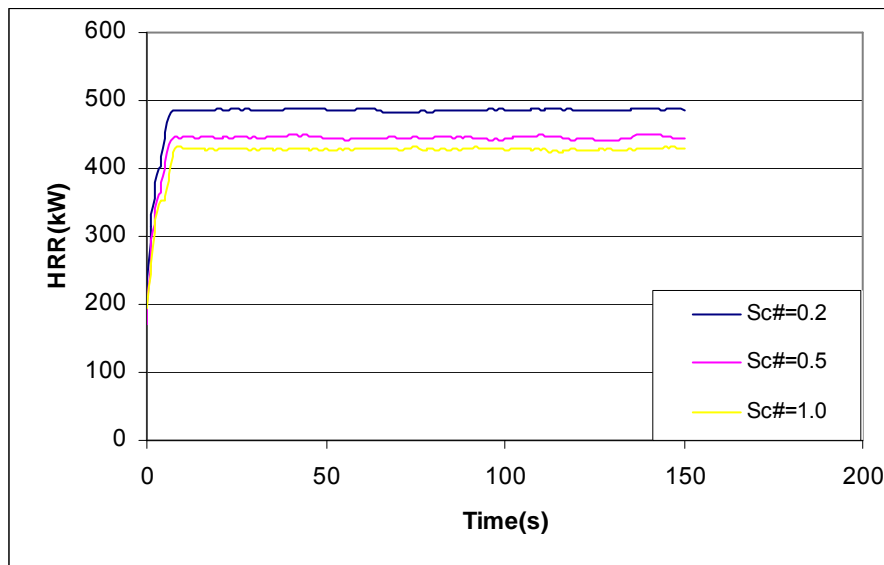


Figure C 18 HRR Comparison for Schmidt Number Analysis.

C1.3.3 Summary

Interestingly, the HRR output in FDS is varied by changing the Schmidt number. This seems because the mass diffusivity is included in the HRR calculation in FDS. A lower value of the Schmidt number produces closer to the prescribed HRR. The same results are observed when the 80 kW fire is used. Generally speaking, the default value of 0.5 is good to use. If one would like to get the same HRR output as input using a default value for Sc, it needs to be taken uncertainty into account.

C2 Parameters in the RADI Namelist Group (Angle Increment, Number Radiation Angles, and Time Increment)

Parameters affecting solution of the Radiation Transport Equation (RTE) can be modified in a namelist group called RADI. There are two models in the radiation solver [2]: a gray gas model and a wide band model. Here, only a gray gas model is considered because 1) the use of a wide band model is not practical due to the computational expenses 2) soot is considered as the dominant radiant emitter. The parameters of angle increment, number radiation angles, and time increment are investigated for the sensitivity analysis. It is noted in advance that the efforts to improve the radiation calculation result in a significant increase in the computational cost.

C2.1 Angle Increment Sensitivity Analysis

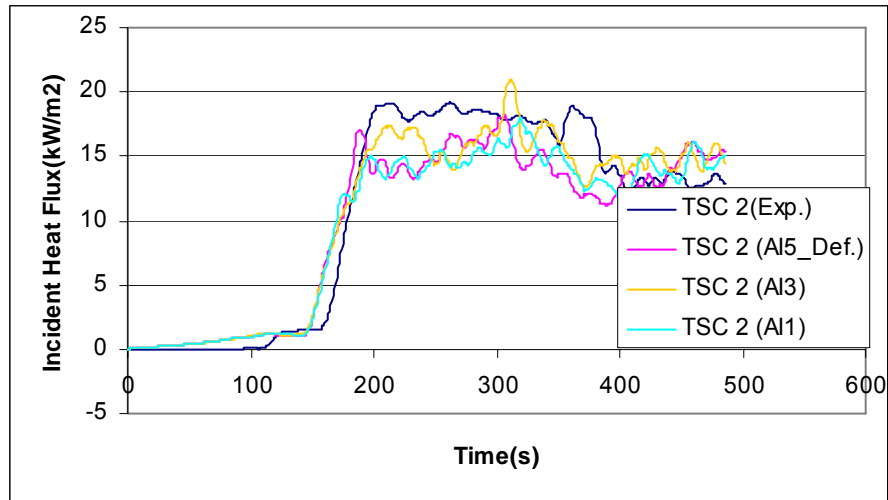
C2.1.1 Descriptions of Angle Increment Analysis

The parameter of angle increment is defined as the increment over which the angles updated. The default value for this parameter is five; in other words, 20 % of the radiation angles are updated once the radiation solver is called. The propane characterization experiment is used as a reference. The FDS domain is constructed as close as the experimental set-up. The angle increments of 3 and 1 are tried and investigated the subsequent effects. The configuration of personal computer used is 3.6 GHz with 1 GB RAM and the operating system is Windows XP.

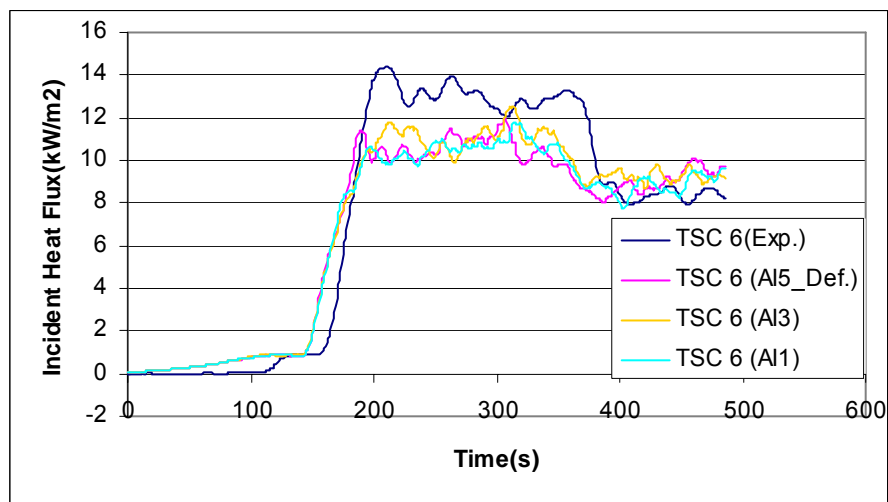
C2.1.2 Results and Discussion

Figure C 19, Figure C 20, and Figure C 21 represent the comparisons of incident heat fluxes, room temperature in the upper layer, and room temperature in the lower layer involving the propane characterization experiment. As can be seen from these charts, the FDS predictions change little as the angle increment is varied. The discrepancies in the incident heat fluxes and the temperatures between the simulations are within 5 % and 2%, respectively. The FDS predictions show a good agreement with the experimental data. Note that the

large discrepancy is observed in the temperature prediction in the lower layer due to the radiation from hot layer to bare bead thermocouple in cold layer in the experiment. It is worthy to note that the run time is increased by about 18% and 55 % from a default value case (=5) to 3 and to 1 (80.4 hr -> 95 hr -> 120.3 hr).



(a)



(b)

Figure C 19 Incident Heat Flux Comparison at (a) TSC2 and (b) TSC6 in Angle Increment Sensitivity.

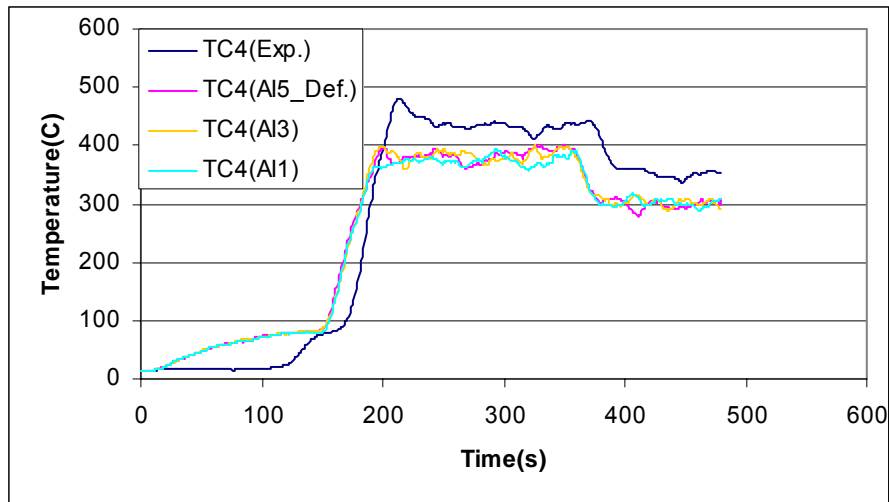


Figure C 20 Temperature Comparison (TC in Upper Layer) in Angle Increment Sensitivity.

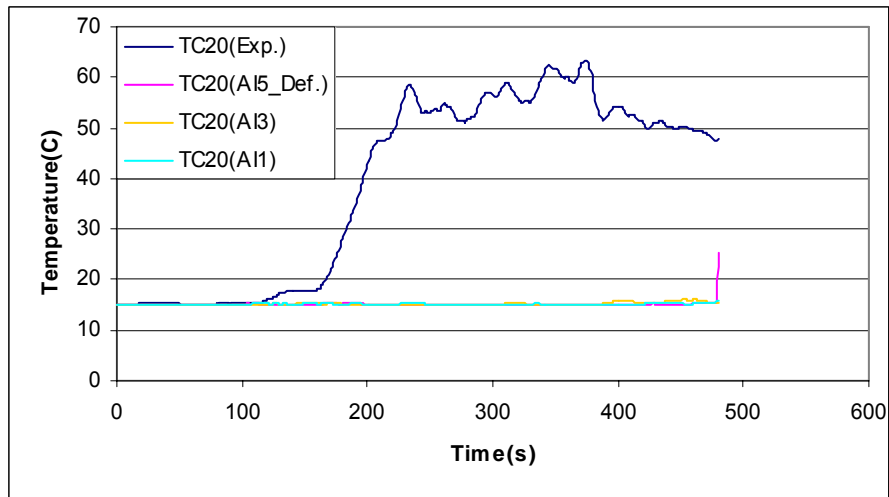


Figure C 21 Temperature Comparison (TC in Lower Layer) in Angle Increment Sensitivity.

C2.1.3 Summary

Several values for the angle increment parameter are tried to improve the radiation calculation in FDS. Its variations, however, little effect on the output. In general, the FDS predictions show a good agreement with the experimental data. A large discrepancy in the temperature in the lower layer is caused mostly by the

radiation effect in the experimental data. When the trade-off between the radiation calculation improvements and numerical costs is considered, a default value (=5) for angle increment is favored to use.

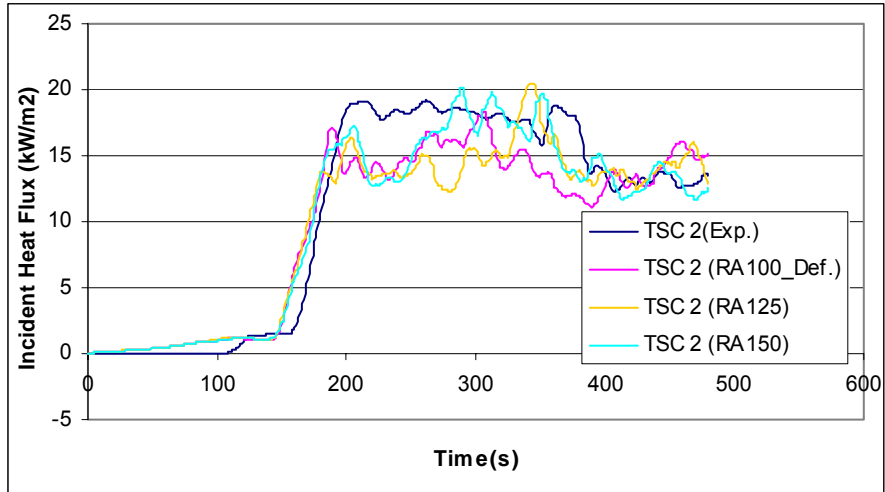
C2.2 Number Radiation Angles Sensitivity Analysis

C2.2.1 Descriptions of Number Radiation Angles Analysis

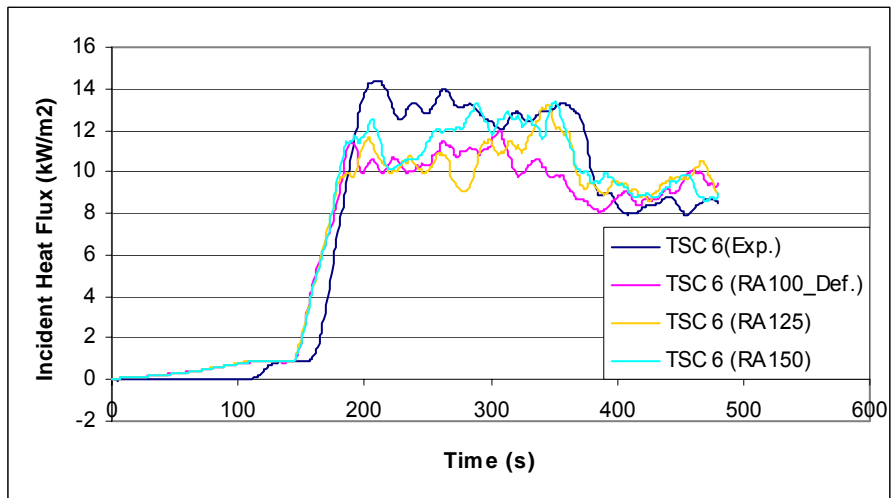
The parameter of number radiation angles is defined as the number of discrete angles for each cell for the radiation calculation. A default value for this parameter is one hundred. The propane characterization experiment is used as a reference. The FDS domain is constructed as close as the experimental set-up. The number of radiation angles is raised to 125 and to 150, and investigated the subsequent effects. The configuration of personal computer used is 3.6 GHz with 2 GB RAM and the operating system is Windows XP.

C2.2.2 Results and Discussion

Figure C 22, Figure C 23, and Figure C 24 represent the comparisons of incident heat fluxes, room temperature in the upper layer, and room temperature in the lower layer. As the number of radiation angles increase, the FDS predictions somewhat improve (10% for the incident heat fluxes and 5 % for the temperatures). Generally, the FDS predictions show a good agreement with the experimental data. It is noted a large discrepancy is observed in the temperature in the lower layer due to the radiation from hot layer to bare bead thermocouple in cold layer in the experiment. It is worthy to note that the run time is significantly increased by about 160% and 340 % from a default value case (=100) to 125 and to 150 (22.3 hr → 57.5 hr → 98.8 hr).



(a)



(b)

Figure C 22 Incident Heat Flux Comparison at (a) TSC2 and (b) TSC6 in Number Radiation Angles Sensitivity.

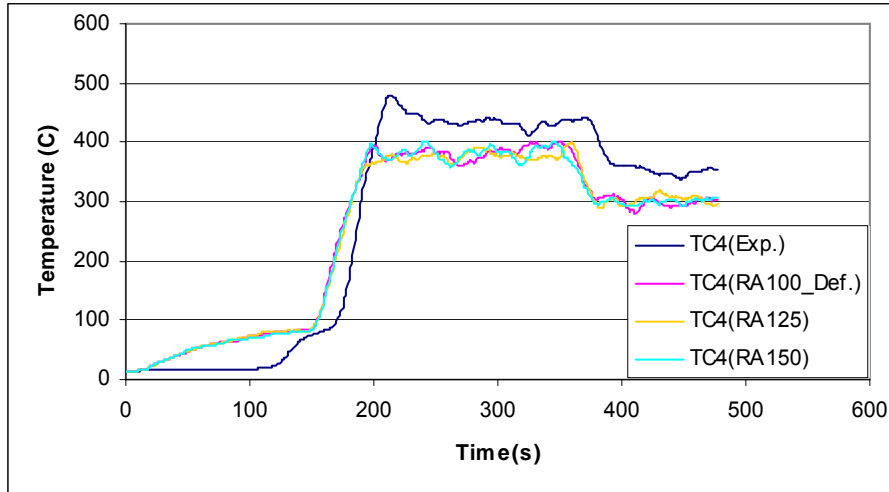


Figure C 23 Temperature Comparison (TC in Upper Layer) in Number Radiation Angles Sensitivity.

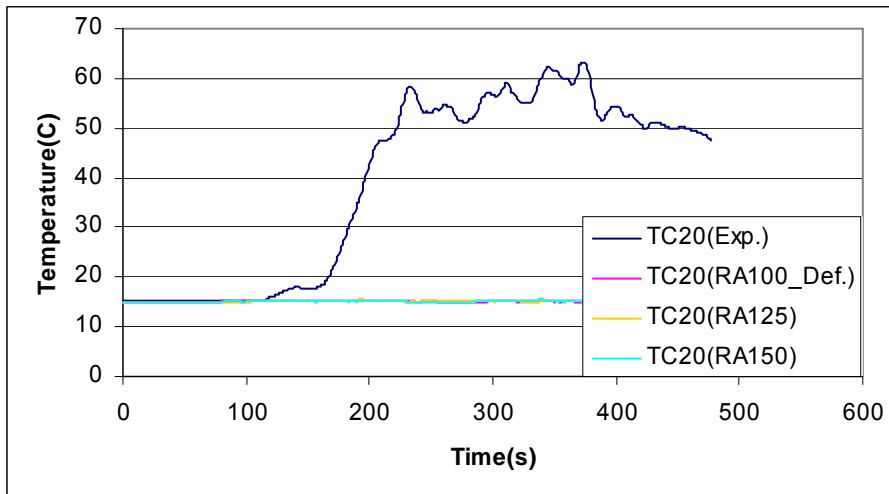


Figure C 24 Temperature Comparison (TC in Lower Layer) in Number Radiation Angles Sensitivity.

C2.2.3 Summary

Several values for the angle increment parameter are tried to improve the radiation calculation in FDS. As the number of radiation angles increases, the predictions somewhat improve. When the trade-off between the radiation calculation improvements and numerical costs is considered, a default value (=5) for angle increment is favored to use. Generally, the FDS predictions show a

good agreement with the experimental data. The large discrepancy in the temperature in the lower layer is caused mostly by the radiation effect in the experimental data.

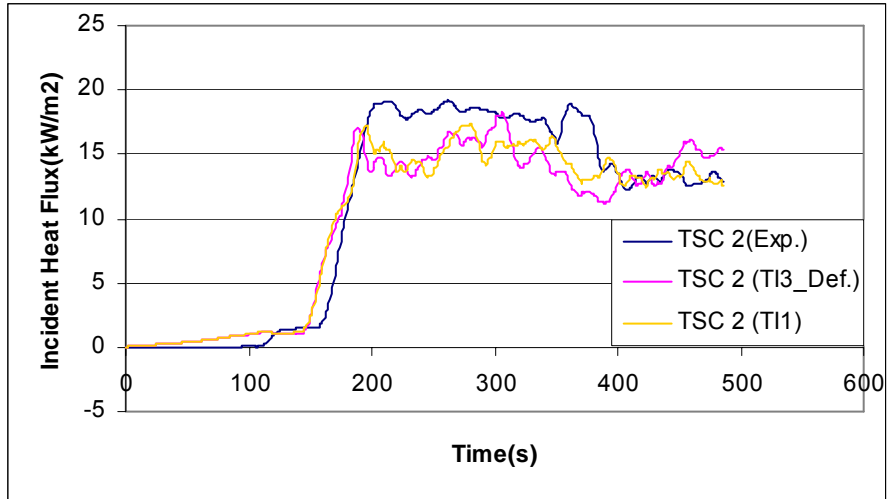
C2.3 Time Step Increment Sensitivity Analysis

C2.3.1 Descriptions of Time Step Increment Analysis

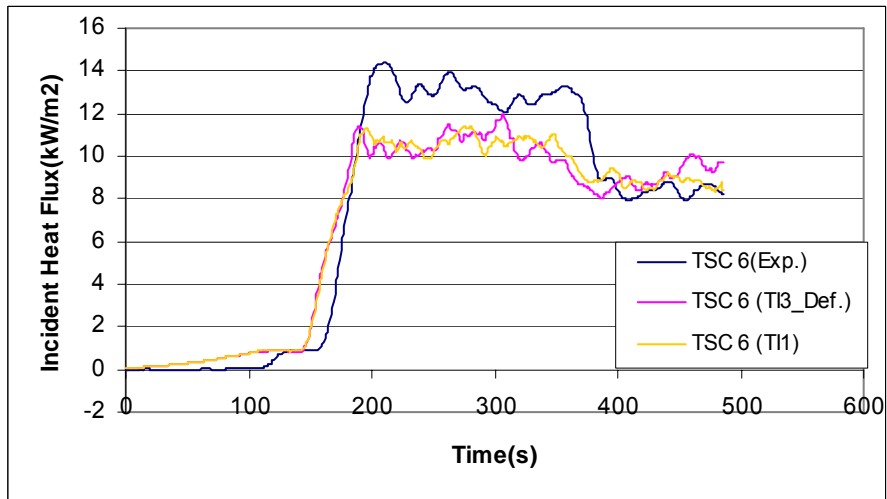
The parameter of time step increment is defined as the frequency of calls to the radiation solver. A default value for this parameter is three. The time step increment is changed from three to one and investigated the subsequent effects. The propane characterization experiment is used as a reference. The FDS domain is constructed as close as the experimental set-up. The configuration of personal computer used is 3.6 GHz with 1 GB RAM and the operating system is Windows XP.

C2.3.2 Results and Discussion

Figure C 25, Figure C 26, and Figure C 27 represent the comparisons of incident heat fluxes, room temperatures in the upper layer, and room temperature in the lower layer. The FDS predictions little change as the time step increment is varied. The discrepancies in the incident heat fluxes and the temperatures between the simulations are both within 1%. The FDS predictions show a good agreement with the experimental data. It is noted a large discrepancy is observed for the temperature in the lower layer due to the radiation from hot layer to bare bead thermocouple in cold layer in the experiment. It is worthy to note that the computation time is increased by about 22 % from a default value case (=3) to the reduced value case (=1) (80.4 hr -> 98 hr).



(a)



(b)

Figure C 25 Incident Heat Flux Comparisons at (a) TSC2 and (b) TSC6 in Time Step Increment Sensitivity.

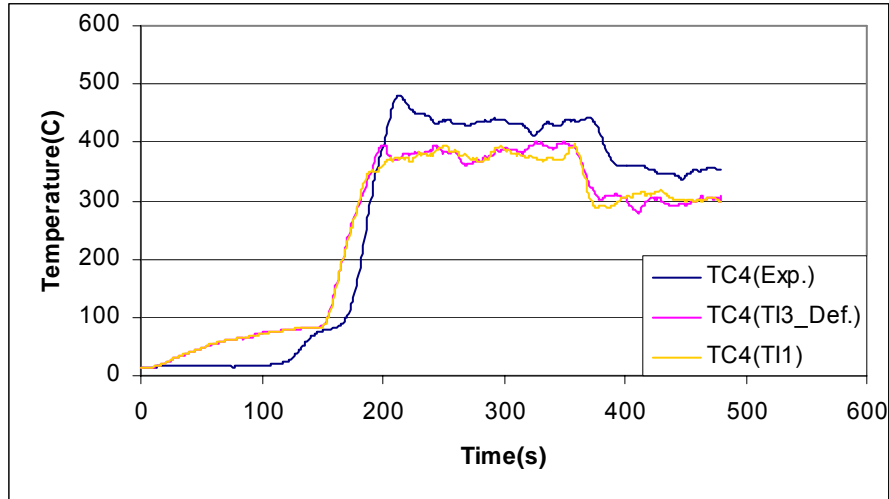


Figure C 26 Temperature Comparison (TC in Upper Layer) in Time Step Increment Sensitivity.

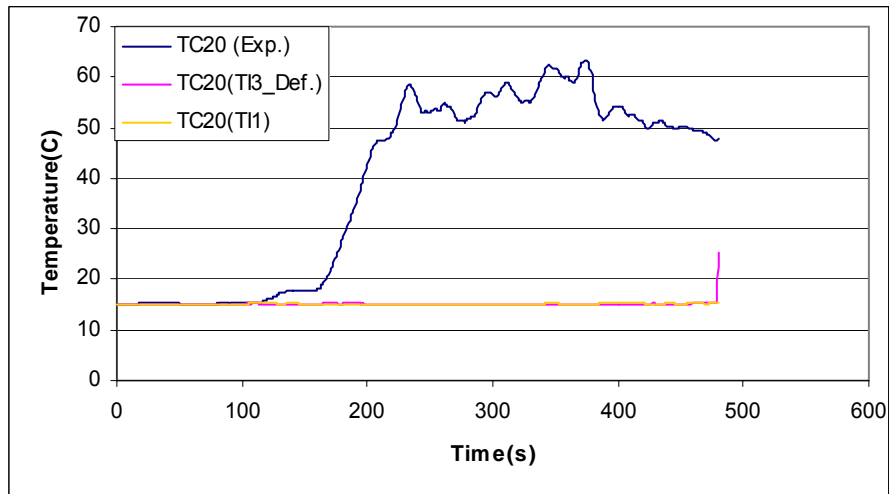


Figure C 27 Temperature Comparison (TC in Lower Layer) in Time Step Increment Sensitivity.

C2.3.3 Summary

The time step increment parameter is reduced from a default value (=3) to one to improve the radiation calculation in FDS. The variations of that parameter little effect on the output. The FDS predictions show a good agreement with the experimental data. A large discrepancy in the temperature in the lower layer is caused mostly by the radiation effect in the experimental data. When the trade-

off between the radiation calculation improvements and numerical costs is considered, a default value for time step increment is favored to use.

C3 Parameters in the REAC (Radiative Fraction)

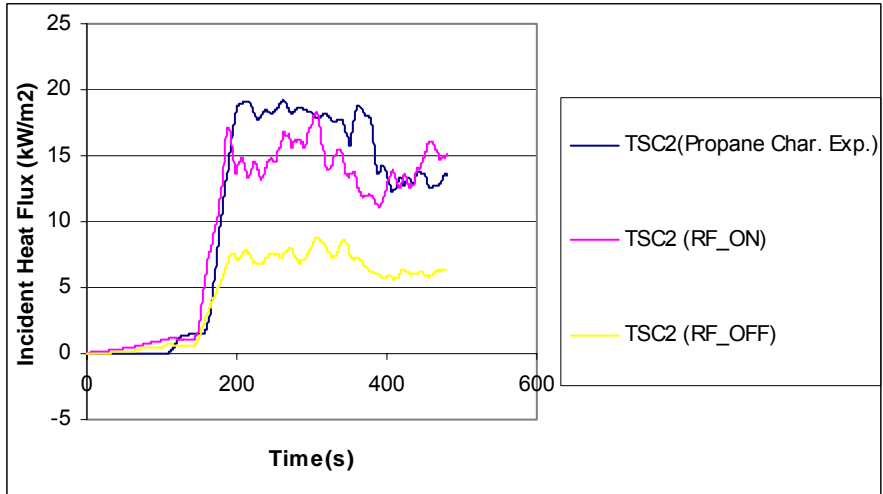
C3.1 Radiative Fraction Sensitivity Analysis

C3.1.1 Descriptions of Radiative Fraction Analysis

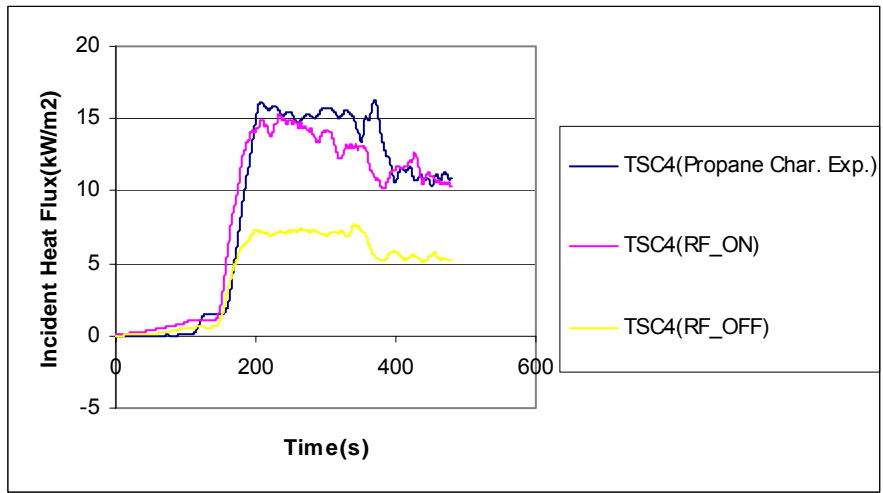
The parameter of radiative fraction is defined as the fraction of thermal radiation energy released from fire. As described in Eqn. A.38, inaccurate estimations of temperatures near flames results in the use of radiative fraction for better radiation estimations. By default, a radiative fraction of 0.35 is used. For the comparison purpose, the radiative fraction is turned off by setting the radiative fraction value to zero. The two simulation predictions (on/off radiative fraction) and the propane characterization experimental data are compared. The FDS domain is constructed as close as the experimental set-up.

C3.1.2 Results and Discussion

The incident heat flux and temperature comparisons between the FDS simulations and the propane characterization experiment are represented in Figure C 28 and Figure C 29. When the radiative fraction is turned off, the incident heat fluxes are dropped by approximately 40 %, which are more deviated from the experimental data. It is evident that a radiative source term inside the flame zone is determined by a method using radiative fraction (See Eqn. A.39). The temperatures between two FDS simulations (on/off radiative fraction) are not sensitive in comparison with the incident heat fluxes, and the differences are within 10%.

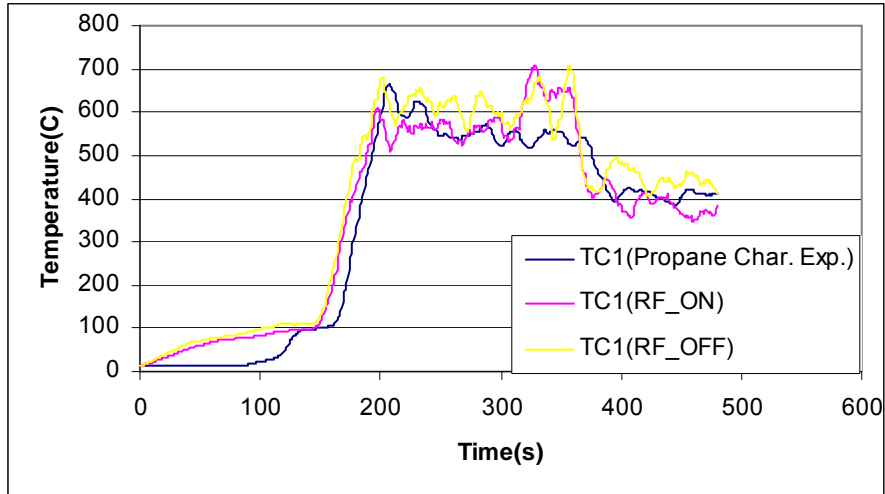


(a)

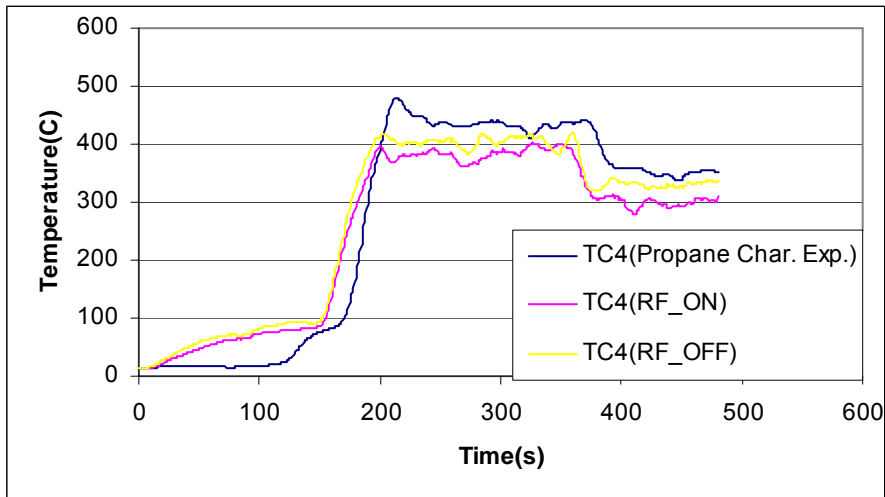


(b)

Figure C 28 Incident Heat Flux Comparisons at (a) TSC2 and (b) TSC4 in Radiative Fraction Sensitivity.



(a)



(b)

Figure C 29 Temperature Comparisons at (a) TC1 and (b) TC4 in Radiative Fraction Sensitivity.

C3.1.3 Summary

The radiative fraction effects on heat fluxes emitted near flames by influencing to a radiation source term. This shows one of the methods using radiative fraction and heat release rate per unit volume (Eqn. A.39) is dominant in the calculation of a radiation source term near flames. It is recommended to include the radiative fraction in the FDS calculation. The radiative fraction is considered to have a universal character by using a constant value in FDS.

Therefore, it is appropriate to use a proper value of radiative fraction for each scenario.

C4 Appendix C References

- [1] J. Smagorinsky, "General Circulation Experiments with the Primitive Equations. I. The Basic Experiment," *Monthly Weather Review*, Vol. 91, No.3, pp. 99-164, 1963.
- [2] K. McGrattan and G. Forney, "FDS V.4 Technical Reference Guide," NIST Special Publication 1018, National Institute Standards and Technology, Gaithersburg, MD, 2005.
- [3] J.W. Deardorff, "A Three-dimensional Numerical Study of Turbulent Channel Flow at Large Reynolds Numbers," *Journal of Fluid Mechanics*, Vol. 41, pp. 435-452, 1970.
- [4] P. Moin and J. Kim, "Numerical Investigation of Turbulent Channel," *Journal of Fluid Mechanics*, Vol. 118, pp. 341-377, 1982.
- [5] S. Murakami, "Overview of Turbulence Models Applied in CWE-1997," *Journal of Wind Engineering and Industrial Aerodynamics*, Vol. 74-76, pp. 1-24, 1998.
- [6] R.A. Clark, J.H. Ferziger, and W.C. Reynolds, "Evaluation of Subgrid-Scale Models using an Accurately Simulated Turbulent Flow," *Journal of Fluid Mechanics*, V. 91, No. Part 1, pp. 1-16, 1979.
- [7] M. Antonopoulos-Domis, "Large-eddy Simulation of a Passive Scalar in Isotropic Turbulence," *Journal of Fluid Mechanics*, Vol.104, pp. 55-79, 1981.
- [8] V. Huijnen, et al., "Validation of the LES Approach in Kiva-3V on a Square Duct Geometry," *International Journal for Numerical Methods in Engineering*, Vol. 64, No.7, pp. 907-919, 2005.
- [9] W. Zhang, et al, "Turbulence Statistics in a Fire Room Model by Large Eddy Simulation," *Fire Safety Journal*, Vol. 37, No. 8, pp. 721-752, 2002.
- [10] J.A. Barnard, and J.N. Bradley, *Flame and Combustion*, 2nd ed., Chapman and Hall, New York, 1985.
- [11] M. Germano, U. Piomelli, P. Moin, and W. Cabot, "A Dynamic Subgrid-Scale Eddy Viscosity Model," *Physics of Fluids A*, Vol. 3, No. 7, pp. 1760-1765, 1991.

- [12] F.T.M. Nieuwstadt, P.J. Mason, C.-H. Moeng, and U. Schumann, "Large Eddy Simulation of the Convection Boundary Layer: A Comparison of Four Computer Codes," Proceedings of the 8th International Symposium on Turbulent Shear Flows, Technical University of Munich, Munich, Germany, 1991, pp. 343-367.
- [13] Yoshizawa A. "Eddy-viscosity-type Subgrid-scale Model with a Variable Smagorinsky Coefficient and its Relationship with the One Equation Model in Large Eddy Simulation," Physics of Fluids A, Vol. 3, No. 8, pp. 2007-2009, 1991.
- [14] F.M. White, Heat and Mass Transfer, Addison-Wesley, Reading, MA, 1988.
- [15] G. Cox and R. Chitty, "A Study of the Deterministic Properties of Unbounded Fire Plumes," Combustion and Flame, Vol. 39, No. 2, pp. 191-209, 1980.

Appendix D Propane Characterization Experiment

A standard ISO 9705 test compartment [1] in Fire Science Lab at WPI was used for the propane characterization experiment. One thermocouple rake that consists of Type K thermocouples was constructed to measure compartment temperature profiles. Also, thin skin calorimeters were constructed and distributed to evaluate incident heat flux in the compartment. The heat release rates were calculated via three methods using oxygen and carbon dioxide concentrations. Both the room temperature profiles and the radiation corrected temperature profiles are presented. The net heat flux and heat losses were estimated using the acquired temperature from the thin skin calorimeter to calculate the incident heat flux. In addition, the extinction coefficients, smoke production rates, and mass loss rates are reported.

D1 Experimental Configurations and Conditions

D1.1 Test Compartments

A standard ISO 9705 test compartment was used for the propane characterization experiment. This compartment is 2.4 m x 3.6 m x 2.4 m in dimension, and one of the short walls (2.4 m x 2.0 m) was open, see Figure D 1. As a matter of convenience, a “North” is set and indicated in Figure D 1. This compartment has a ceiling and walls that were covered with three layers of 0.016 m (5/8”) gypsum wallboard backed by one layer of 0.012 m (1/2”) fir plywood while the floor was covered with one layer of 0.016 m (5/8”) gypsum wallboard. An exhaust hood was located next to and above the compartment opening (See Figure D 2). The hood captured the combustion products from the fires. The sampling gas from the hood was sent to the Large Oxygen Depletion System (LODS) to measure CO, CO₂, and O₂ concentration. Also, gas velocity, gas temperature, pressure, and percent light transmission in the exhaust duct were acquired.

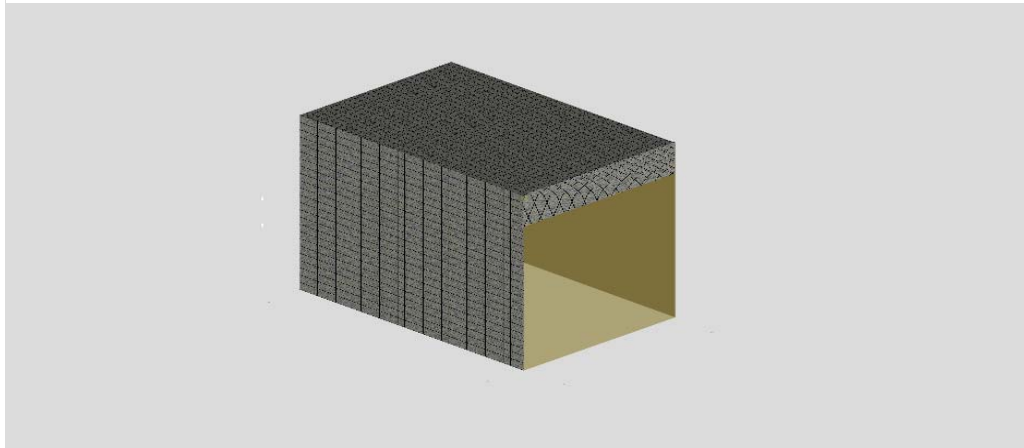
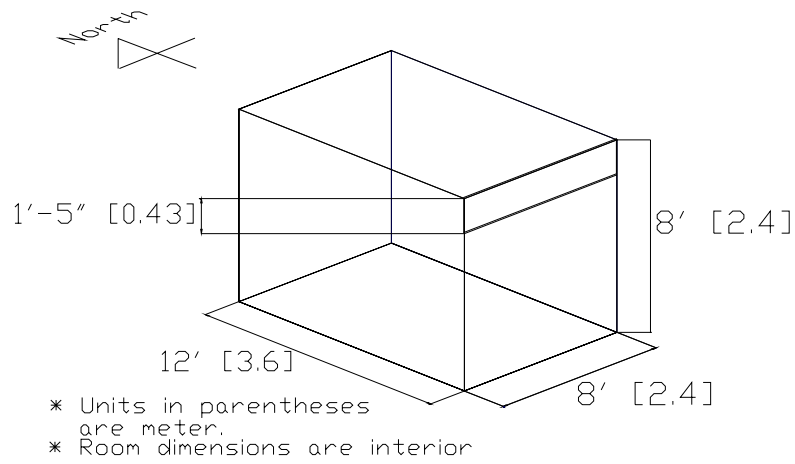


Figure D 1 Standard ISO 9705 Test Compartment

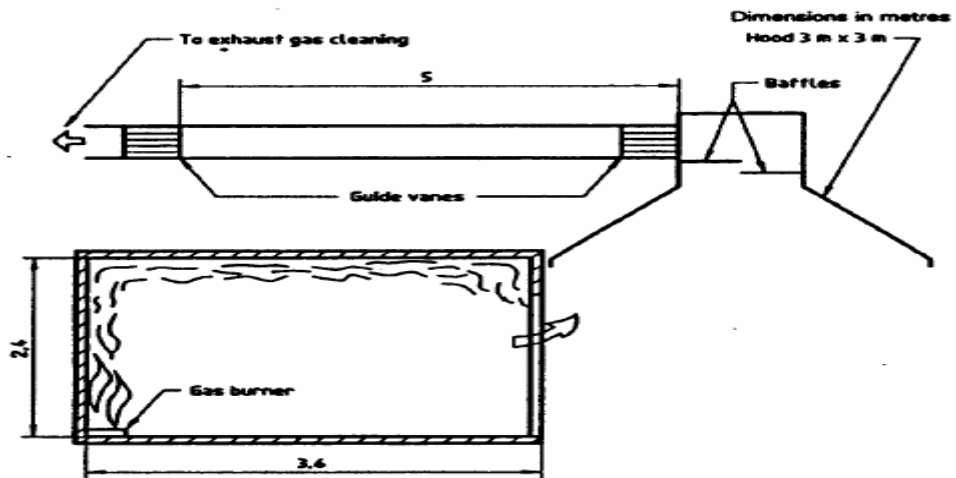


Figure D 2 ISO 9705 Compartment and Hood Arrangement [2]

D1.2 Room Contents and Gas burner

The locations of content and instruments are presented in detail in Figure D 3 through Figure D 5. Various propane supply rates were used throughout the experiment as the source fire. The locations of the gas burner, fuel type, and supply rate for each experiment are presented in Table D 1. The rectangular porous gas burner (0.66 m x 0.36 m) and the propane gas as a source fire were used for the experiment. The properties of propane are presented in Table D 2.

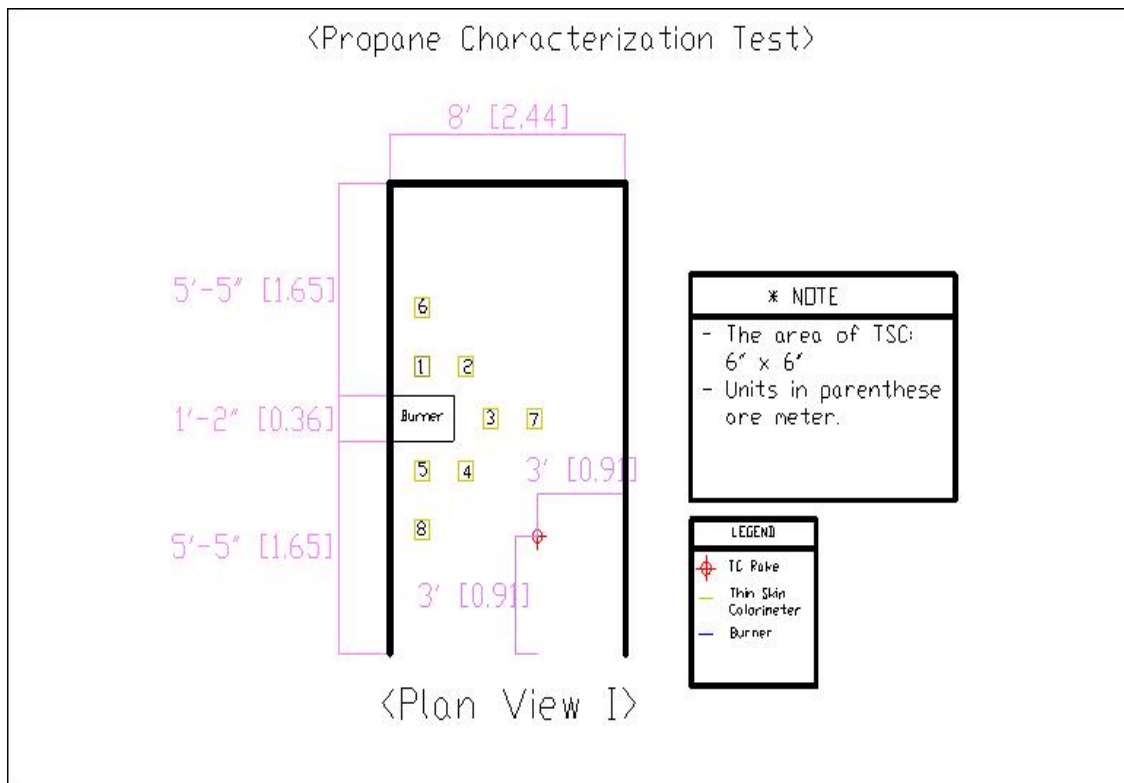


Figure D 3 Configuration of Content and Instruments in Propane Characterization Experiment, Plan View I.

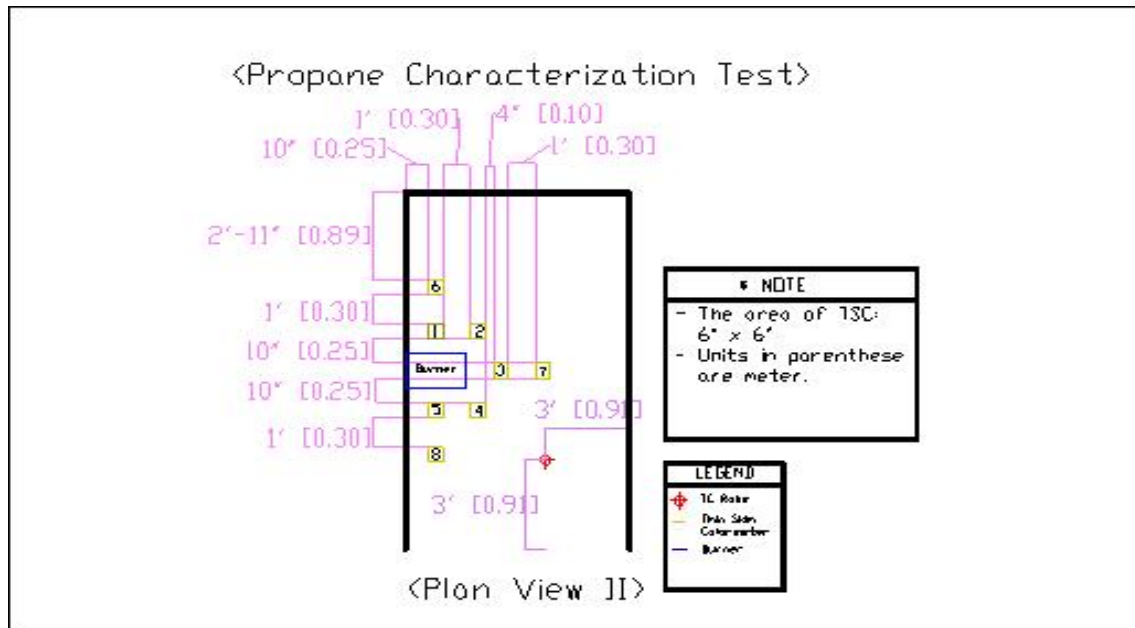


Figure D 4 Configuration of Content and Instruments in Propane Characterization Experiment, Plan View II.

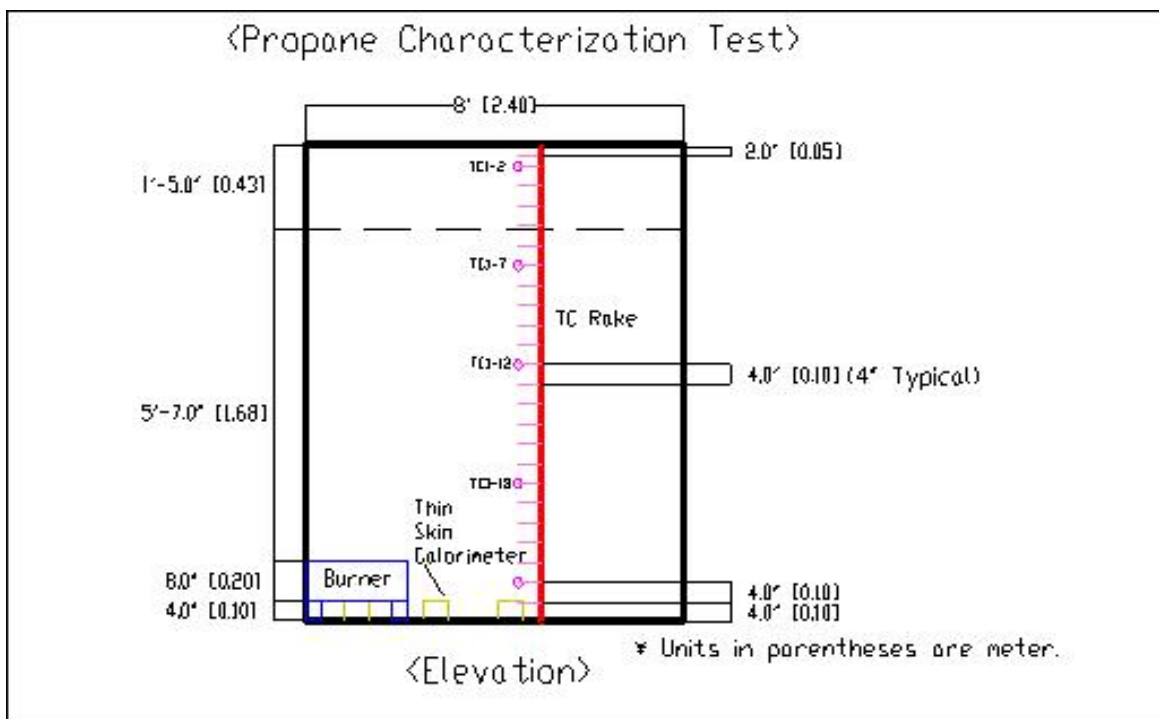


Figure D 5 Configuration of Content and Instruments in Propane Characterization Experiment, Elevation View.

Table D 1 Burner Locations, Fuels, and Supply Rates.

Test	Burner Location	Fuel	Supply Rate
[1]	1.83 m from North wall, against West wall	Propane	1 MW → 700kW → 100kW

Table D 2 Propane Properties.

Molecular Weight	44.11 [kg/kg·mole]
Liquid Density at 0 C and 760 Torr	1.967 [kg/m ³]
Heat of Combustion (total)	46.0 [kJ/g]
Heat of Combustion (chemical)	43.7 [kJ/g]
Lower Flammable Limit	2.1 [%]
Upper Flammable Limit	9.5 [%]

D2 Instrumentation

D2.1 Thermocouple Rakes

The rake used in the experiment was composed of a vertical array of 24 thermocouples spaced 0.1 m intervals from floor to ceiling, but the top thermocouple from the ceiling was located 0.05 m below the ceiling, see Figure D 6. The rake has five “isotherm stations” to allow radiation correction of the acquired temperatures. Each station consisted of 0.81 mm in diameter (20 AWG), 0.51 mm (24 AWG), 0.32 mm (28 AWG), and 0.25 mm (30 AWG) wires that were positioned closely together. The stations were positioned at 0.15 m, 0.65 m, 1.15 m, 1.75 m, and 2.25 m from the ceiling. ANSI type K glass-

insulated high temperature wires with Special Limited Error (SLE)* were used for the 20 and 24 AWG wires, and SLE glass insulated wires for the 28 and 30 AWG wires. The specifications of the thermocouple wires used are presented in Table D 3.

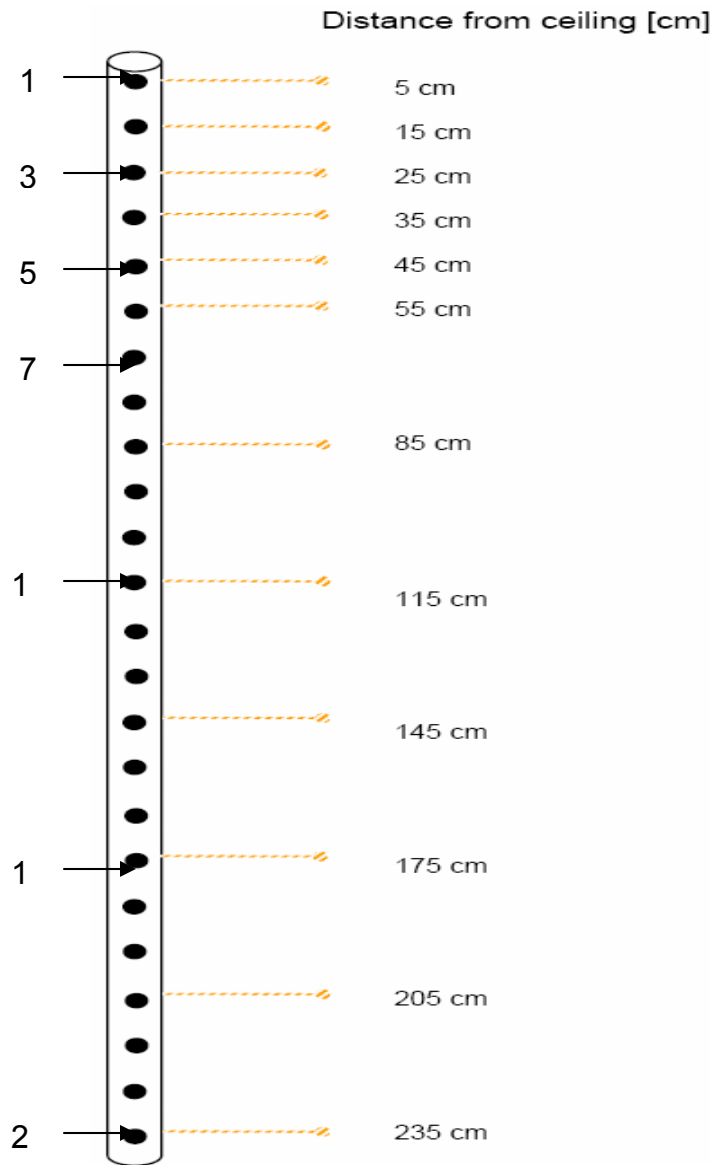


Figure D 6 Thermocouple Array Spacing [2].

* Tolerance value is 1.1°C or 0.4% (whichever value is greater) in the temperature range of 0°C to 1250°C

Table D 3 Thermocouple Wire Specifications [3].

AWG No.	Insulation	Insulation		Max.Tem p	
		Conductor	Overall	[°F]	[°C]
20	High Temperature Glass	High Temp. Glass	High Temp. Glass	1300	704
24	High Temperature Glass	High Temp. Glass	High Temp. Glass	1300	704
28	Glass	Glass Braid	Glass Braid	900	482
30	Glass	Glass Braid	Glass Braid	900	482

D2.2 Thin-Skin Calorimeters

Thin Skin Calorimeters (TSCs) were constructed as shown in Figure D 7. Inconel 718 plate was used and cut into pieces 0.15m x 0.15m. The properties of Inconel are presented in Table D 4. The exposed surfaces of these metals were painted with Pyromark High Temperature Paint 2500 that has solar absorptivity of 0.95 [4]. The maximum performance temperature of the paint is up to 1093 °C (2000 °F) on Inconel. Three layers of ceramic fiberboard, Duraboard H, were attached to the inconel plate to provide an insulating substrate. The properties of fiberboard are summarized in Table D 5.

Three thermocouple wires, high-temperature glass insulated Type K 24 AWG wires with SLE, in the TSCs were installed to measure temperatures. One wire was intrinsically welded to the unexposed side of the inconel plate, and two wires formed into beads were placed between the substrates. These acquired temperatures were used to estimate the net heat flux and all losses from the inconel plates.

Thin Skin Construction:

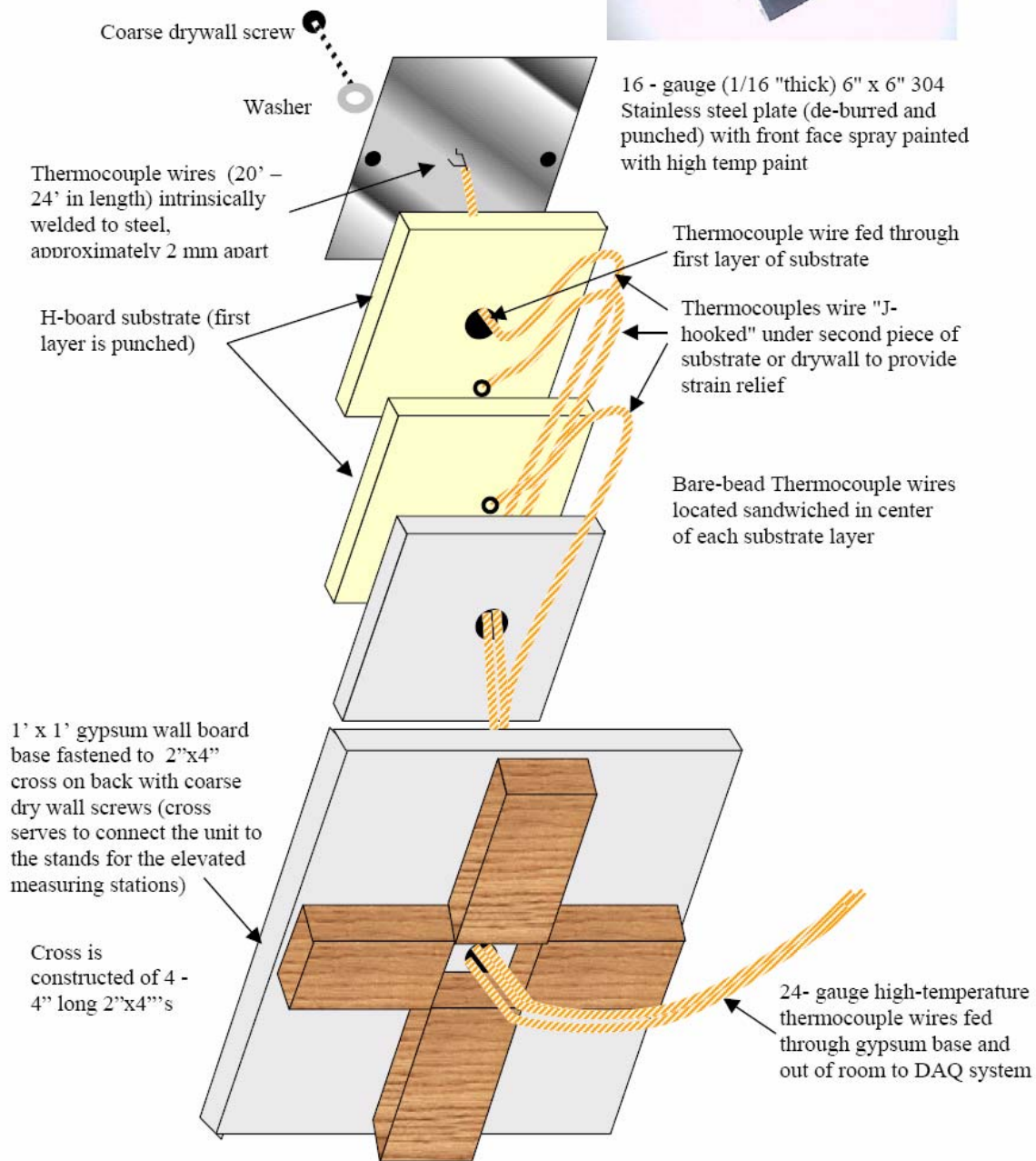


Figure D 7 Thin-Skin Calorimeter Construction [2]

Table D 4 Inconel 718 [5].

HEAT CAPACITIES	
Inconel	435 [J/kgK]
THERMAL CONDUCTIVITIES	
Inconel	11.4 [W/mK]
DENSITY	
Inconel	8190 [kg/m ³]
THICKNESS	
Inconel	0.0016 [m]

Table D 5 Properties of Ceramic Fiberboard [6].

Property		Ceramic Fiberboard (Duraboard H)
Heat Capacities		1172 [J/kgK]
Density		415 [kg/m ³]
Thickness		0.0127 [m]
Thermal Conductivities	260 °C	0.098 [W/mK]
	538 °C	0.121 [W/mK]
	816 °C	0.161 [W/mK]
	1093 °C	0.228 [W/mK]

Table D 6 Information of Thin Skin Calorimeters.

Test	Material	Size [m]	Number of TSCs
[1]	Inconel	0.15 x 0.15	8

D3 Data Reduction

The data reduction methods used are presented in this chapter. The data of HRR, heat flux, room temperatures, and smoke properties were collected through the experiment.

D3.1 Heat Release Rate (HRR)

This section addresses three methods applied to calculate a heat release rate (HRR) such as oxygen consumption and carbon dioxide production calorimetries. The results and discussion are presented in Section D4.

D3.1.1 Oxygen Based Heat Release Rate

The gas sample is captured from the exhaust duct and is sent to the analyzer to determine the concentration of oxygen. The amount of depleted oxygen can be converted to a heat release rate [7]. A nearly constant value of heat of 13.1 MJ/kg(O₂) is released per unit mass of oxygen consumed for most organic materials. Parker [8] developed equations for HRR based on typical measurements of exhaust gas concentrations such as only oxygen or containing carbon dioxide, carbon monoxide, and water vapor. Parker's equations were used to calculate the HRR based on the assumption of complete combustion. The first step is the calculation of oxygen depletion factor:

$$\Phi = \frac{X_{O_2}^{A_0} * [1 - X_{CO_2}^A - X_{CO_2}^A] - X_{O_2}^A * [1 - X_{CO_2}^{A_0}]}{X_{O_2}^{A_0} * [1 - X_{O_2}^A - X_{CO_2}^A - X_{CO}^A]} \quad (D 1)$$

where $X_{O_2}^{A_0}$, $X_{CO_2}^{A_0}$, $X_{O_2}^A$, $X_{CO_2}^A$, and X_{CO}^A are respectively the ambient O₂ mole fraction, the ambient CO₂ mole fraction, the measured O₂ mole fraction in analyzer, the measured CO₂ mole fraction in analyzer, and the measured CO mole fraction in analyzer. Since the concentration of CO₂ and CO has little effect, Eqn. D1 simplifies to:

$$\Phi = \frac{X_{O_2}^{A_0} - X_{O_2}^A}{X_{O_2}^{A_0} * [1 - X_{O_2}^A]} \quad (D 2)$$

Then, it is necessary to convert the measured pressure differential from in-H₂O to Pa for the next calculation steps:

$$P = P[\text{in-H}_2\text{O}] * 284.48[\text{Pa} / \text{in-H}_2\text{O}] \quad (\text{D } 3)$$

where P is the pressure differential across the probe. The next step is the calculation of gas velocity in the system:

$$\dot{V}_s = 22.4 jkA \left[\frac{P}{T_s} \right]^{1/2} \quad [\text{m}^2 / \text{s}] \quad (\text{D } 4)$$

where j is 0.926 for a bi-directional probe, k is the velocity ratio from Table D 7, A is the duct cross-sectional area, T_s is the gas temperature in duct, P it the pressure differential across the probe from Eqn. D3.

The velocity ratios at the various flow-rates in duct are listed in Table D 7.

Then, the volume flow rate of air into the system is obtained as follows:

$$\dot{V}_A = \frac{\dot{V}_s}{(1 + (\alpha - 1)\Phi)} \quad [\text{m}^3 / \text{s}] \quad (\text{D } 5)$$

where α is the molar expansion factor (1.1 for unknown fuels).

Finally, the HRR can be calculated using the calculated variables above:

$$Q = E \left[\frac{M_{O_2}}{M_{air}} \right] * \rho_{air} * \dot{V}_A * \left[\frac{X_{O_2}^{Ao} - X_{O_2}^A}{1 - X_{O_2}^A} \right] \quad [\text{KW}] \quad (\text{D } 6)$$

where E is 13.1 MJ/kg(O₂) for unknown fuels and 12.9 MJ/kg(O₂) for propane.

(M_{O₂}/M_{air}) is the mass ratio of oxygen to air. ρ_{air} is the density of air referenced to an ambient temperature (kg/m³).

Table D 7 Velocity Ratio at the Various Flow-rates

Flow Setting	Velocity Ratio
Maximum	0.953
Medium	0.975
Minimum	0.954

D3.1.2 Carbon Dioxide Based Heat Release Rate (ASTM E-2058)

Tewason [9] developed the carbon dioxide generation (CDG) calorimetry. According to ASTM E-2058 [10], a heat release rate is determined as follows:

$$Q_{ch}'' = \Delta H_{CO_2}^* G_{CO_2}'' + \Delta H_{CO}^* G_{CO}'' \quad (D 7a)$$

$$\Delta H_{CO_2}^* = \frac{\Delta H_T}{\Psi_{CO_2}} \quad (D 7b)$$

$$\Delta H_{CO}^* = \frac{\Delta H_T - \Delta H_{CO} \Psi_{CO}}{\Psi_{CO}} \quad (D 7c)$$

where Q_{ch}'' is the chemical heat release rate (kW/m^2), $\Delta H_{CO_2}^*$ is the net heat of complete combustion per unit mass of CO_2 generated (kJ/g), ΔH_{CO}^* is the net heat of complete combustion per unit mass of CO generated (kJ/g), ΔH_T is the net heat of complete combustion per unit mass of fuel consumed (kJ/g), Ψ_{CO_2} is the stoichiometric yield for the maximum conversion of fuel to CO_2 (g/g), Ψ_{CO} is the stoichiometric yield for the maximum conversion of fuel to CO (g/g), G_{CO_2}'' is the generation rate of CO_2 ($\text{g/m}^2\cdot\text{s}$), and G_{CO}'' is the generation rate of CO ($\text{g/m}^2\cdot\text{s}$). The values for net heat of complete combustion per unit mass of CO_2 and CO produced are listed below.

Table D 8 Net Heat of Complete Combustion
per Unit Mass of CO_2 and CO Produced

Fuel	$\Delta H_{CO_2}^*$ (kJ/g)	ΔH_{CO}^* (kJ/g)
Unknown	13.3	11.1
Propane	15.3	14.0

In addition, generation rate of CO_2 and CO were obtained from the following equations:

$$G_{CO_2}'' = 1.52 * X_{CO_2} * \dot{m}_d \quad (\text{g/m}^2\text{s}) \quad (D 8a)$$

$$G_{CO}'' = 1.52 * X_{CO} * m_d \quad (\text{g/m}^2\text{s}) \quad (\text{D } 8\text{b})$$

$$m_d = V_s * \rho_{air} \quad (\text{D } 8\text{c})$$

where X_{CO_2} is the CO₂ mole fraction, X_{CO} is the CO mole fraction, m_d is the mass flow rate of combustion products in the exhaust duct (kg/s), and V_s is the gas velocity from Eqn. D4. Eqn. D8a, D8b, and D8c were modified from those stated in ASTM E-2058 because the equipment to measure the pressure differential was different. Another modification was including the amount of generated H₂O in the HRR calculation by substituting the following equation into Eqn. D8a:

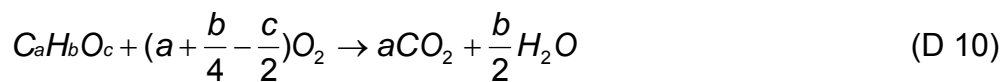
$$X_{CO_2} = \frac{X_{CO_2}^A (1 - X_{H_2O}^{Ao})}{1 + \frac{4}{3} X_{CO_2}^a} \quad \text{for a propane} \quad (\text{D } 9)$$

where $X_{CO_2}^A$ is the measured CO₂ mole fraction in analyzer and $X_{H_2O}^{Ao}$ is the ambient H₂O mole fraction. More details about Eqn. D9 are discussed in Section D3.1.3.

D3.1.3 CO₂ Based Heat Release Rate (Thermochemistry Technique)

A heat release rate can be expressed by the difference of the heat of formation between the products and reactants based on the three laws: conservation of energy, Hess' law of summation, and Lavoisier-Laplace law. The method developed by Enright and Fleischmann [11] uses the concentrations of CO and CO₂. It also accounts for the generated H₂O so that a bit more accurate value can be obtained.

First, set up the stoichiometric equation for the complete combustion of arbitrary fuel as follows:



Then, the HRR is expressed using the number of moles CO₂ generated:

$$\dot{q} = \left((\Delta H_f^0)_{CO_2} + \frac{b}{2a} (\Delta H_f^0)_{H_2O} - \frac{1}{a} (\Delta H_f^0)_{fuel} \right) \dot{n}_{CO_2}^g \quad (D 11)$$

where ΔH_f^0 is the heat of formation (kJ/mol).

The following relationships are used in Eqn. D.11:

$$\dot{n}_{CO_2}^g = X_{CO_2}^g \cdot \frac{\dot{m}_d}{M_e} \quad (D 12a)$$

$$X_{CO_2}^g = \frac{X_{CO_2}^a (1 - X_{H_2O}^0) - X_{CO_2}^0}{1 + \frac{b}{2a} X_{CO_2}^a} \quad (D 12b)$$

where \dot{m}_d is the mass flow rate of combustion products in the exhaust duct

(kg/s), and M_e is the molecular mass of exhaust gases ($\approx M_{a(dry)} = .02896 \frac{kg}{mol}$)

Then, Eqn. D11 is rearranged as follows:

$$\dot{q} = \left((\Delta H_f^0)_{CO_2} + \frac{b}{2a} (\Delta H_f^0)_{H_2O} - \frac{1}{a} (\Delta H_f^0)_{fuel} \right) \left(\frac{X_{CO_2}^a (1 - X_{H_2O}^0) - X_{CO_2}^0}{1 + \frac{b}{2a} X_{CO_2}^a} \right) \frac{\dot{m}_e}{M_e} \quad (D 13)$$

where ΔH_f^0 is the heat of formation [kJ/mol], $X_{H_2O}^0 (= \frac{P}{760} \frac{RH}{100})$ is the ambient

H_2O mole fraction, P = Water vapor pressure (mm Hg) (= 23.78 at 25°C), and

RH is the relative humidity (%).

Once the listed data for the heat of formations in the SFPE Handbook [12] are used, the HRR for the commercial fuels can be calculated using Eqn. D13 above.

D3.2 Gas Temperature and Radiation Corrected Temperature

Thermocouple rakes were constructed to measure the gas temperatures. However, the measured temperatures using the bare-bead thermocouples do not always represent the true temperature of surrounding gases due to radiation heat transfer from or to the bare-bead. In theory, a thermocouple having an infinitely small diameter reads the true gas temperature. It is impossible to use the

infinitely small diameter wires, but it was tried to estimate a true gas temperature through extrapolation; therefore, five “isotherm stations” were uniformly distributed on each rake. Young’s correlation method [13] containing radiative effects was used to do a radiation correction. It is reported the method used is valid just for the heating phase and steady state [6]. The following expression is the heat balance on the surface of thermocouple:

$$\rho_{TC} c_{TC} d_{ch} \frac{dT_N}{dt} = h_N (T_g - T_N) + \varepsilon \sigma (T_e^4 - T_N^4) \quad (D 14)$$

where ρ_{TC} is the thermocouple material density, c_{TC} is the thermocouple material specific heat, d_{ch} is the thermocouple characteristic dimension, T_N is the thermocouple (bead) temperature, h_N is the average heat transfer coefficient over thermocouple, T_g is the gas(true) temperature, T_e is the effective environment (radiating) temperature, ε is the thermocouple material emissivity, and σ is the Stefan-Boltzman constant. As Young [13] recommended, the convective heat transfer coefficient, h_N , was calculated using the correlations of Collis and Williamson [14] for flow over the wires. The correlation makes use of the temperature loading function to account for variable gas properties:

$$Nu \left(\frac{T_m}{T_g} \right)^{-0.17} = 0.24 + 0.56 Re^{0.45} \quad (D 15)$$

where T_m is the temperature half-way between the gas temperature and the thermocouple temperature and Re is the Reynold’s number. A velocity of 0.5 m/s as typical for compartment fire was used to calculate Reynold’s number. It is assumed that the emmissivity of thermocouple is set to 0.8 for dull, oxidized metal. Four different size wires will receive and emit more or less radiation depending on their overall area. The true gas temperature would be obtained using the measured temperatures from two different sizes of wires:

$$T_g = \left[\frac{1}{h_2 - h_1} \right] \left[\rho_{TC} C_{TC} \left[d_{ch-2} \frac{dT_2}{dt} - d_{ch-1} \frac{dT_1}{dt} \right] + h_2 T_2 - h_1 T_1 - \varepsilon \sigma (T_2^4 - T_1^4) \right] \quad (D 16)$$

Six true gas temperatures were calculated because six thermocouple pairings would be obtained from the four different wires. The results from the 20 AWG and 30 AWG pairing were reported since this pairing shows the most consistency for each experiment. Correction profiles were made by interpolating the correction factors between two closest “isotherm stations” to be applied to all thermocouples. It is noted that this method is inconsistent under “rapidly” changing environments in terms of the temperature. In summary, this correction method provides reasonable and applicable results for the “steady state” or “slowly” changing heating phase.

D3.3 Incident Heat Flux

Heat flux was measured using thin skin calorimeters (TSCs). Based on ASTM-E-457 [15], the analysis assumes that heat flows in one-dimension through a metal calorimeter and the metal plate is thin enough to employ ‘lumped thermal capacity analysis’:

$$\dot{q}_{net} = \rho c \delta \frac{dT}{dt} \quad (D 17)$$

where \dot{q}_{net} is the heat transfer rate (W/m^2), ρ is the metal density (kg/m^3), c is the metal specific heat ($J/kg \cdot K$), δ is the metal thickness (m), and $\frac{dT}{dt}$ is the back surface temperature rise rate (K/s). To get the incident heat flux from Eqn. D17, it is necessary to account for heat losses. The governing equation is as follows:

$$\rho c \delta \frac{dT}{dt} = \alpha q_i'' - \varepsilon \sigma (T^4 - T_0^4) - h_{conv} (T - T_g) - (4\varepsilon_b \sigma T^3 + h_{cr}) (T - T_1) - q_{lat}'' \quad (D 18)$$

The left hand side of Eqn. D18 represents the rate of increase in energy stored per unit area of the metal plate. The first term of the right hand side of equation is the heat flux absorbed by the black painted plate, and the second term is the heat flux re-radiated from the surface to the ambient environment. The painted

plate is presumed to have surface emissivity and absorptivity that are both equal to 0.95. The third term on the right is the convective heat loss from the top surface of the metal plate. The correlation to calculate the convective heat transfer coefficients, h_{conv} , used in this work are tabulated in Table D 9. The next term on the right represents a contact resistance developed by de Ris and Khan [16]. The contact resistance shows the heat transfer across the interface, from the metal plate to the insulation substrate. The last term stands for the lateral heat conduction. Based on the method developed by de Ris and Khan [16], the contact resistance was applied to account for the heat losses into the ceramic fiberboard. The thermal resistance is modeled by a temperature jump, $T-T_1$, where T_1 is a surface temperature of insulation substrate and T is a temperature of metal plate. Both radiation, $4\epsilon_b\sigma T^3(T_S-T_1)$, and conduction, $h_{cr}(T-T_1)$, heat transfer occur across the interface. h_{cr} is a contact resistance heat transfer coefficient. The contact resistance heat transfer coefficient of $430 \text{ Wm}^{-2}\text{K}^{-1}$ and the thermal conductivity of $0.135 \text{ WK}^{-1}\text{m}^{-1}$ were chosen for the analysis [6]. An implicit finite difference method was employed to calculate the surface temperature of substrate. It was reported that the lateral conduction losses account for less than 5% of the incident flux [6]; therefore, the lateral conduction losses was excluded in the incident heat flux analysis.

Table D 9 Convection Correlation for Evaluation of Thin Skin Calorimeter.

Flow	Location	Type	Equation	Restrictions
Free/Natural	Wall (vertical)	Average ($T_s=\text{const}$)	$\bar{Nu}_L = \left\{ 0.825 + \frac{0.387Ra_L^{1/6}}{\left[1 + (0.492/Pr)^{9/16}\right]^{8/27}} \right\}^2$	None
	Floor & Ceiling (hot surface up or cold surface down)	Average ($T_s=\text{const}$)	$\bar{Nu}_L = 0.54Ra_L^{1/4}$ $\bar{Nu}_L = 0.15Ra_L^{1/3}$	$10^5 \leq Ra_L \leq 10^7$ $10^7 \leq Ra_L \leq 10^{10}$

D3.4. Smoke Properties

Extinction coefficient and smoke production rate (SPR) are used to represent the smoke properties. The extinction coefficient is calculated from:

$$k = \frac{1}{L} \ln \left[\frac{I_o}{I} \right] \quad (D 19)$$

where k is the extinction coefficient (m^{-1}), L is the extinction beam path length, I_o is the beam intensity with no smoke, and I is the actual beam intensity.

Smoke production rate is achieved using a following relationship:

$$SPR = k \cdot \dot{V}_s \text{ [m}^2\text{/s]} \quad (D 20)$$

where k is the extinction coefficient [m^{-1}] and \dot{V}_s is the gas velocity [m^3/s] obtained from Eqn. D4.

D4 Results and Discussion

Data obtained from the propane characterization experiment are shown in Figure D 8 (heat release rate), Figure D 9 (uncorrected compartment temperature), Figure D 10 (corrected compartment temperature), Figure D 11 (incident heat flux), Figure D 12 (Extinction Coefficient), and Figure D 13 (smoke production rate). A photo at 1 MW fire is presented in Figure D 14. "T1" and "B" in Figure D 9 and Figure D 10 represent TC rake #1 and 24 AWG wire, respectively. Also, the numbers in Figure D 9 and Figure D 10 indicate the locations of TCs in the TC rake, see Figure D 6. As can be seen in Figure D 8, oxygen based HRR was 10~20% higher than carbon dioxide based HRR. It is presumed that the amount of generated soot played in a role as soot is removed from the gas sample before gas analysis. The temperature, incident heat flux, and smoke data show the similar trend consistent with the HRR. It is noted that the corrected temperatures under a rapid change environment in terms of temperature are not reliable because Figure D 10 shows the corrected temperatures in the lower (cool) layer go below the ambient temperature around 383 seconds.

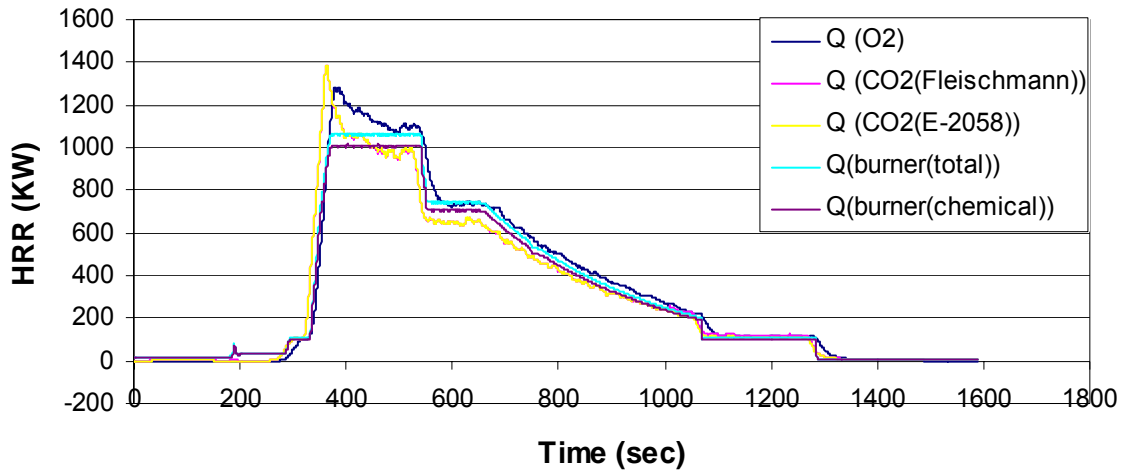


Figure D 8 Heat Release Rate in Propane Characterization Experiment.

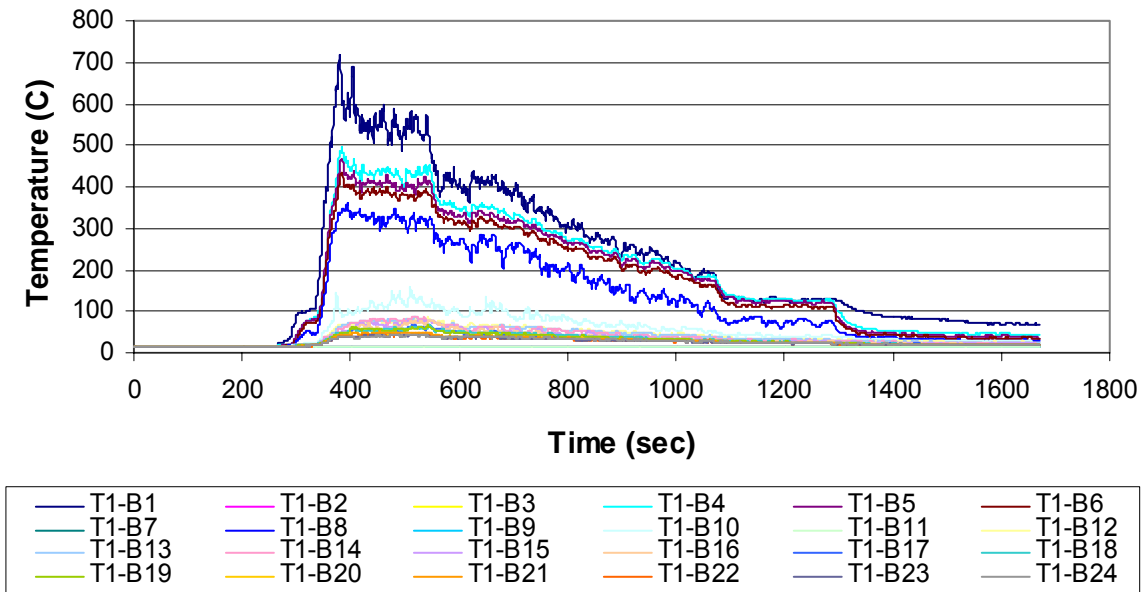


Figure D 9 Uncorrected Room Temperature in Propane Characterization Experiment.

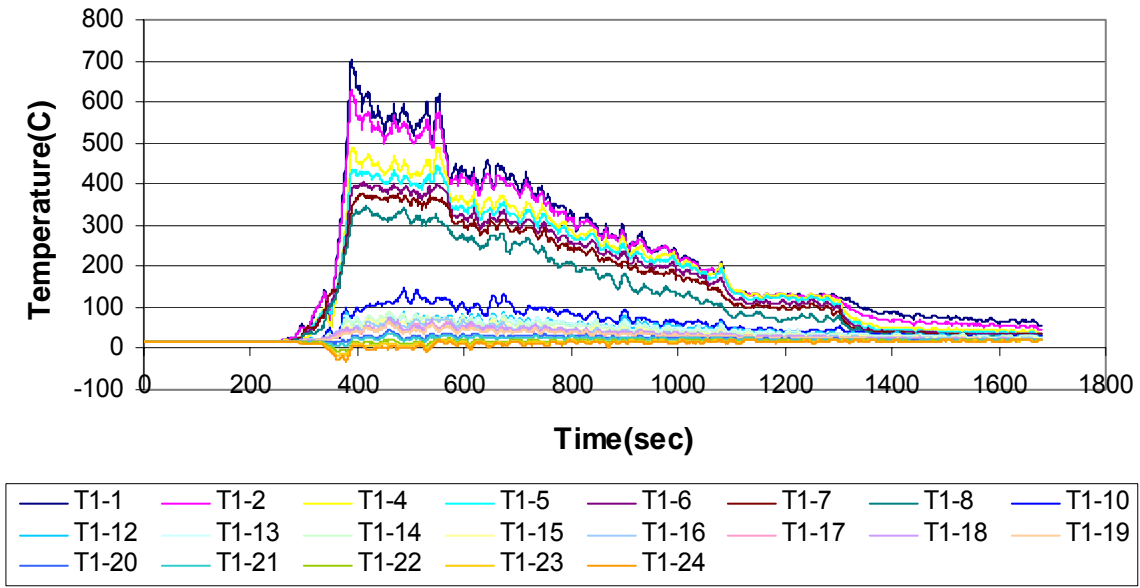


Figure D 10 Radiation Corrected Room Temperature in Propane Characterization Experiment.

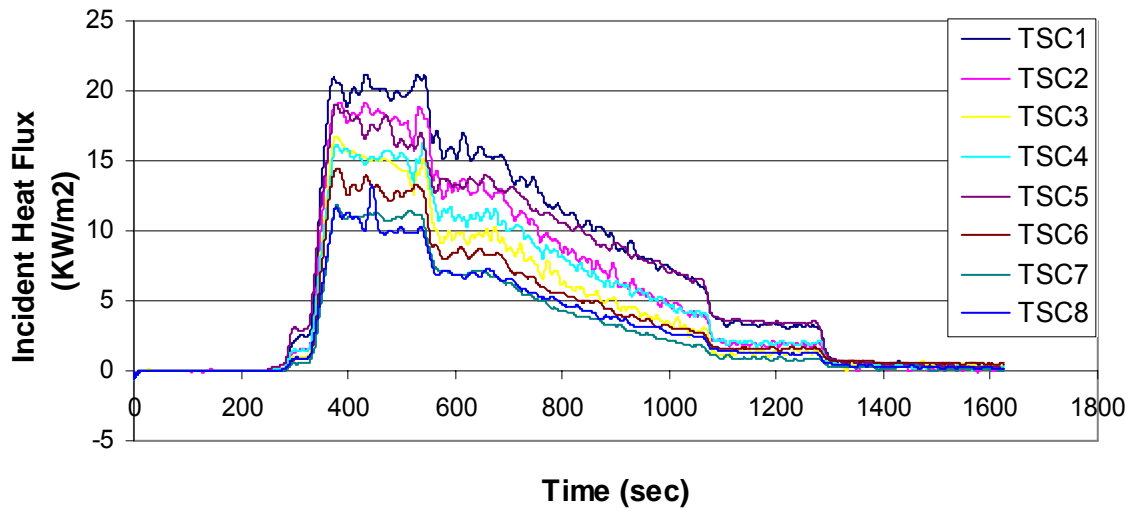


Figure D 11 Incident Heat Flux in Propane Characterization Experiment.

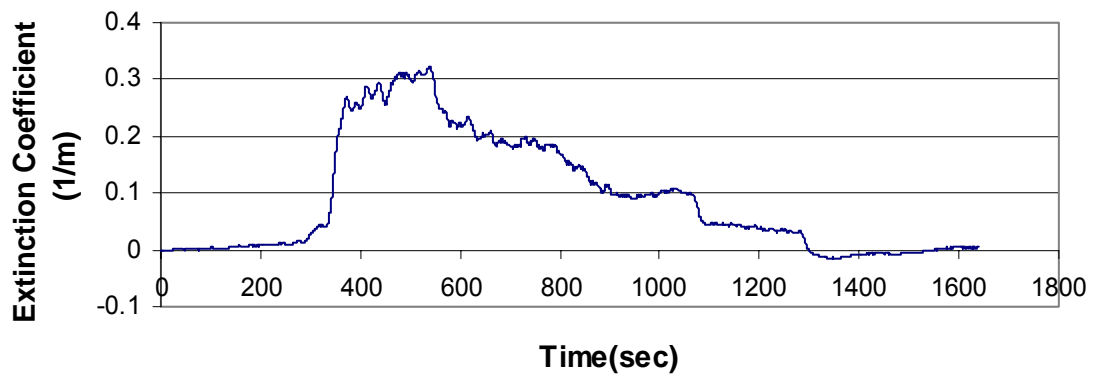


Figure D 12 Extinction Coefficient in Propane Characterization Experiment.

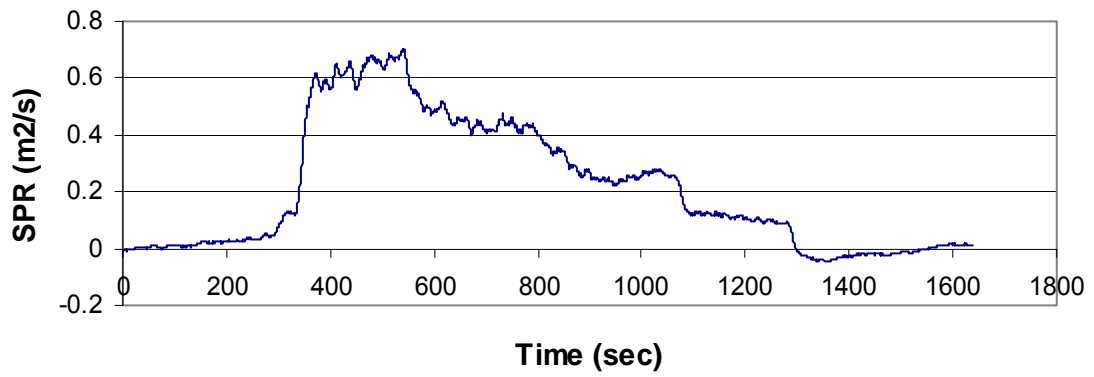


Figure D 13 Smoke Production Rate in Propane Characterization Experiment.



Figure D 14 A Photo of 1 MW Fire in Propane Characterization Experiment.

D5 Summary

Heat release rates, compartment temperature profiles, incident heat fluxes, and smoke production were reported. The heat release rates (HRR) calculated by three methods were presented. The HRR obtained from oxygen consumption method was 10~20% higher than that from carbon dioxide production method for all experiments. It is presumed that the amount of generated soot played in a role as soot is removed from the gas sample before gas analysis. The radiation correction method used provided the reasonable values under “steady state” or “slowly changing” heating. The magnitude of the thermocouple radiation correction was usually within 50°C for the upper layer and more than 100°C for the lower layer. These correction sizes show that the temperature in the lower layer was affected more by radiation than that in the upper layer. It is presumed that the sooty environments or optically thick conditions reduced the radiation effects.

D6 Appensix D References

- [1] "ISO 9705 Full Scale Room Test for Surface Products". Geneva: International Organization for Standardization, 1993.
- [2] "Class CD for FPE 587s", Worcester Polytechnic Institute, Worcester, MA, 2003.
- [3] "Omega Engineering Catalogue", Omega Engineering, Hartford, Connecticut, 2004.
- [4] "Pyromark High Temperature Paint Product Specifications Guide", Tempil, South Plainfeild, NJ, 2004.
- [5] Material Property Data. Automation Creations, Inc. 5 March 2005.
<<http://www.matweb.com/index.asp?ckck=1>>.
- [6] J.J. Alston, "Room/Corner Fire Calibration Data: Marine Composite Screening Specimens," M.S. Thesis, Worcester Polytechnic Institute, MA, U.S.A, 2004.
- [7] C. Huggett, "Estimation of the Rate of Heat Release by Means of Oxygen Consumption" Fire and Materials, Vol. 12, 1980, pp. 61-65.
- [8] W.J. Parker, "Calculations of the Heat Release Rate by Oxygen Consumption for Various Applications," NBSIR 81-2427, National Bureau of Standards, Maryland, 1982.
- [9] A. Tewarson, "Chapter 3-4 Generation of Heat and Chemical Compounds in Fires," in The SFPE Handbook of Fire Protection Engineering, 3rd ed., National Fire Protection Association, Quincy, MA, 2002.
- [10] "ASTM E-2058 Standard Test Mehods for Measurement of Synthetic Polymer Material Flammability Using a Fire Propagation Apparatus (FPA)," The American Society for Testing and Materials, Philadelphia, PA, 2003.
- [11] P.A. Enright and C.M. Fleischmann, "Cone Calorimeter – An Alternative Calibration Constant Calculation," Fire and Materials, Vol. 24, No.4, pp. 187-193, 2000.
- [12] D.D. Drysdale, "Chapter 1-5 Thermochemistry" in The SFPE Handbook of Fire Protection Engineering, 3rd ed., National Fire Protection Association, Quincy, MA, 2002.

- [13] C.N. Young, "Thermocouple Compensation", M.S. Thesis, University of Waterloo, Ontario, Canada, 1998.
- [14] D. Collis and M. Williams, "Two Dimensional Convection from Heated Wires at Low Reynolds Numbers," Journal of Fluid Mechanics, Vol. 6, pp.357-384, 1959.
- [15] "ASTM E-459 Standard Test Methods for Measuring Heat Transfer Rate Using a Thin-Skin Calorimeter", The American Society for Testing and Materials. Philadelphia, PA, 1997.
- [16] J. de Ris and M. Khan, "A Sample Holder for Determining Material Properties," Fire and Materials, Vol. 24, No.5, 219-226, 2000.

Appendix E PMMA Panel Simulation with High Activation Energy and High Pre-exponential Factor

E1 New Material Properties for PMMA

An effort to replicate a “switch” is made by setting a high activation energy E_A and a high pre-exponential factor A in the pyrolysis reaction in FDS V.4. The high E_A and A are determined by satisfying, 1) MLR remains very low until surface temperature approaches ignition temperature (361 °C) and 2) MLRs between the low E_A and A (used in PMMA panel simulation) and the high E_A and A are matched at ignition temperature (Figure E 1). Figure E 1 represents mass loss rate vs. surface temperature between the low E_A , A and the high E_A , A for black PMMA in FDS V.4 Pyrolysis Model.

Figure E 2 represents the inverse square root of the time to ignition vs. applied heat flux for thermally thick behaving PMMA. A mass flux of 4 g/m²·s is used to determine the time to ignition for Lee’s model [1]. The ignition data from Lee’s experiment and model is plotted with the values from Beaulieu [2], Tewarson and Ogden [3], and Hopkins and Quintiere [4]. As can be see in Figure E 2, new material properties combined with the FDS pyrolysis model reproduce the bench-scale experimental data for PMMA that exists in the literature. The FDS simulation is conducted with a new set of material properties. The others remains the same as the PMMA panel simulation.

E2 Results and Discussions

Figure E 3 shows heat release rate comparison between FMRC experiment [5] and the FDS simulations with a low E_A , A and a high E_A , A . It is unsuccessful to reproduce the experimental data. It takes too long for flame to spread. Note that it is worthy to try other values for E_A and A . This remains for a future work.

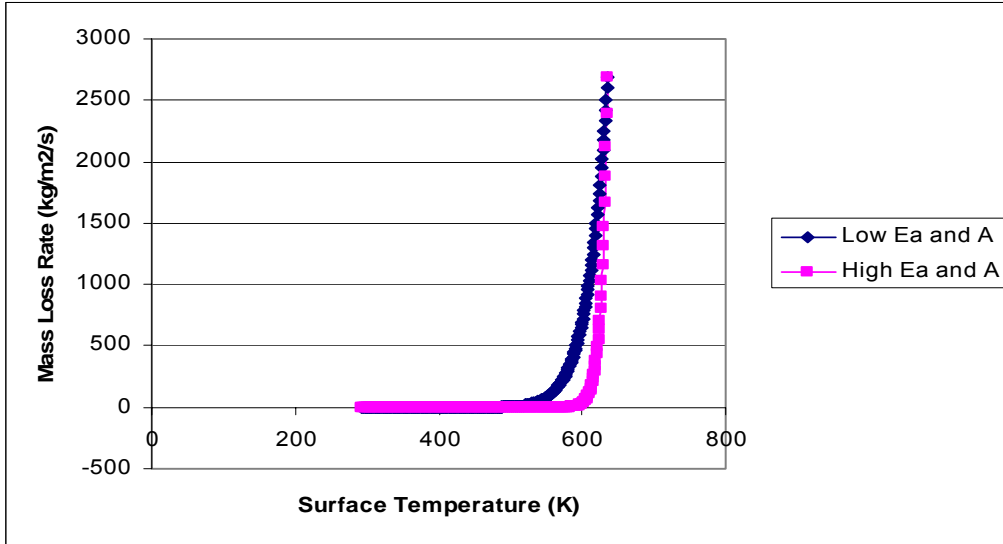


Figure E 1 Mass Loss Rate vs. Surface Temperature between Low E_A, A and high E_A, A for Black PMMA in FDS V.4 Pyrolysis Model.

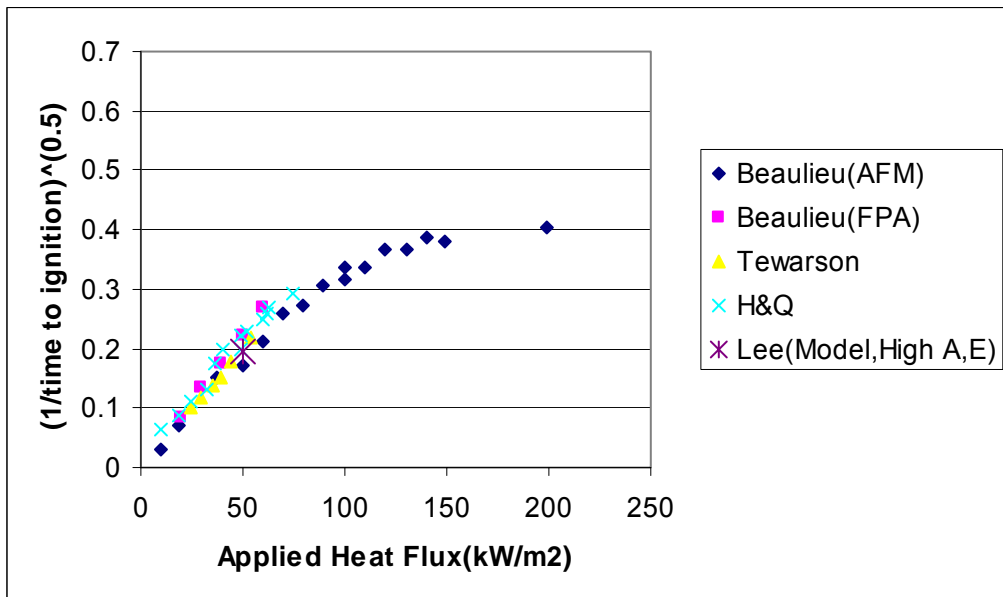


Figure E 2 Time to Ignition vs. Applied Heat Flux for Black PMMA, Thickness 0.025 m.

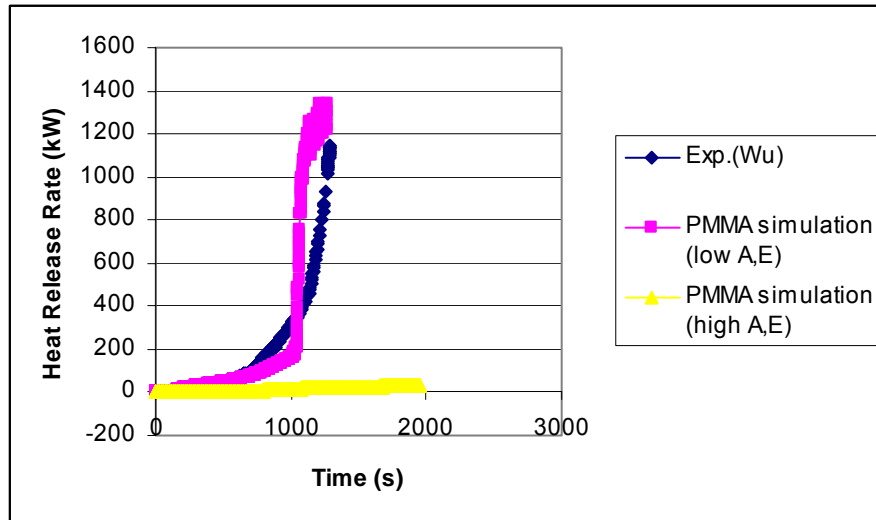


Figure E 3 Heat Release Rate Comparison between FMRC Experiment [5] and FDS Simulations.

E3 Appendix E References

- [1] S. Lee “Material Property Method using a Thermoplastic Pyrolysis Model,” MS Thesis, Worcester Polytechnic Institute, 2005.
- [2] P. Beaulieu, “Flammability Characteristics at Applied Heat Flux Levels up to 200 kW/m² and the Effect of Oxygen on Flame Heat Flux,” Ph.D Dissertation, Worcester Polytechnic Institute, 2005.
- [3] A. Tewarson and S.D. Ogden, “Fire Behavior of Polymethylmethacrylate,” *Combustion and Flame*, Vol. 89, No. 3 and 4, pp. 237-259, 1992.
- [4] D. Hopkins and J. Quintiere, “Material Fire Properties and Predictions for Thermoplastics,” *Fire Safety Journal*, Vol. 26, No. 3, pp. 241-268, 1996.
- [5] P.K, Wu, L. Orloff, and A. Tewarson, “Assessment of Material Flammability with the FSG Propagation Model and Laboratory Test Methods,” in 13th Joint Panel Meeting of the UJNR Panel on Fire Research and Safety, NIST, Gaithersburg, MD, USA, 1996.

Appendix F FDS Input File for PMMA Panel Simulation

```
HEAD CHID='PMMA' TITLE='HOT_BRICK_15kW/m2_Wu_FMRC'  
GRID IBAR=48, JBAR=24, KBAR=320  
PDIM XBAR0=0.0 XBAR=1.2 YBAR0=0 YBAR=0.60 ZBAR0=0 ZBAR=8  
TIME TWFN=1500  
MISC NFRAMES=30000 DTCORE=25 REACTION='MMA'  
VENT CB='ZBAR', SURF_ID='OPEN'  
VENT CB='YBAR', SURF_ID='OPEN'  
VENT XB=0.00,0.30,0.0,0.0,0.00,8.00, SURF_ID='MARINITE'  
VENT XB=0.90,1.20,0.0,0.0,0.00,8.00, SURF_ID='MARINITE'  
VENT CB='XBAR0', SURF_ID='SHEET METAL'  
VENT CB='XBAR', SURF_ID='SHEET METAL'  
VENT XB=0.30,0.90,0.0,0.0,0.0,5.0, SURF_ID='PMMA'  
VENT XB=0.00,1.20,0.0,0.0,0.0,5.0, SURF_ID='SHEET METAL'  
OBST XB=0.30,0.90,0.20,0.250,0.0,0.10,  
SURF_ID6='INERT','INERT','HOT_BRICK','INERT','INERT','INERT'  
THCP XYZ=0.60, 0.0, 0.025 QUANTITY='GAUGE_HEAT_FLUX' IOR=2 LABEL='GHF1_Ch' DTSAM=1.00  
THCP XYZ=0.60, 0.0, 0.050 QUANTITY='GAUGE_HEAT_FLUX' IOR=2 LABEL='GHF2_Ch' DTSAM=1.00  
THCP XYZ=0.60, 0.0, 0.075 QUANTITY='GAUGE_HEAT_FLUX' IOR=2 LABEL='GHF3_Ch' DTSAM=1.00  
THCP XYZ=0.60, 0.0, 0.10 QUANTITY='BURNING_RATE' IOR=2 LABEL='B1' DTSAM=1.00  
THCP XYZ=0.60, 0.0, 0.20 QUANTITY='BURNING_RATE' IOR=2 LABEL='B2' DTSAM=1.00  
THCP XYZ=0.60, 0.0, 0.30 QUANTITY='BURNING_RATE' IOR=2 LABEL='B3' DTSAM=1.00  
THCP XYZ=0.60, 0.0, 0.40 QUANTITY='BURNING_RATE' IOR=2 LABEL='B4' DTSAM=1.00  
THCP XYZ=0.60, 0.0, 0.50 QUANTITY='BURNING_RATE' IOR=2 LABEL='B5' DTSAM=1.00  
THCP XYZ=0.60, 0.0, 0.60 QUANTITY='BURNING_RATE' IOR=2 LABEL='B6' DTSAM=1.00  
THCP XYZ=0.60, 0.0, 0.70 QUANTITY='BURNING_RATE' IOR=2 LABEL='B7' DTSAM=1.00  
THCP XYZ=0.60, 0.0, 0.80 QUANTITY='BURNING_RATE' IOR=2 LABEL='B8' DTSAM=1.00  
THCP XYZ=0.60, 0.0, 0.90 QUANTITY='BURNING_RATE' IOR=2 LABEL='B9' DTSAM=1.00  
THCP XYZ=0.60, 0.0, 1.00 QUANTITY='BURNING_RATE' IOR=2 LABEL='B10' DTSAM=1.00  
THCP XYZ=0.60, 0.0, 1.10 QUANTITY='BURNING_RATE' IOR=2 LABEL='B11' DTSAM=1.00  
THCP XYZ=0.60, 0.0, 1.20 QUANTITY='BURNING_RATE' IOR=2 LABEL='B12' DTSAM=1.00  
THCP XYZ=0.60, 0.0, 1.30 QUANTITY='BURNING_RATE' IOR=2 LABEL='B13' DTSAM=1.00  
THCP XYZ=0.60, 0.0, 1.40 QUANTITY='BURNING_RATE' IOR=2 LABEL='B14' DTSAM=1.00  
THCP XYZ=0.60, 0.0, 1.50 QUANTITY='BURNING_RATE' IOR=2 LABEL='B15' DTSAM=1.00  
THCP XYZ=0.60, 0.0, 1.60 QUANTITY='BURNING_RATE' IOR=2 LABEL='B16' DTSAM=1.00  
THCP XYZ=0.60, 0.0, 1.70 QUANTITY='BURNING_RATE' IOR=2 LABEL='B17' DTSAM=1.00  
THCP XYZ=0.60, 0.0, 1.80 QUANTITY='BURNING_RATE' IOR=2 LABEL='B18' DTSAM=1.00  
THCP XYZ=0.60, 0.0, 1.90 QUANTITY='BURNING_RATE' IOR=2 LABEL='B19' DTSAM=1.00  
THCP XYZ=0.60, 0.0, 2.00 QUANTITY='BURNING_RATE' IOR=2 LABEL='B20' DTSAM=1.00  
THCP XYZ=0.60, 0.0, 2.10 QUANTITY='BURNING_RATE' IOR=2 LABEL='B21' DTSAM=1.00  
THCP XYZ=0.60, 0.0, 2.20 QUANTITY='BURNING_RATE' IOR=2 LABEL='B22' DTSAM=1.00  
THCP XYZ=0.60, 0.0, 2.30 QUANTITY='BURNING_RATE' IOR=2 LABEL='B23' DTSAM=1.00  
THCP XYZ=0.60, 0.0, 2.40 QUANTITY='BURNING_RATE' IOR=2 LABEL='B24' DTSAM=1.00  
THCP XYZ=0.60, 0.0, 2.50 QUANTITY='BURNING_RATE' IOR=2 LABEL='B25' DTSAM=1.00  
THCP XYZ=0.60, 0.0, 2.60 QUANTITY='BURNING_RATE' IOR=2 LABEL='B26' DTSAM=1.00  
THCP XYZ=0.60, 0.0, 2.70 QUANTITY='BURNING_RATE' IOR=2 LABEL='B27' DTSAM=1.00  
THCP XYZ=0.60, 0.0, 2.80 QUANTITY='BURNING_RATE' IOR=2 LABEL='B28' DTSAM=1.00  
THCP XYZ=0.60, 0.0, 2.90 QUANTITY='BURNING_RATE' IOR=2 LABEL='B29' DTSAM=1.00  
THCP XYZ=0.60, 0.0, 3.00 QUANTITY='BURNING_RATE' IOR=2 LABEL='B30' DTSAM=1.00  
THCP XYZ=0.60, 0.0, 3.10 QUANTITY='BURNING_RATE' IOR=2 LABEL='B31' DTSAM=1.00  
THCP XYZ=0.60, 0.0, 3.20 QUANTITY='BURNING_RATE' IOR=2 LABEL='B32' DTSAM=1.00  
THCP XYZ=0.60, 0.0, 3.30 QUANTITY='BURNING_RATE' IOR=2 LABEL='B33' DTSAM=1.00  
THCP XYZ=0.60, 0.0, 3.40 QUANTITY='BURNING_RATE' IOR=2 LABEL='B34' DTSAM=1.00  
THCP XYZ=0.60, 0.0, 3.50 QUANTITY='BURNING_RATE' IOR=2 LABEL='B35' DTSAM=1.00  
THCP XYZ=0.60, 0.0, 3.60 QUANTITY='BURNING_RATE' IOR=2 LABEL='B36' DTSAM=1.00  
THCP XYZ=0.60, 0.0, 3.70 QUANTITY='BURNING_RATE' IOR=2 LABEL='B37' DTSAM=1.00  
THCP XYZ=0.60, 0.0, 3.80 QUANTITY='BURNING_RATE' IOR=2 LABEL='B38' DTSAM=1.00  
THCP XYZ=0.60, 0.0, 3.90 QUANTITY='BURNING_RATE' IOR=2 LABEL='B39' DTSAM=1.00  
THCP XYZ=0.60, 0.0, 4.00 QUANTITY='BURNING_RATE' IOR=2 LABEL='B40' DTSAM=1.00  
THCP XYZ=0.60, 0.0, 4.10 QUANTITY='BURNING_RATE' IOR=2 LABEL='B41' DTSAM=1.00  
THCP XYZ=0.60, 0.0, 4.20 QUANTITY='BURNING_RATE' IOR=2 LABEL='B42' DTSAM=1.00  
THCP XYZ=0.60, 0.0, 4.30 QUANTITY='BURNING_RATE' IOR=2 LABEL='B43' DTSAM=1.00  
THCP XYZ=0.60, 0.0, 4.40 QUANTITY='BURNING_RATE' IOR=2 LABEL='B44' DTSAM=1.00  
THCP XYZ=0.60, 0.0, 4.50 QUANTITY='BURNING_RATE' IOR=2 LABEL='B45' DTSAM=1.00  
THCP XYZ=0.60, 0.0, 4.60 QUANTITY='BURNING_RATE' IOR=2 LABEL='B46' DTSAM=1.00  
THCP XYZ=0.60, 0.0, 4.70 QUANTITY='BURNING_RATE' IOR=2 LABEL='B47' DTSAM=1.00  
THCP XYZ=0.60, 0.0, 4.80 QUANTITY='BURNING_RATE' IOR=2 LABEL='B48' DTSAM=1.00  
THCP XYZ=0.60, 0.0, 4.90 QUANTITY='BURNING_RATE' IOR=2 LABEL='B49' DTSAM=1.00  
THCP XYZ=0.60, 0.0, 5.00 QUANTITY='BURNING_RATE' IOR=2 LABEL='B50' DTSAM=1.00  
THCP XYZ=0.60, 0.0, 0.10 QUANTITY='GAUGE_HEAT_FLUX' IOR=2 LABEL='HF1' DTSAM=1.00  
THCP XYZ=0.60, 0.0, 0.20 QUANTITY='GAUGE_HEAT_FLUX' IOR=2 LABEL='HF2' DTSAM=1.00  
THCP XYZ=0.60, 0.0, 0.30 QUANTITY='GAUGE_HEAT_FLUX' IOR=2 LABEL='HF3' DTSAM=1.00  
THCP XYZ=0.60, 0.0, 0.40 QUANTITY='GAUGE_HEAT_FLUX' IOR=2 LABEL='HF4' DTSAM=1.00  
THCP XYZ=0.60, 0.0, 0.50 QUANTITY='GAUGE_HEAT_FLUX' IOR=2 LABEL='HF5' DTSAM=1.00  
THCP XYZ=0.60, 0.0, 0.60 QUANTITY='GAUGE_HEAT_FLUX' IOR=2 LABEL='HF6' DTSAM=1.00  
THCP XYZ=0.60, 0.0, 0.70 QUANTITY='GAUGE_HEAT_FLUX' IOR=2 LABEL='HF7' DTSAM=1.00
```


THCP XYZ=0.60, 0.025, 3.80 QUANTITY='TEMPERATURE' LABEL='T38' DTSAM=1.00
 THCP XYZ=0.60, 0.025, 3.90 QUANTITY='TEMPERATURE' LABEL='T39' DTSAM=1.00
 THCP XYZ=0.60, 0.025, 4.00 QUANTITY='TEMPERATURE' LABEL='T40' DTSAM=1.00
 THCP XYZ=0.60, 0.025, 4.10 QUANTITY='TEMPERATURE' LABEL='T41' DTSAM=1.00
 THCP XYZ=0.60, 0.025, 4.20 QUANTITY='TEMPERATURE' LABEL='T42' DTSAM=1.00
 THCP XYZ=0.60, 0.025, 4.30 QUANTITY='TEMPERATURE' LABEL='T43' DTSAM=1.00
 THCP XYZ=0.60, 0.025, 4.40 QUANTITY='TEMPERATURE' LABEL='T44' DTSAM=1.00
 THCP XYZ=0.60, 0.025, 4.50 QUANTITY='TEMPERATURE' LABEL='T45' DTSAM=1.00
 THCP XYZ=0.60, 0.025, 4.60 QUANTITY='TEMPERATURE' LABEL='T46' DTSAM=1.00
 THCP XYZ=0.60, 0.025, 4.70 QUANTITY='TEMPERATURE' LABEL='T47' DTSAM=1.00
 THCP XYZ=0.60, 0.025, 4.80 QUANTITY='TEMPERATURE' LABEL='T48' DTSAM=1.00
 THCP XYZ=0.60, 0.025, 4.90 QUANTITY='TEMPERATURE' LABEL='T49' DTSAM=1.00
 THCP XYZ=0.60, 0.025, 5.00 QUANTITY='TEMPERATURE' LABEL='T50' DTSAM=1.00
 THCP XB=0.0,1.2,0.0,0.6,0.0,8.0, QUANTITY='HRR', LABEL='HRR', DTSAM=1.
 BDNF QUANTITY='HEAT_FLUX' DTSAM=1.00
 BDNF QUANTITY='WALL_TEMPERATURE' DTSAM=1.00
 BDNF QUANTITY='BURNING_RATE' DTSAM=1.00
 BDNF QUANTITY='CONVECTIVE_FLUX' DTSAM=1.00
 BDNF QUANTITY='RADIATIVE_FLUX' DTSAM=1.00
 SLCF PBX=0.60 QUANTITY='TEMPERATURE'
 SLCF PBX=0.60 QUANTITY='DENSITY'
 SLCF PBX=0.60 QUANTITY='VELOCITY'
 SLCF PBZ=8.00 QUANTITY='TEMPERATURE'
 SLCF PBZ=8.00 QUANTITY='DENSITY'
 SLCF PBZ=8.00 QUANTITY='VELOCITY'
 SLCF XB=0.0,1.2,0.0,0.6,0.0,8.0, QUANTITY='HRRPUV'
 SURF ID='HOT_BRICK', TMPWAL=760., RGB=0,1,0
 REAC ID='MMA'
 FYI='MMA monomer, C_5 H_8 O_2'
 EPUMO2=13125.
 MW_FUEL=100.
 NU_O2=6.
 NU_H2O=4.
 NU_CO2=5.
 SOOT_YIELD=0.022
 SURF ID = 'PMMA'
 FYI = 'Lee model data'
 RGB = 0.30,0.90,0.90
 A = 3015730
 E = 119000
 HEAT_OF_VAPORIZATION = 2000
 HEAT_OF_COMBUSTION = 23900
 DELTA = 0.025
 KS = 0.17
 C_P = 1.9
 DENSITY = 1180
 BACKING = 'INSULATED'
 SURF ID = 'MARINITE'
 FYI = 'BNZ Materials, Marinite I'
 RGB = 0.70,0.70,0.70
 BACKING = 'EXPOSED'
 EMISSIVITY = 0.8
 DENSITY = 737.
 RAMP_C_P = 'rampcp'
 RAMP_KS = 'rampks'
 DELTA = 0.0254
 RAMP ID='rampks',T= 24.,F=0.13
 RAMP ID='rampks',T=149.,F=0.12
 RAMP ID='rampks',T=538.,F=0.12
 RAMP ID='rampcp',T= 93.,F=1.172
 RAMP ID='rampcp',T=205.,F=1.255
 RAMP ID='rampcp',T=316.,F=1.339
 RAMP ID='rampcp',T=425.,F=1.423
 SURF ID = 'SHEET METAL'
 FYI = '24 guage sheet metal'
 RGB = 0.20,0.20,0.20
 C_DELTA_RHO = 4.7
 DELTA = 0.00051
 TMPWAL = 20.0